ACCURATE IRIS RECOGNITION AT-A-DISTANCE AND UNDER LESS CONSTRAINED ENVIRONMENTS

TAN CHUN WEI

Ph.D

The Hong Kong Polytechnic University

2014

THE HONG KONG POLYTECHNIC UNIVERSITY

DEPARTMENT OF COMPUTING

Accurate Iris Recognition At-a-distance and Under Less Constrained Environments

By

TAN CHUN WEI

A thesis submitted in partial fulfilment

of the requirements for the degree of

Doctor of Philosophy

March 2014

CERTIFICATE OF ORIGINALITY

I hereby declare that this thesis is my own work and that, to the best of my knowledge and belief, it reproduces no material previously published or written, nor material that has been accepted for the award of any other degree or diploma, except where due acknowledgement has been made in the text.

____________________ (Signed)

TAN CHUN WEI (Name of student)

ABSTRACT

Accurate iris recognition using eye or face images acquired *at-a-distance* and *under less constrained environments* requires development of specialized iris segmentation and recognition strategies. Image quality of such distantly acquired eye or face images under less constrained imaging conditions are usually degraded due to the multiple commonly observed noise sources such as occlusions (eyeglasses, hair, eyelashes, eyelid and shadow), reflections, motion or defocus blur, off-angle and partial eye images. The influence from the noise is even more noticeable from the eye images acquired using visible illumination imaging. Performing iris segmentation and recognition on such noisy eye images can be highly challenging. Therefore, it is the main objective of this thesis to provide feasible solutions to improve the effectiveness of the iris recognition strategy at-a-distance and under less constrained environments.

We develop an iris segmentation approach by exploiting the random walker algorithm in order to efficiently estimate coarsely segmented iris region. Such coarsely segmented iris region reduces the search space for further refinement through a set of developed post processing operations which can effectively improve the segmentation accuracy. Most of the commonly observed noise sources can be identified and masked by the developed post processing operations. The segmentation accuracy is evaluated on subsets of distantly acquired images from three publicly available databases: UBIRIS.v2, FRGC and CASIA.v4-distance, by comparing the binary segmented iris mask with the corresponding ground truth mask.

The second contribution of this thesis is the development of a global iris bits stabilization encoding and a localized Zernike moments phase-based encoding strategies. The global iris encoding strategy has its strength in less noisy region pixels while the localized iris encoding strategy can be more tolerant to imaging quality variations (*e.g.* scale change, illumination change, rotation, and translation) and noise. The complementary matching information from the joint strategy of both global and localized iris encoding can provide more accurate recognition accuracy

for the iris recognition at-a-distance and under less constrained environments. The reported recognition performance from using such joint matching strategy on UBIRIS.v2, FRGC and CASIA.v4-distance databases is encouraging, but further research efforts are still required to improve the recognition accuracy. Therefore, we present a study on the recent emerging research in the periocular recognition. The joint matching information from simultaneously acquired iris and periocular features has shown to achieve even better recognition accuracy than any of the iris or periocular features alone.

A final contribution of this thesis is the development of a computationally attractive binary encoding strategy by exploiting the geometric information for localized iris encoding, which we refer it as geometric key iris encoding. Such geometric key iris encoding strategy is aimed to provide an alternative to the global iris bits stabilization encoding which incurs relatively higher computational complexity. Our experimental results suggest that the joint matching information from the geometric key encoding and Zernike moments phase-based encoding strategies achieve better or comparable recognition performance but with reduced computational complexity.

PUBLICATIONS

Journal papers:

1. **Chun-Wei Tan**, Ajay Kumar, "Efficient and accurate at-a-distance iris recognition using geometric key iris encoding," *IEEE Trans. Inf. Forensics Secur.*, vol. 9, no. 9, pp. 1518-1526, 2014.
2. **Chun-Wei Tan**, Ajay Kumar, "Accurate iris recognition at a distance using stabilized iris encoding and Zernike Moments phase features," *IEEE Trans. Image Process.*, vol. 23, no. 9, pp. 3962-3974, 2014.
3. **Chun-Wei Tan**, Ajay Kumar, "Towards online iris and periocular recognition under relaxed imaging constraints," *IEEE Trans. Image Process.*, vol. 22, no. 10, pp. 3751-3765, 2013.
4. **Chun-Wei Tan**, Ajay Kumar, "A unified framework for automated iris segmentation using distantly acquired face images," *IEEE Trans. Image Process.*, vol. 21, no. 9, pp. 4068-4079, 2012.

Conference papers:

1. **Chun-Wei Tan**, Ajay Kumar, "Adaptive and localized iris weight map for accurate iris recognition under less constrained environments," *Proc. BTAS 2013*, pp. 1-7, 2013.
2. **Chun-Wei Tan**, Ajay Kumar, "Efficient iris segmentation using grow-cut algorithm for distantly acquired iris images," *Proc. BTAS 2012*, 2012.
3. **Chun-Wei Tan**, Ajay Kumar, "Robust automatic human Identification at-a-distance exploiting iris and periocular features", *Proc. ICPR 2012*, 2012.
4. Ajay Kumar, Tak-Shing. Chan, **Chun-Wei Tan**, "Human identification from at-a-distance face images using sparse representation of local iris features," *Proc ICB 2012*, pp.303-309, 2012.
5. **Chun-Wei Tan**, Ajay Kumar, "Automated segmentation of iris images using visible wavelength face images," *Proc. CVPRW 2011*, pp. 9-14, 2011.

ACKNOWLEDGEMENTS

It would not have been possible to write this doctoral thesis without the help and support of the kind people around me, to only some of whom it is possible to give particular mention here.

First of all, I would like to express my deepest gratitude to my supervisor Dr. Ajay Kumar for this advice, patience, enthusiasm, motivation and support throughout the years. I would also like to thank my co-supervisor Prof. You Jia for her enormous support to my research work. I offer my sincere appreciation for the financial, academic and technical support of The Hong Kong Polytechnic University and its staff, particularly in the award of a postgraduate research studentship that provided the necessary financial support for this research. I would also like to thank my external examiners, Prof. Kevin W. Bowyer (University of Notre Dame) and Prof. Oscar Au (Hong Kong University of Science and Technology) for their invaluable advises to further improve my thesis.

I owe a great debt of gratitude to my former colleagues at the Faculty of Information and Communication Technology in UTAR for their enormous support and assistance, especially the dean, Prof. Liew Soung Yue, deputy dean, Dr. Michael Cheng, and head of department, Dr. Alex Ooi. I would like to thank my former supervisors, Prof. Prof. Lee Byung Gook (Dongseo University) and Assoc. Prof. Andrew Teoh Beng Jin (Yonsei University), who have been my mentors since the very beginning of my postgraduate studies. I am particularly grateful to Dr. Lim Meng Hui (Hong Kong Baptist University), who has been a good friend of mine since 2007 for all his encouragement and advice in writing this thesis.

I would also like to gratefully acknowledge the SOCIA Lab in University of Beira Interior (Portugal), NIST (USA) and Institute of Automation in Chinese Academy of Sciences (China) for their contributions of the databases employed in this research.

My gratitude and heartfelt thanks is extended to all my friends who have directly or indirectly supported me academically, personally and emotionally along the journey in this endeavor.

Last, but not least, I would like express appreciation to my family for their love, understanding, encouragement and support over the years. Without them, this thesis would never have been possible.

TABLE OF CONTENTS

CERTIFICATE OF ORIGINALITY i

ABSTRACT ii

PUBLICATIONS iv

ACKNOWLEDGEMENTS v

TABLE OF CONTENTS vii

LIST OF FIGURES x

LIST OF TABLES xiv

ABBREVIATIONS xv

CHAPTER 1 Introduction 1

1.1 Biometrics Technology 1
1.1.1 Modes of Operation 3
1.1.2 Performance Evaluation 5
1.2 The Human Eye and Iris 7
1.3 Iris Recognition 9
1.4 Organization of Thesis 15

CHAPTER 2 Iris Recognition under Constrained Environment 17

2.1 Iris Segmentation 18
2.1.1 Daugman's Method 18
2.1.2 Kazuyuki et al. Method 20
2.1.3 He et al. Method 21
2.1.4 Kumar and Passi's Method 22
2.1.5 Other Methods 23
2.2 Feature Encoding and Matching 24
2.2.1 Gabor Filters 24
2.2.2 Log-Gabor Filters 25
2.2.3 Ordinal Filters 26
2.2.4 Fragile Bits 28
2.2.5 Personalized Weight Map 29
2.2.6 Other Methods 29
2.3 Summary 30

CHAPTER 3 Iris Recognition under Less Constrained Environments 31

3.1 Relaxed Imaging Setup 31

3.1.1 Limitations and Challenges *33*
3.2 Iris Segmentation 36
3.2.1 Tan et al. Method *36*
3.2.2 Proença's Method *37*
3.2.3 Tan and Kumar's Method *39*
3.2.4 Other Methods *40*
3.3 Feature Encoding and Matching 41
3.3.1 Tan et al. Method *42*
3.3.2 Wang et al. Method *42*
3.3.3 Santos and Hoyle's Method *42*
3.3.4 Other Methods *43*
3.4 Summary 43

CHAPTER 4 Proposed Segmentation Approach for Iris Images Acquired under Less Constrained Environments 45

4.1 Methodology 45
4.1.1 Preprocessing *46*
4.1.2 Coarse Iris Segmentation *47*
4.1.3 Initial Iris Center Estimation *49*
4.1.4 Iris and Pupil Localization *52*
4.1.5 Boundary Refinement *54*
4.1.6 Eyelid Localization with Adaptive Eyelid Models *56*
4.1.7 Eyelashes and Shadow Masking *59*
4.2 Experiments and Results 60
4.2.1 Databases and Evaluation Protocol *60*
4.2.2 Performance Comparison *61*
4.3 Summary 66

CHAPTER 5 Proposed Feature Encoding and Matching Approaches for Iris Images Acquired under Less Constrained Environments 67

5.1 Methodology 68
5.1.1 Global Iris Feature Representation *69*
5.1.2 Zernike Moments Phase-based Encoding *74*
5.2 Experiments and Results 77
5.2.1 Databases and Evaluation Protocol *78*
5.2.2 Comparison Between Real-valued and Quantized ZM Phase-based Features 80
5.2.3 Combination of Global and Local Matching Scores *81*
5.2.4 Performance Comparison *86*
5.2.5 Discussion *92*
5.3 Summary 94

CHAPTER 6 Periocular Recognition 96

6.1 Methodology 96
6.1.1 Segmentation of Periocular Region 96
6.2 Experiments and Results 97
6.2.1 Comparison between Different Feature Extraction Methods 98
6.2.2 Combination of Iris and Periocular Matching Scores 103
6.3 Summary 106

CHAPTER 7 GeoKey Iris Encoding 107

7.1 Methodology 107
7.1.1 Generating Geometric Key 109
7.1.2 Geometric Key Encoding 110
7.2 Experiments and Results 113
7.2.1 Databases and Evaluation Protocol 113
7.2.2 Combination of Global and Local Matching Scores 113
7.2.3 Performance Comparison 116
7.2.4 Joint Scores from Multiple Phase-based Features 120
7.2.5 Discussion 120
7.3 Summary 122

CHAPTER 8 Conclusions and Future Work 123

8.1 Contributions 125
8.2 Future Work 126

BIBLIOGRAPHY 127

LIST OF FIGURES

Figure 1.1: Examples of biometric traits (pictures from [7], [8], [9], [10], [11], [12], [13]). 2
Figure 1.2: Typical categories of various biometric applications. 3
Figure 1.3: Block diagram of a generic biometric system. 3
Figure 1.4: Modes of operation of a biometric system. 4
Figure 1.5: The performance of a biometric system evaluated using ROC and CMC curves. 7
Figure 1.6: Anatomy of the human eye. 7
Figure 1.7: The anterior and posterior surfaces of the iris (pictures from [19]). 8
Figure 1.8: The human iris exhibits extremely rich texture patterns (picture from [33], ID: 015L_2). 10
Figure 1.9: Iris image acquisition *at-a-distance* in laboratory environment. 10
Figure 1.10: Sample segmentation result for an iris image (ID: 001_09) from IITD iris database [42]. 11
Figure 1.11: Iris normalization based on Daugman's rubber sheet model. 12
Figure 2.1: A commercial NIR-based iris recognition system deployed in UAE (picture from [68]). 17
Figure 2.2: Pupillary and limbic boundaries approximation using active contour model (picture from [43]). 19
Figure 2.3: Deformable iris model (picture from [56]). 20
Figure 2.4: The pulling and pushing method (pictures from [53]). 21
Figure 2.5: Sample segmentation result (ID: 001_01) from IITD iris database [42] 23
Figure 2.6: Quantization of the phase-only information in order to produce the binary representation, *i.e.* iris code (picture from [31]). 24
Figure 2.7: Visualization of the Log-Gabor filters in spatial domain with the parameters, $f0 = 16$ and $\sigma f = 0.55$. 25
Figure 2.8: Examples of the multilobe differential filters. All filters are constructed with the basic lobe size of 21×21 and $\sigma = 3.5$. 27
Figure 3.1: Less constrained imaging setup in a laboratory environment (picture from [40]). 32
Figure 3.2: Electromagnetic spectrum (picture from [81]). 32
Figure 3.3: Sample eye images from UBIRIS.v2 database [40]. 34
Figure 3.4: Segmentation results using gradient-based approach on eye images from UBIRIS.v2 database. 35
Figure 3.5: Examples of normalized iris images acquired under constrained and less constrained environments. 36
Figure 3.6: Integro-differential based constellation model (picture from [59]). 37

Figure 3.7: Proportion of sclera features computed from classified sclera pixels.....38
Figure 4.1: Block diagram of the proposed iris segmentation approach. 46
Figure 4.2: Flow chart of coarse segmentation using random walker based algorithm. 47
Figure 4.3: Initial center estimation. (a) Input enhanced image (color images are presented to provide better visualization), (b) Coarse segmented iris mask, (c) The estimated initial center (yellow mark) using (b), (d) Refined Ri, (e) The initial estimated iris center. 50
Figure 4.4: Initial center estimation using localized intensity information. (a) Extracted red channel plane, (b) Gamma corrected of image (a), with $\gamma = 0.8$, (c) The corresponding refined mask Bc superimposed with a rectangle indicates the bounding region, (d) The region with the minimum average intensity, (e) Binary mask Br and its center of mass. The estimated distance between C and C, dC, C = 20.8945. 51
Figure 4.5: Limbic and pupillary boundaries localization. (a) Input smoothed image Ir, (b) Edgemap of (a), (c) Localized limbic and pupillary boundaries. 54
Figure 4.6: Boundary refinement. (a) Half-ring region $R1$, (b) Region $R2$, (c) Thresholded region, (d) Refined limbic boundary mask. 56
Figure 4.7: Eyelid localization steps. 56
Figure 4.8: Adaptive eyelid models construction. Note that the edge points shown in the figures were enhanced for better visualization. (Note (c)-(e): Control points CMl are denoted using red 'o', bounding region is shown using yellow box and the constructed model is shown as green curve). 57
Figure 4.9: Sample eyelid localization results obtained using the adaptive eyelid model. 58
Figure 4.10: Eyelashes and shadow masking. 59
Figure 4.11: Segmentation performance. 62
Figure 4.12: Sample segmentation results. 65
Figure 5.1: Block diagram of the proposed joint iris recognition strategy using global and localized (ZMs phase-based encoding) iris features encoding. 68
Figure 5.2: Overlapping block strategy (Note that the actual image size of (b) and (c) are larger than the (a), and therefore they are resized to better utilization of space).70
Figure 5.3: Examples of the trained probability map (last row) computed from five iris codes (first five rows) from CASIA.v4-distance database (Image IDs: {S4011D00, S4011D01, S4011D02, S4011D03, S4011D04}, {S4023D00, S4023D01, S4023D02, S4023D03, S4023D04}). Brighter pixel indicates the bit is more stable while darker pixel indicates otherwise. 71
Figure 5.4: The influence of μ on the bit probability. 72
Figure 5.5: Phase angle information for three Zernike features respectively computed from the normalized iris images from CASIA.v4-distance database. Features (a) and (b) are computed from the images of the same class. The varying angles represent the encoded iris features using the phase information of the ZMs.

The similarity scores between (a) and (a), (a) and (b), and (a) and (c) are $sa, a = 0$, $sa, b = 16.624$ and $sa, c = 27.218$, respectively. 76
Figure 5.6: Parameters selection for Zernike-moments phase-based encoding on three employed databases with the corresponding window sizes {25, 17, 25}.........79
Figure 5.7: Normalized matching score distributions for the proposed global and local encoding approaches...81
Figure 5.8: Receiver operating characteristic curves from the proposed ZMs phase-based encoding approach...82
Figure 5.9: Cumulative match characteristic curves from the proposed ZMs phase-based encoding approach...83
Figure 5.10: Receiver operating characteristics from the proposed. 84
Figure 5.11: Cumulative match curves from the proposed approach.........................85
Figure 5.12: Receiver operating characteristics from various approaches................87
Figure 5.13: Cumulative match curves from various approaches. 88
Figure 5.14: Expected improvement in Equal Error Rate as compared to the competing approaches in literature...89
Figure 5.15: Cumulative match curves from the comparison with the best two reported iris matching methods. 91
Figure 6.1: Segmentation of periocular regions from face images acquired at-a-distance (left eyes are employed for better illustration and comparison)..................97
Figure 6.2: Cumulative match characteristic curves of different periocular feature extraction methods computed on local periocular regions. 99
Figure 6.3: Cumulative match characteristic curves of different periocular feature extraction methods computed on global periocular regions......................................99
Figure 6.4: Sample images from the three employed databases. 100
Figure 6.5: Block diagrams of the developed periocular recognition approach......101
Figure 6.6: Estimation of the parameter k for constructing texton dictionary.........102
Figure 6.7: Receiver operating characteristics from joint periocular and iris strategy. 104
Figure 6.8: Cumulative match characteristics from joint periocular and iris strategy. 105
Figure 7.1: Block diagram of the proposed geometric key iris encoding scheme for iris images acquired at-a-distance and under less constrained conditions. 108
Figure 7.2: Examples of the GeoKey at different configurations ($B = 32; d = 32$). (a) original GeoKey, (b) rotation of (a) at $\theta = 30$-degree, (c) rotation of (a) at $\theta = 60$-degree, (d) scaled of (a) at $s = 0.85$, (e) scaled of (a) at $s = 1.15$, (f) scaled and rotation of (a) at $s = 0.65$ and $\theta = 30$-degree...109
Figure 7.3: Illustration of the GeoKey iris encoding from an image patch of size $B \times B$. The binary test is performed on the local smoothing windows of size $S \times S$ centered at $\boldsymbol{x1}$ and $\boldsymbol{x2}$, respectively. Therefore, the $\boldsymbol{x1}$ and $\boldsymbol{x2}$ represent the average values of the filter responses computed from the respective local window $\mathbf{w}$. 111

Figure 7.4: Receiver operating characteristics from the proposed GeoKey encoding scheme. 114
Figure 7.5: Cumulative match characteristic curves from the proposed GeoKey encoding scheme. 115
Figure 7.6: Expected improvement in Equal Error Rate as compared to several competing approaches from the literature. 117
Figure 7.7: Receiver operating characteristic curves from various approaches. 118
Figure 7.8:. Cumulative match characteristic curves from various approaches. 119
Figure 7.9: Cumulative match characteristic curves from joint scores of multiple phase-based features. 120
Figure 8.1: Contribution highlights of this thesis. 125

LIST OF TABLES

Table 1.1: Recent promising works in the iris biometrics (between year 2007 and 2013)........13
Table 2.1: Estimation of fragile bits........28
Table 3.1: Comparison between NIR and visible illumination based iris recognition [65]........33
Table 3.2: Top three ranking from the NICE.II competition [90]........41
Table 4.1: Estimated Euclidean distance between iris and pupil centers........52
Table 4.2: Overview of the three employed databases........60
Table 4.3: Average execution time........63
Table 5.1: Numbers of images and subjects of the employed databases........78
Table 5.2: Parameters employed by the proposed approach........79
Table 5.3: The Equal Error Rate and decidability index obtained by the different approaches from the three employed databases........86
Table 5.4: Parameter employed for score combination........90
Table 5.5: Memory requirement and the computational cost of the proposed iris matching strategy........93
Table 6.1: Overview of the three employed databases........98
Table 6.2: The Equal Error Rate and decidability index from joint periocular and iris strategy........103
Table 7.1: Parameters employed by the proposed iris encoding scheme........113
Table 7.2: The Equal Error Rate and decidability index obtained by the different approaches from the three employed databases........117
Table 7.3: Memory requirements by the best three algorithms from the experiments........121

ABBREVIATIONS

ANSI	American National Standards Institute
BATH	University of Bath Iris Database
CASIA	Institute of Automation Chinese Academy of Sciences Iris Image Database
CCD	Charge Coupled Device
CIE	International Commission on Illumination
CMC	Cumulative Match Curve
CMOS	Complementary Metal Oxide Semiconductor
DCT	Discrete Cosine Transform
DNA	Deoxyribonucleic Acid
EER	Equal Error Rate
FAR	False Acceptance Rate
FERET	Face Recognition Technology Database
FRGC	Face Recognition Grand Challenge Face Image Database
FRR	False Rejection Rate
GAR	Genuine Acceptance Rate
ICAO	International Civil Aviation Organization
ICE	Iris Challenge Evaluation Iris Database
IITD	Indian Institute of Technology Delhi Iris Database
ISO	International Organization for Standardization
MBGC	Multiple Biometric Grand Challenge Database
NICE	Noisy Iris Challenge Evaluation
NIR	Near-Infrared
NIST	National Institute of Standards and Technology
ROC	Receiver Operating Characteristic
UAE	United Arab Emirates
UBIRIS	University of Beira Interior Iris Image Database
WVU	West Virginia University Iris Database

CHAPTER 1

Introduction

1.1 Biometrics Technology

Biometric recognition, or simply the biometrics, is term comes from the Greek *bios* (life) and *metron* (measure). Biometrics is the science of identifying or verifying the identity of an individual based on the physiological characteristics such as fingerprint, face, palmprint, ear, iris, DNA (Deoxyribonucleic Acid), retina, hand veins and hand geometry, or behavioral characteristics such as gait, voice, signature and keystroke of the person [1], [2], [3], [4]. Figure 1.1 shows some examples of the physiological and behavioral biometric traits which can be used for various personal recognition purposes. In other words, any biological characteristic, be it physiological or behavioral, can be used as biometric as long as it satisfies the following characteristics: uniqueness, universality, permanence, collectability, acceptability, performance and circumvention [1], [4], [5]. The *uniqueness* measures the distinctiveness of the biometric trait between any two persons. The biometric trait being measured should be sufficiently different in order to make good distinguishing of individuals. The *universality* refers to the availability of the biometric trait being measured across the population. The *permanence* measures the rate of change of the biometric trait over a period of time. A good biometric trait is expected to be invariant or has little changes over time. The *collectability* refers to the easiness in collecting the biometric trait using suitable sensors. The *acceptability* reflects the overall willingness of the target population to accept the use of biometric technology in their daily lives. The privacy reasons are the main factor which concerns the use of the biometric technology in a particular population. The *performance* concerns about the overall technology burden such as recognition accuracy, computational cost and equipment required to practically deploy a biometric system. The *circumvention* concerns about the security perspective of a biometric system by evaluating the easiness of using fraudulent approaches to deceive the system. These seven characteristics serve as guidance to objectively determine the choice of a biometric trait to be used in a biometric application. Therefore, a practical biometric solution should be evaluated according to these seven characteristics which meet the specified requirements and constraints as imposed by the biometric application. Figure 1.2 shows nine general areas as suggested in [6] where the biometric applications are actively involved.

Figure 1.1: Examples of biometric traits (pictures from [7], [8], [9], [10], [11], [12], [13]).

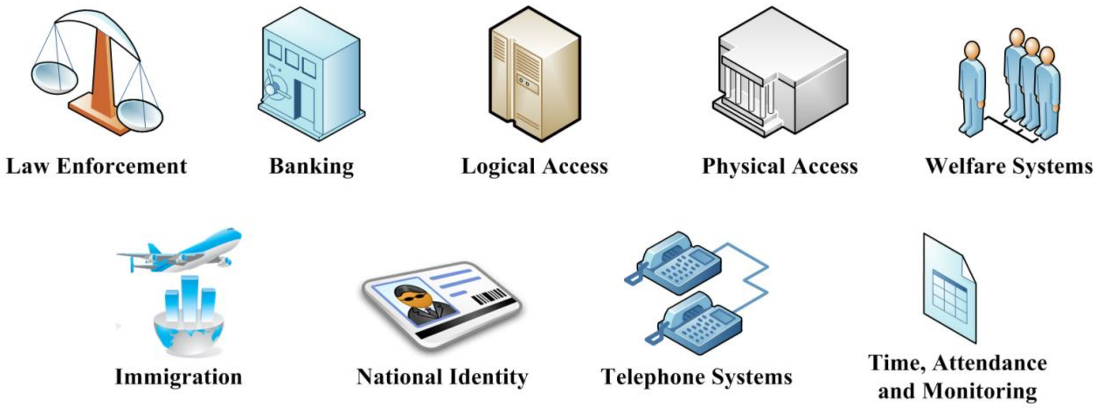

Figure 1.2: Typical categories of various biometric applications.

1.1.1 Modes of Operation

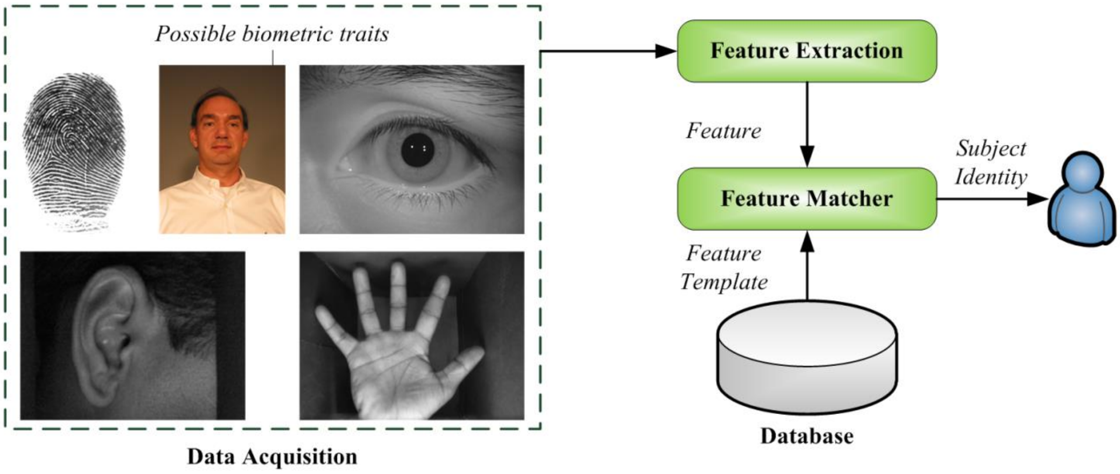

Figure 1.3: Block diagram of a generic biometric system.

Biometrics is being increasingly pervasive today to provide reliable automated personal recognition[a] in ranges of applications such as border control, performing a financial transaction, law enforcement, *etc* [14], [15]. Biometric recognition can be regarded as a pattern recognition problem by comparing the similarity between any two given biometric features. A generic biometric system consists of four primary procedures: data acquisition, feature extraction, feature matcher and database,

[a] We use the generic term *recognition* as commonly used in the biometrics literatures to refer to both identification and verification operations throughout this thesis.

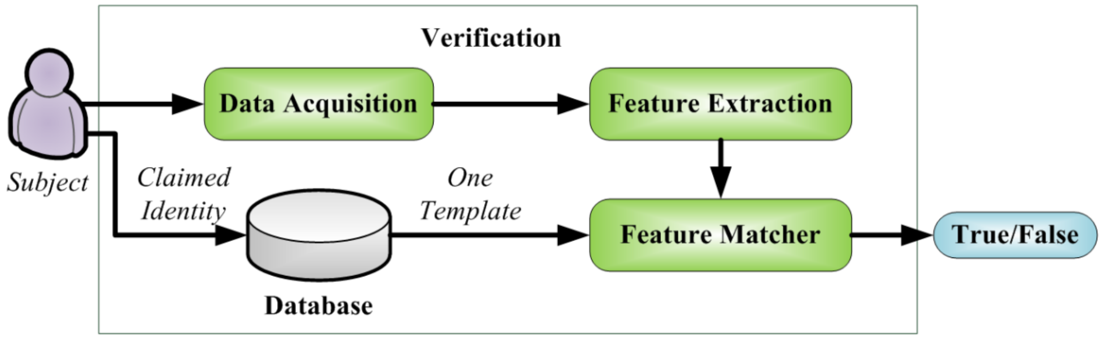

(a) Verification mode.

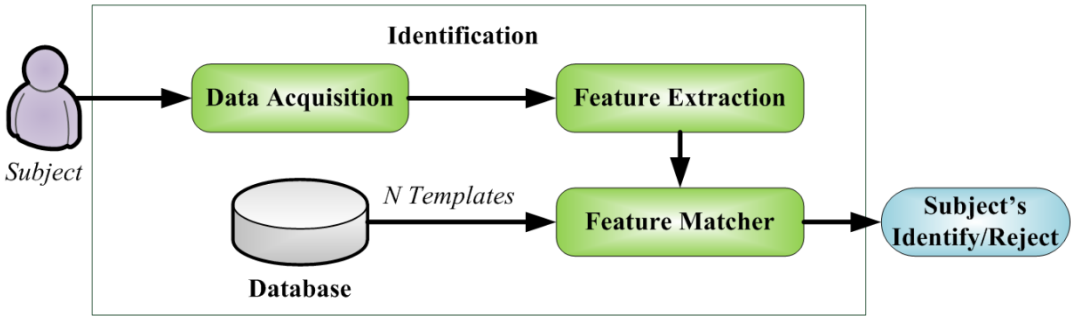

(b) Identification mode.

Figure 1.4: Modes of operation of a biometric system.

as depicted in Figure 1.3. The *data acquisition* process acquires raw biometric sample, and convert it into digital form for further processing. The *feature extraction* serves to compute/extract distinctive feature representation from the acquired biometric sample. During enrollment, *i.e.* registering a subject into the biometric system, such extracted feature representation is stored in the database and is commonly regarded as *feature template*. The responsibility of the matcher is to make comparison of the extracted feature against the registered feature templates in the database. The similarity between any two compared features is typically represented using a similarity/dissimilarity score. For example, Hamming distance is used to indicate the similarity level of two acquired iris codes, with the score closes to zero being the most similar while the score closes to one being the most dissimilar.

A biometric system can be operated either in the verification or identification mode to meet the requirements by the application. Figure 1.4 shows the functioning procedures by the verification and identification methods, respectively. In the verification mode, the system attempts to validate the identity of a subject by comparing the acquired biometric data with the template(s) retrieved from the database as indexed by the identifier supplied by the subject. Therefore, the verification mode performs a one-to-one matching to determine if the subject is indeed who she/he claims to be. For example, the ICAO-compliant biometric passport or national identity card which stores the biometric information such as face, fingerprint or/and iris is employed in many countries to verify the identities of the travelers/citizens [16], [17], [15].

In the identification mode, the biometric system attempts to recognize the identity of a subject by performing a complete search of the templates for all the subjects registered in the database (*N* comparison). Therefore, the identification mode conducts a one-to-many comparison to determine the identity of a subject, or a rejection decision is made if the subject is not registered in the database. For example, the use of face recognition technology in automated surveillance systems to identifying subjects in public or identifying unknown persons of interest from images [18].

1.1.2 Performance Evaluation

A number of measures are commonly used to evaluate the overall performance and effectiveness of a biometric system. Unlike the password-based authentication systems, the biometric systems can hardly achieve a perfect match between two biometric features acquired from the same subject. Therefore, the comparison between any two features computed from the same biometric trait is measured in terms of degree of similarity. Such comparison usually generates a similarity score to indicate the similarity between the two compared biometric features. A similarity score computed from two biometric features of the same subject is known as a genuine score. While the result of the similarity comparison between two biometric features originating from different subjects is known as an imposter score.

There are two kinds of errors can be induced from such similarity comparison: *false accept* (false match) and *false reject* (false non-match). The computed genuine or imposter score is typically compared (through binary comparison) with respect to a predetermined threshold T to determine the validity of the claimed identity. For example, an imposter score which exceeds T results in a false accept; a genuine score which falls below T results in a false reject. The performance of a biometric system can be evaluated in terms of two variables: false acceptance rate/false match rate (FAR/FMR) and false rejection rate/false non-match rate (FRR/FNMR). The FAR indicates the percentage of false accept cases while the FRR indicates the percentage of false reject cases. Sometimes, the FRR is represented as the percentage of genuine acceptance cases known as genuine acceptance rate (GAR), *i.e.* $GAR = 1 - FRR$. The tradeoff between the FAR and FRR (or GAR) can be described using a receiver operating characteristic (ROC) curve, which plots the GAR/FRR against the FAR in a semi-logarithmic scale. The Equal Error Rate (EER) which indicates the point where FAR intersects with the FRR ($FAR = FRR$) is a single variable commonly used to show the performance of a biometric system. A lower EER value is preferred as it indicates better recognition performance. The *d*-prime value (also known as decidability index), d', as defined in Equation (1.1), is another commonly used indicator to show the performance of a biometric system.

$$d' = \frac{|\mu_{genuine} - \mu_{imposter}|}{\sqrt{(\sigma^2_{genuine} + \sigma^2_{imposter})}}, \tag{1.1}$$

where $\mu_{genuine}$ and $\mu_{imposter}$ denote the means of genuine and imposter scores, respectively; $\sigma_{genuine}$ and $\sigma_{imposter}$ denotes the variance of the genuine and imposter scores, respectively. Therefore, the *d*-prime is a measurement of the separation between means of the genuine and imposter probability densities in standard deviation units. In the case of identification, a cumulative match characteristic (CMC) curve is commonly employed to summarize the percentage of the correct match occurs in the top $k = 1,2, \dots, N$ ranking, where N denotes the number of the enrolled subjects. Figure 1.5 shows examples of the ROC and CMC curves computed using the similarity scores obtained from the CASIA.v3-Lamp database [7].

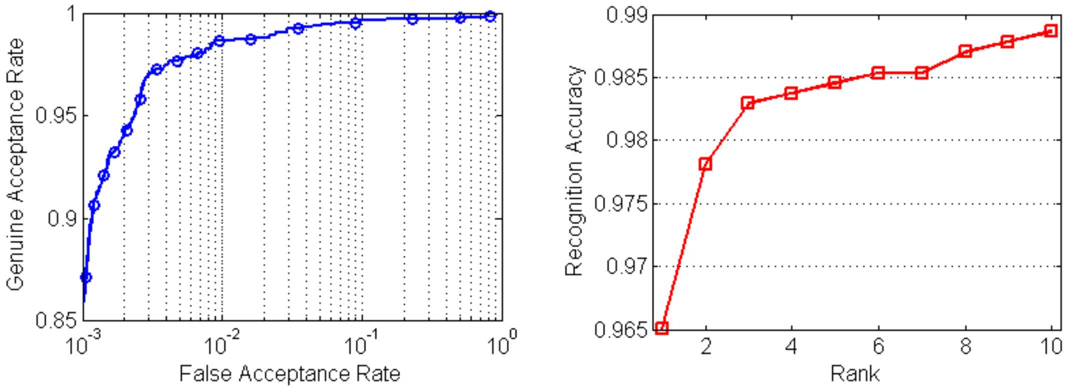

(a) ROC curve (b) CMC curve

Figure 1.5: The performance of a biometric system evaluated using ROC and CMC curves.

1.2 The Human Eye and Iris

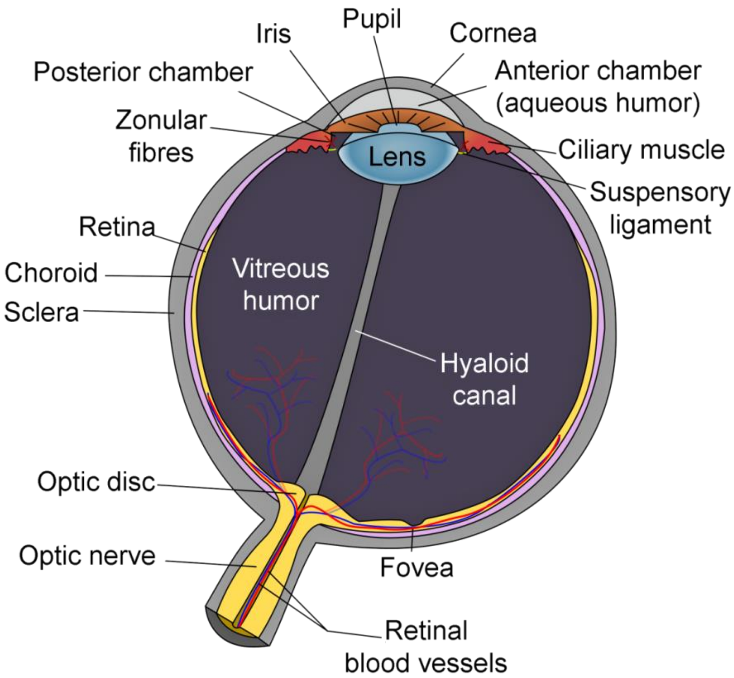

Figure 1.6: Anatomy of the human eye[b].

The human eye is part of the visual system which takes in light rays and converts them to a neural signal for further analysis and interpretation by the brain.

[b] © Soerfm / CC-BY-SA-3.0
http://commons.wikimedia.org/wiki/File%3ASchematic_diagram_of_the_human_eye_en-edit.png

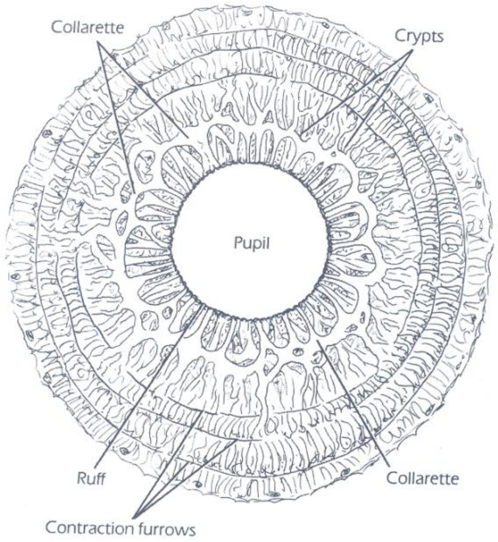

(a) Anterior surface

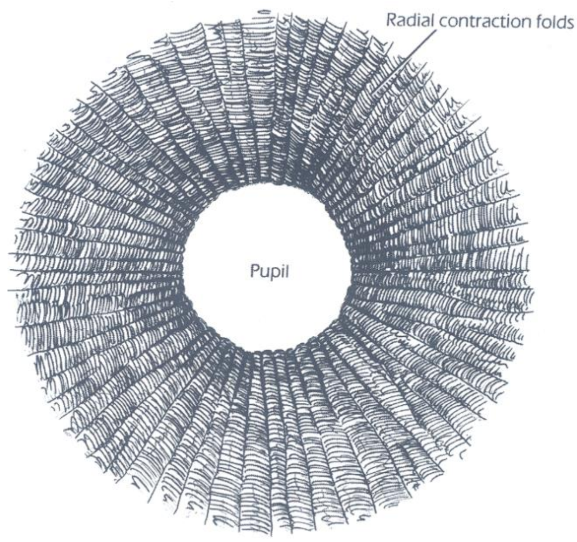

(b) Posterior surface

Figure 1.7: The anterior and posterior surfaces of the iris (pictures from [19]).

The eye resembling the shape of a globe which consists of three spaces: anterior chamber, posterior chamber and vitreous chamber, as illustrated in Figure 1.6 [19], [20], [21]. The anterior chamber is bounded by the cornea, iris and the anterior surface of the lens. The posterior chamber is situated behind the iris and surrounds the equator of the lens. The vitreous chamber, which occupies the largest space of the eye, is bounded by the inner retina layer and the lens. The *sclera* is the opaque white of the eye formed by tough and fibrous tissue to provide protection for the shape of the eyeball and the resistance to the intraocular pressure. The transparent *cornea* is convex as seen from the front which responsible for allowing the light rays entering the eye and focus on the retina by refraction. The *iris* is a thin, contractile and pigmented diaphragm which regulates the amount of light entering the *pupil*. The color of the iris varies from light blue to dark brown, which is determined by the pigment in the melanocytes. Figure 1.7 shows the anterior and posterior surfaces of the iris. The anterior surface is separated into two regions known as central *pupillary zone* and a peripheral *ciliary zone*. The wavy *collarette* acts as a circular demarcation line between pupillary and ciliary zones. The *contraction furrows* responsible to regulate the contraction and dilation of the iris as the pupil dilates or contracts. *Crypts* are adjacent to the collarette on both the pupillary and ciliary sides which is enclosed by rich radially arranged trabeculae meshwork. The posterior surface of the iris is relatively smoother and more uniform than the anterior surface. The posterior surface shows a number of radial folds such as the contraction folds, structural folds and circular folds [19], [22].

1.3 Iris Recognition

Iris recognition is one of the biometric technologies to provide automated *non-invasive* personal recognition based on the distinctive characteristic extracted from the iris. The human iris exhibits extremely complex texture patterns which are relatively stable throughout a human's lifespan. Such texture patterns are epigenetic and are widely regarded to be highly distinctive. For example, the irises of left and right eyes are different; the irises of identical twins are different [1], [23], [24], [25]. Figure 1.8 shows the complex texture patterns of an iris where the collarette, crypts, ridges and furrow can be observed [26], [27].

The idea of automated iris recognition was first proposed by Flom and Safir and patented in 1987 [28]. However, there had no actual implementation to perform the automated iris recognition based on their described proposal. The earliest workable automated iris recognition solutions were perhaps the approaches as proposed in [23], [29], [30], which serve as a reference model for most of the existing commercial iris biometrics technology. Based on their proposed model, an iris recognition system is generally composed of four modules: image acquisition, iris segmentation, feature encoding and matching. The image acquisition module involves the acquisition of the iris or eye image with sufficient image quality which can be useful for recognition. For example, the diameter of the iris image being acquired should have at least 140 pixels as suggested in [31] or 200 pixels as suggested by the International Organization for Standardization (ISO) [32]. Nearly all the existing commercial iris recognition systems use the NIR (near-infrared) in the 700-900 nm range to illuminate the iris[c], and require *full cooperation* from the users to provide their iris images at the standoff distance between one and

[c] The face/eye region is generally acquired simultaneously and can be employed to provide multimodal biometrics solutions [136], [137].

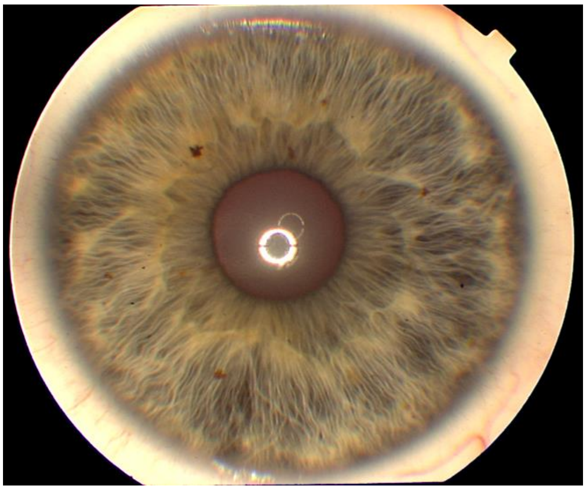

Figure 1.8: The human iris exhibits extremely rich texture patterns (picture from [33], ID: 015L_2).

three feet. With the advancement of the imaging technology, iris images can now be acquired conveniently with less cooperation from the users and be acquired *at-a-distance* (3-8 m), as shown in Figure 1.9 [34], [35]. It is worth nothing that precaution should be paid for the use of the NIR illumination in the image acquisition as the excessive NIR illumination level can cause permanent damage to the human eyes [36], [37], [38]. Recently, attempts of using visible illumination imaging are proposed to acquire iris images *at-a-distance* (between three to ten meters) and under *less constrained environments* [39], [40].

(a) Portal of the "Iris on the Move" project (picture from [41], [34]).

(b) An ongoing project of iris acquisition system which is capable to acquire images at distance up to 8m (picture from [35]).

Figure 1.9: Iris image acquisition *at-a-distance* in laboratory environment.

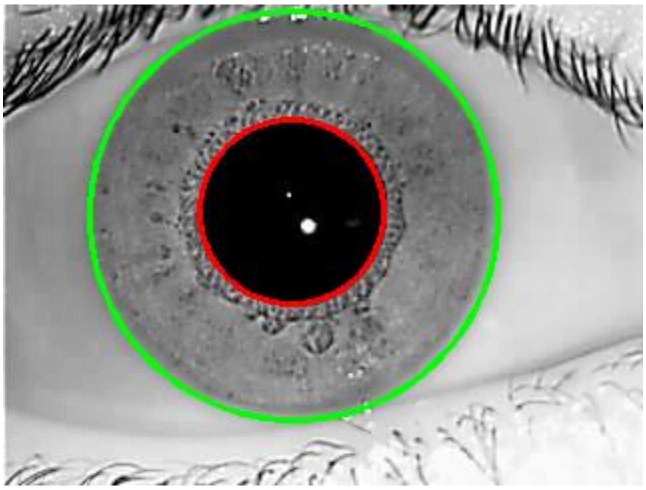

Figure 1.10: Sample segmentation result for an iris image (ID: 001_09) from IITD iris database [42].

The purpose of the segmentation is to localize the valid/useful iris region from the acquired iris image. Daugman's integro-differential operator [31], [43] perhaps is one of the remarkable iris segmentation approaches and has been employed in almost all existing commercial iris biometrics systems. The iris is assumed to have a circular boundary and can be represented with three parameters: the coordinates of the center of the circle, x_c and y_c, and the radius r. The integro-differential operator attempts to locate the iris boundary by searching the parameter space to maximize

$$\max_{(x_c,\, y_c, r)} \left| G_\sigma(r) * \frac{\partial}{\partial r} \oint_{(x_c,\, y_c, r)} \frac{I(x,y)}{2\pi r} ds \right|, \tag{1.2}$$

where $I(x,y)$ denotes the intensity value of the iris image at location (x,y); $G_\sigma(r)$ with the standard deviation σ serves as a Gaussian smoothing function, and '$*$' denotes the convolution operator. Often, the commonly known noise[d] sources such as eyelid, eyelashes, shadow and reflection highlight are also being identified during the iris segmentation process. Figure 1.10 shows a sample iris segmentation result (superimposed red and green circles) obtained by using a publicly available open-source software distributed by NIST (National Institute of Standards and Technology) [44], [45].

[d] We use the generic term *noise* to refer to those commonly observed noise sources in the iris image.

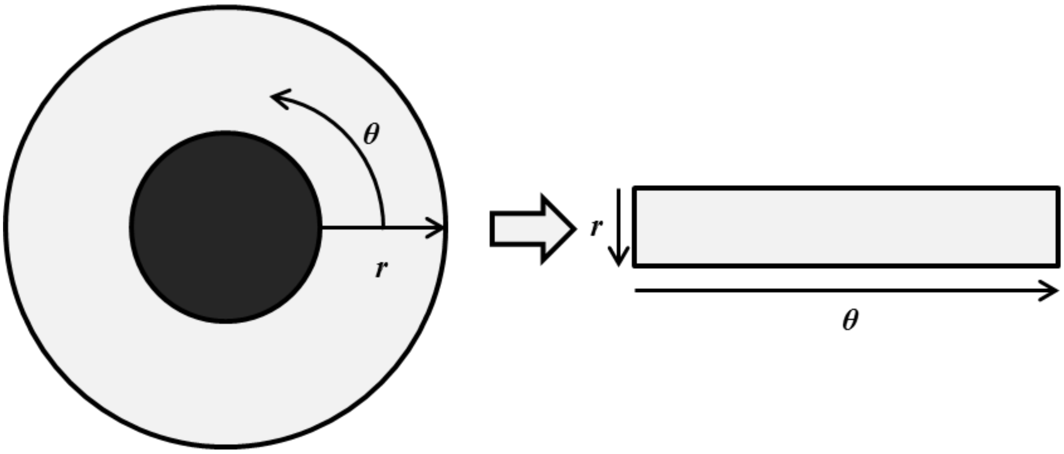

Figure 1.11: Iris normalization based on Daugman's rubber sheet model.

The encoding module aims to recover distinctive iris features which can be useful in distinguishing each individual accurately. In order to account for the varying iris size due to the imaging distance between the eye and the acquisition device, as well as the pupillary response to ambient light which results in dilation or constriction of the pupil, normalization is applied before the feature encoding. Daugman's rubber sheet model as illustrated in Figure 1.11 performs a mapping from the Cartesian coordinates (x, y) to the doubly-dimensionless polar coordinates (r, θ):

$$I\big(x(r,\theta), y(r,\theta)\big) \rightarrow I(r,\theta)\,, \tag{1.3}$$

$$\begin{bmatrix} x(r,\theta) \\ y(r,\theta) \end{bmatrix} = \begin{bmatrix} x_p(\theta) & x_s(\theta) \\ y_p(\theta) & y_s(\theta) \end{bmatrix} \begin{bmatrix} 1-r \\ r \end{bmatrix}, \tag{1.4}$$

where (x_p, y_p) denote the Cartesian coordinates of the pupillary contour; (x_s, y_s) denote the Cartesian coordinates of the outer iris contour. The parameters $r \in [0,1]$ spans the unit interval and θ is the angle span the interval in $[0,2\pi]$. Such coordinate mapping system has been adopted as ISO standard 197946 [32]. The normalized iris image has achieved the invariance to the size of the iris and the pupillary response. Feature encoding approach is then applied to the normalized iris image in order to recover discriminative iris features. Examples of the feature encoding methods as commonly reported in the iris biometrics literature are 2D Gabor filter [29], [31], [43], [46] 1D Log-Gabor filter [47], [48], [49], wavelet transform [50], [51], ordinal filter [52], [53] and DCT (discrete cosine transform) [54]. The iris features as recovered by different feature encoding methods are generally described using the representation which can allow the efficient matching. Such representation can be generally divided into two categories: binary representation and real-valued feature vector [24]. The binary representation, or typically referred to as *iris code*, produces the binary representation

Table 1.1: Recent promising works in the iris biometrics (between year 2007 and 2013).

Year	**Ref.**	**Methodology**		**Database and operating illumination ($^{*\wedge\#+}$)**
		Segmentation	**Encoding**	
2007	[54]	Hough transform to localize pupil. Circular iris boundary is searched from the horizontal line through the localized pupil center	Discrete Cosine Transform (DCT)	CASIA$^{*\wedge}$, BATH$^{\wedge}$
2007	[43]	Coarse segmentation using Integro-differential operator and boundaries refinement based on active contour model	2D Gabor filters	ICE.v1$^{\wedge}$, UAE$^{*\wedge}$
2008	[55]	Pupil and iris are modeled as ellipse shape. Boundaries refinement through modified Mumford–Shah functional	Global features encoded using Log-Gabor. Local topological features encoded using Euler numbers	CASIA.v3$^{\wedge}$, ICE2005$^{\wedge}$, UBIRIS.v1$^{\#}$
2008	[56]	Gradient-based approach. Pupil is modeled as ellipse while iris is assumed to be circular	2D Discrete Fourier Transform (DFT)	CASIA.v1$^{\wedge}$, CASIA.v2$^{\wedge}$, ICE2005$^{\wedge}$
2009	[48]	IrisBEE-similar software	Log-Gabor with estimation of fragile bits	ICE$^{\wedge}$
2009	[57]	Use of modified algorithm based on [49]	Global and local features encoded using Gabor phase	ICE2005$^{\wedge}$, CASIA.v2$^{\wedge}$, CBS$^{\wedge *}$
2009	[53]	Iris detection using AdaBoost. Localize pupil and iris based on iterative pulling and pushing method	Ordinal filters	ICE.v1$^{\wedge}$, CASIA.v3-Lamp$^{\wedge}$
2009	[58]	Based on Geodesic active	2D Gabor filters	WVU Non-ideal$^{\wedge}$,

		contour model		CASIA.v3-Interval^
2009	[52]	N/A	Ordinal filters	BATH^, CASIA .v1^, CASIA.v3-Interval^, ICE2005^
2010	[51]	Pupil is localized based on the intensity information. Iris is localized using a voting-based scheme.	Log-Gabor, Haar wavelet, DCT, DFT	IITD.v1^, CASIA.v1, CASIA.v3-Lamp^
2010	[59]	Constellation model based on Integro-differential operator	N/A	UBIRIS.v1#, UBIRIS.v2#
2010	[60]	Use of trained neural network classifiers to classify pupil and iris pixels	N/A	UBIRIS.v2#, FRGC#, FERET+, ICE2006^
2011	[61]	Use of existing publicly available source code [49]	Gabor filters	ICE2005^, ND-IRIS-0405^, MBGC^
2011	[62]	Use approach [53]	Ordinal filters with weight map	CASIA.v3-Lamp^, ICE2005^, BATH^
2012	[63]	Hough transform	Dynamic features (see the corresponding reference for details)	Internally constructed video-based iris database*^#
2012	[64]	Manually segmented	Multiple features such as ordinal, color, SIFT, etc. computed from iris and periocular regions.	UBIRIS.v2#
2012	[65]	Neural-network/SVM trained classifiers using Zernike moments features to classify iris pixels	Log-Gabor	UBIRIS.v2#, FRGC#, CASIA.v4-distance^
2013	[66]	Random walker-based segmentation	Log-Gabor and Dense SIFT computed from iris and periocular regions	UBIRIS.v2#, FRGC#, CASIA.v4-distance^

Remark:

N/A *Not available/applicable*
* *Not publicly available*
^ *NIR illumination*
# *Visible illumination*
+ *Grayscale image*

by applying the coarse quantization to the recovered iris features. Refs. [31], [43], [46], [47], [48], [49], [52], [53], [54] are some of the representative works of employing the iris code as the feature representation. On the other hand, the real-valued feature vector uses the *raw* values computed from the encoding methods to form the feature vector. The representative works of using the real-valued feature vector as iris feature representation are reported in [23], [50], [51], [54], [56], [61]. Table 1.1 attempts to summarize the recent promising works in iris biometrics reported in the literature.

The matching module is responsible to compute the similarity between the query iris template and the template(s) stored in the database (gallery). Depends on the mode and the requirement of the application (see Section 1.1.1), the comparison can be either an one-to-one or one-to-many matching. For example, the similarity score between a query iris code $IrisCode_{query}$ and a gallery iris code $IrisCode_{gallery}$ can be computed in terms of the total number of disagreeing iris bits, *i.e.* Hamming distance (HD), as defined as:

$$HD = \frac{\left\|\left(IrisCode_{query} \oplus IrisCode_{gallery}\right) \cap mask_{query} \cap mask_{gallery}\right\|}{\left\|mask_{query} \cap mask_{gallery}\right\|}, \qquad (1.5)$$

where the '$\oplus$' and '$\cap$' denote the *Exclusive-or* and *And* operators, respectively. The $mask_{query}$ and $mask_{gallery}$ represent the binary masks which mask out the portion of occluded iris bits as identified in the segmentation module. Such binary mask has the same dimension as the iris code. The HD is normalized into the unit range $[0,1]$ with the value closes to zero indicates higher similarity while the value closes to one indicates higher dissimilarity between any two compared iris codes.

1.4 Organization of Thesis

This thesis details my research work in improving the iris segmentation and recognition strategies which can be more effective and accurate for eye images acquired at-a-distance and under less constrained environments using either visible or NIR illumination imaging. In Chapter 2, some background on the recent promising iris segmentation and feature encoding approaches which are developed for the conventional NIR based iris recognition systems is provided. Chapter 3 offers some background on the recent development of the iris recognition at-a-distance and under less constrained environments.

In Chapter 4, a robust and efficient iris segmentation strategy which can be more effectively for eye images acquired distantly and under less constrained environments is detailed. In Chapter 5, we detail the joint encoding strategy from a global iris bits stabilization encoding and a localized Zernike moments phase-based encoding. The complementary matching information from such joint strategy has shown to provide more accurate recognition accuracy for the iris recognition at-a-distance and under less constrained environments. Chapter 6 investigates recognition performance from various commonly employed periocular features. We show that the joint matching information from simultaneously acquired iris and periocular features can achieve even better recognition accuracy than any of the iris or periocular features alone. In Chapter 7, a computationally attractive binary encoding strategy by exploiting the geometric information for localized iris encoding is presented. Such geometric-based iris encoding strategy is aimed to provide an alternative to the global iris bits stabilization encoding which incurs relatively higher computational complexity. We show that the joint matching information from the geometric based encoding and Zernike moments phase-based encoding strategies can offer better or comparable recognition performance but with reduced computational complexity. Chapter 8 provides concluding remarks and suggestions for further work.

CHAPTER 2

Iris Recognition under Constrained Environment

Iris biometrics has emerged as one of well-established biometric technologies to provide reliable human recognition with many existing successfully deployed large-scale applications. For example, iris biometrics has been used for border control in The United Arab Emirates (UAE) with the reported 2.7 billion iris cross-comparisons daily [67], [14], the Unique ID (*Aaahar*) project for millions of citizens in India [15], access control into some security zones and *etc*. Almost all the existing commercial iris recognition systems employ NIR illumination in the 700-900 nm range to illuminate the iris images which can better reveal the iris textures and provide sufficient contrast even for darkly pigmented irises. Such NIR-based iris recognition systems are designed to work under constrained environment in order to mitigate the influence from the commonly observed noise sources such as illumination changes, occlusions from eyeglasses, eyelashes, hair and reflections. In addition, full cooperation is highly expected from the users, *e.g.* stop-and-stare as illustrated in Figure 2.1, in order to provide their eye/iris images with sufficient image quality which can be useful for the recognition.

Figure 2.1: A commercial NIR-based iris recognition system deployed in UAE (picture from [68]).

Remarkable iris recognition accuracy has been reported by many existing state-of-the-art iris recognition algorithms on those iris images acquired using NIR illumination under the constrained environment [43], [48], [51], [53], [54] [56]. Therefore, this chapter aims to provide review into some of these state-of-the-art iris recognition algorithms particularly in the context of iris segmentation, feature encoding and matching. Lastly, we discuss about the limitations and challenges of the existing NIR-based iris recognition systems.

2.1 Iris Segmentation

Iris segmentation is a process to localize the valid iris region from the eye image. The iris is assumed to resembling a circular shape (annulus) as seen from a frontally acquired iris image. Such assumption has since become the basis for most iris segmentation methods that are developed for the iris images acquired using *NIR* illumination under the *constrained* environment in order to localize the iris region. Therefore, this section serves to provide review on several representative works on the iris segmentation methods.

2.1.1 Daugman's Method

Daugman's method is a well-known technique which has been employed by most commercial NIR-based iris recognition systems. In his earlier paper [31], the iris and pupil are modeled as two circles, which can be approximated using the Integro-differential operator as given in Equation (1.2). However, the latest findings show that the pupil and the iris are not necessary to resembling circular shape. In order to better approximate such noncircular boundaries, Daugman proposed an improvement over his earlier work to approximate the pupillary and limbic boundaries using the active contour model based on the Fourier series [43]. The M Fourier coefficients $\{C_k\}_{k=0}^{M-1}$ for N regularly sampled angular edge points (pupil/iris) $\{r_\theta\}_{\theta=0}^{N-1}$ are given as follows:

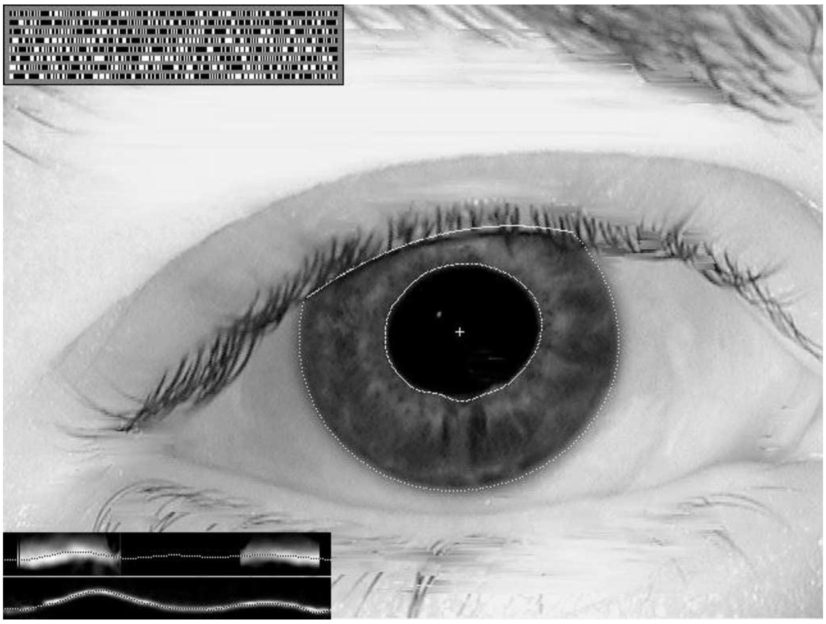

Figure 2.2: Pupillary and limbic boundaries approximation using active contour model (picture from [43]).

$$C_k = \sum_{\theta=0}^{N-1} r\theta e^{-2\pi ik\theta/N}. \tag{2.1}$$

Therefore, the approximation to the boundary edge points can be computed by inverse of the M discrete Fourier coefficients, as given as follows:

$$R_\theta = \frac{1}{N} \sum_{k=0}^{M-1} C_k e^{2\pi ik\theta/N}. \tag{2.2}$$

Figure 2.2 shows a sample result obtained from the approximation based on the active contour model on a preprocessed iris image from ICE dataset. It can be observed that the boundary of the non-circular pupil can now be better estimated based on the active contour model. In order to reduce the influence from the eyelids, the Equation (1.2) is again employed to localize the eyelids, which are modeled as two parabolic curves. A statistical inference model based on the intensity distribution from the localized iris region is used to compute a threshold for separating the eyelashes and shadow.

2.1.2 Kazuyuki *et al.* Method

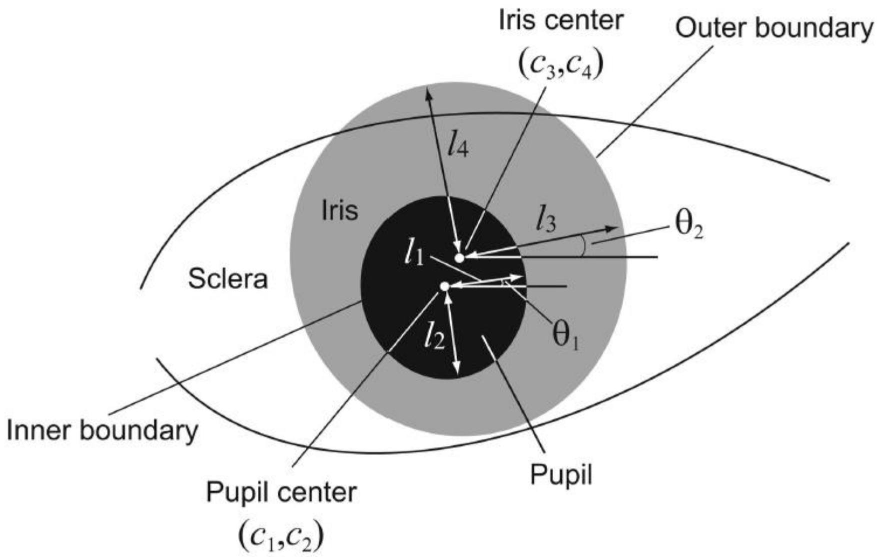

Figure 2.3: Deformable iris model (picture from [56]).

Kazuyuki *et. al* proposed a deformable iris model to approximate the pupillary and limbic boundaries, as illustrated in Figure 2.3 [56]. Firstly, an iterative search approach is employed to find the initial pupil center (c_1, c_2) from the binarized iris image. Then, the pupillary and limbic boundaries can be approximated by maximizing the following:

$$|S(l_1 + \Delta l_1, l_1 + \Delta l_1, c_1, c_2, \theta_1) - S(l_1, l_1, c_1, c_2, \theta_1)|, \tag{2.3}$$

$$S(l_1, l_1, c_1, c_2, \theta_1) = \sum_{n=0}^{N-1} I\big(p_1(n), p_2(n)\big), \tag{2.4}$$

where Δl_1 and Δl_2 denote the step sizes; θ_1 and θ_2 denote the angles; S denotes the contour summation of the intensity values of N sampling points from the iris image I. The coordinates of the contour can be obtained using: $p_1(n) = l_1 \cos\theta_1 \cos\left(\frac{2\pi}{N}n\right) - l_2 \sin\theta_1 \sin\left(\frac{2\pi}{N}n\right) + c_1$ and $p_2(n) = l_1 \sin\theta_1 \cos\left(\frac{2\pi}{N}n\right) - l_2 \cos\theta_1 \sin\left(\frac{2\pi}{N}n\right) + c_2$, respectively. In their approach, the pupil is modeled using ellipse shape while the iris is modeled using circle shape. In order to avoid the influence from the eyelashes, only the lower half of the localized iris region is employed for encoding and matching.

2.1.3 He *et al.* Method

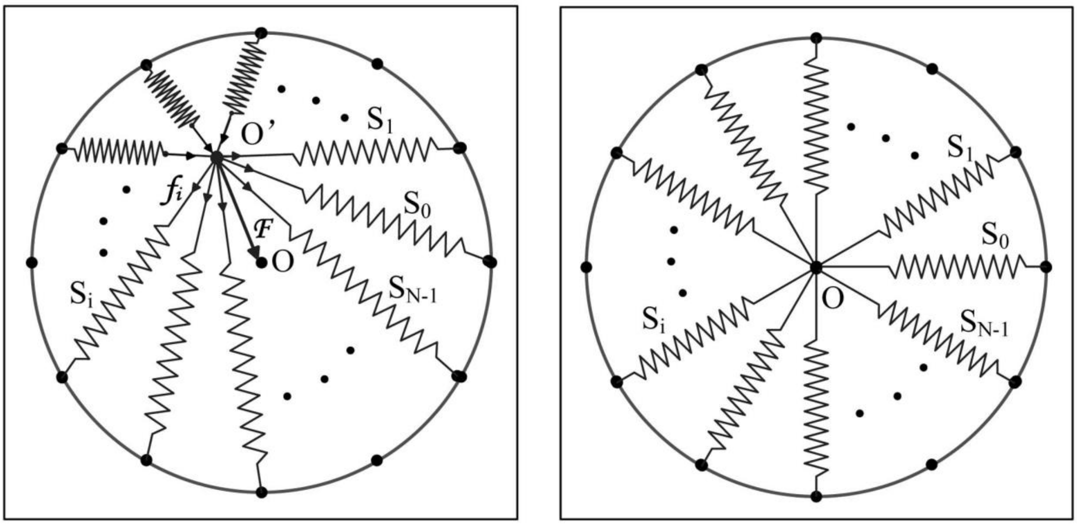

(a) The springs are not in the equilibrium position as different forces are produced by each spring

(b) The springs produce the identical force and all springs are restored to its equilibrium position

Figure 2.4: The pulling and pushing method (pictures from [53]).

The approach proposed by He *et al.* first performs a coarse detection of iris by using a trained Adaboost-cascade iris detector in order to obtain an initial estimation for the iris location. The localization of the pupillary and limbic boundaries is then performed by using pulling and pushing (PP) method [69], [53]. The PP method attempts to restore the forces as produced by the N identical imaginary springs $\{S_i\}_{i=0}^{N-1}$ to its equilibrium (neutral) position, as illustrated in Figure 2.4. The force produced by each spring is given as follows:

$$\vec{f_i} = -k(\bar{R} - r_i)\vec{e_i}, \qquad i = 0,1,\dots,N-1, \tag{2.5}$$

where $k = 1/N$ represents the spring constant; r_i denotes the length of the corresponding spring S_i; $\vec{e_i}$ indicates the direction of the spring radiating from the estimated center O'. The $\overline{R}$ denotes the equilibrium length of the springs and can be obtained from:

$$\overline{R} = \frac{1}{N} \sum_{i=0}^{N-1} \overline{O'_p P_i}. \tag{2.6}$$

where P_i denotes the detected pupillary/limbic edge point. The localization of the eyelids is performed by measuring the shape similarity between the detected candidate eyelid edge points and the three generic eyelid models established statistically from the training samples. The model which resembles the most similarity is used to eliminate the noisy candidate eyelid edge points. The remaining candidate eyelid edge points are then used to approximate the eyelid by using the parabolic curve fitting technique. In order to detect the eyelash and shadow noise, a statistically learned prediction model is used to estimate an appropriate threshold to exclude those occluded pixels from the localized iris region.

2.1.4 Kumar and Passi's Method

The segmentation algorithm [51] proposed by Kumar and Passi first performs a row-wise scanning of the image to search for the consecutive low intensity pixels whose values are less than a predefined threshold. The heuristic is made here by assuming that the longest consecutive of such thresholded pixels must correspond to the diameter of the pupil. To localize the limbic boundary, a voting-based scheme is employed. A 20×20 window centered at the localized pupil center is assumed to be the candidates to test for the iris center. The voting begins by varying the radiuses (typically in the monotonic order) of the search circle from the edge map produced by the Canny edge detector. The circumference pixel which encounters the edge points contributes a vote. Therefore, the parameters of the circle, *i.e.* iris center and radius, which accumulates the maximum vote is used to approximate the limbic

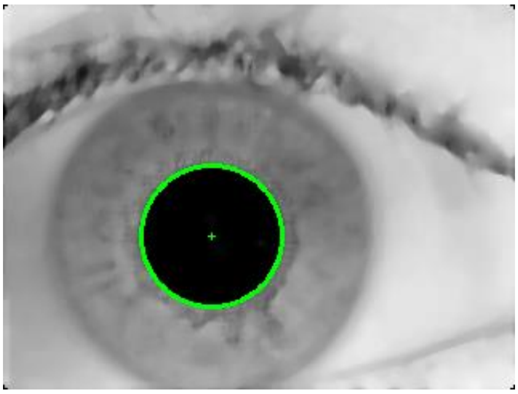

(a) The localized pupillary boundary

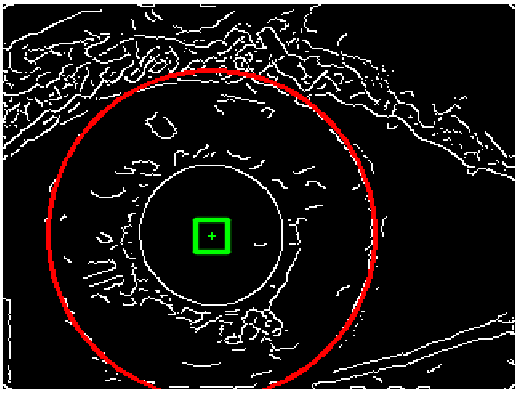

(b) Localization of limbic boundary from the candidate iris centers as indicated by the superimposed rectangle

Figure 2.5: Sample segmentation result (ID: 001_01) from IITD iris database [42]

boundary. Figure 2.5 shows a sample segmentation result produced by the Kumar's segmentation algorithm.

2.1.5 Other Methods

The approach presented in [54] models the pupil and iris as two circles. The pupillary boundary is approximated using the Hough transform from the generated edge map. The dominant row which passes through the localized pupil center is used to search for the limbic boundary, also using the Hough transform. The approach presented in [55] models pupil and iris as two ellipses. A coarse localization is performed to obtain the initial contours of the pupillary and limbic boundaries. The coarsely localized boundaries are further refined based on the modified Mumford–Shah functional. The approach presented in [58] employs a circle fitting procedure to approximate the pupillary boundary from the binarized iris image while the limbic boundary is approximated using geodesic active contour model. The approach presented in [70] employs a graph-based technique to represent the line segments from the edge map as produced by applying the Canny edge detector to the iris image. A likelihood test which is based on the Normalized Cuts approach is employed to segment the circular-like contours computed from the line segments.

The coarsely segmented circular contours are further refined by using the Hough circle transform.

2.2 Feature Encoding and Matching

As shown in Figure 1.8, the human iris exhibits extremely rich texture patterns which have been widely regarded to be unique among each individual. The feature encoding is a process to recover the distinctive features from such complex texture patterns which can be employed for human recognition. The matching takes the similarity (dissimilarity) measurement between any two recovered features and outputs a similarity score which can be used for decision making. In this section, we provide review on several promising efforts on the feature encoding and matching methods.

2.2.1 Gabor Filters

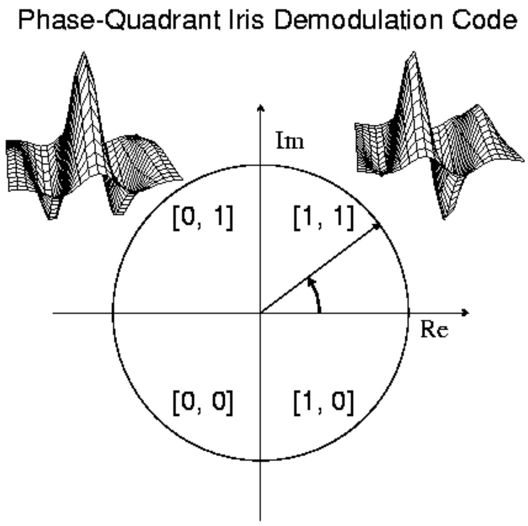

Figure 2.6: Quantization of the phase-only information in order to produce the binary representation, *i.e.* iris code (picture from [31]).

Gabor filters have been shown to exhibit desirable characteristics such as spatial-frequency selectivity and orientation selectivity which can be used to characterize the textural information of the iris, as proposed by Daugman [29], [31]. A 2D Gabor filter computed over an image domain (x, y) is given as follows:

$$G(x,y) = \exp\left(-\pi\left[\frac{(x-x_0)^2}{\alpha^2} + \frac{(y-y_0)^2}{\beta^2}\right]\right).\exp(-2\pi i[u_0(x-x_0) + v_0(y-y_0)]) \quad (2.7)$$

where (x_0, y_0) indicates the center of the Gaussian filter; α and β represent the width and length of the filter, respectively; (u_0, v_0) specifies the modulation with spatial frequency $w_0 = \sqrt{u_0^2 + v_0^2}$ and orientation $\theta = \arctan(v_0/u_0)$. In order to encode the iris texture, the 2D Gabor filter is applied to the normalized iris images (unwrapped iris images). Phase-only information from the 2D Gabor filter response is coarsely quantized into binary code (iris code) according to the phase-quadrant, as illustrated in Figure 2.6. Therefore, iris recognition can be performed by computing the Hamming distance between two iris codes using the Equation (1.5).

2.2.2 Log-Gabor Filters

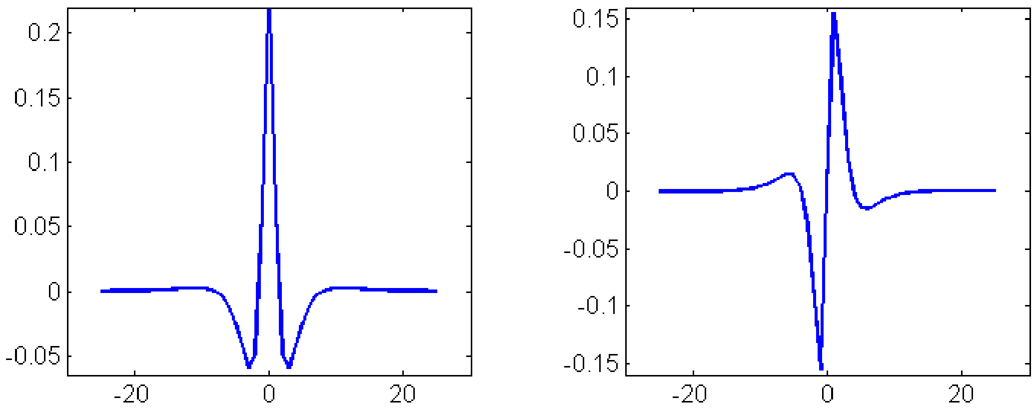

(a) Real component (b) Imaginary component

Figure 2.7: Visualization of the Log-Gabor filters in spatial domain with the parameters, $f_0 = 16$ and $\sigma_f = 0.55$.

Log-Gabor filters are another commonly used phase encoding method (*e.g.* [47], [51], [61]) as an alternative to the Gabor filters as it offers several advantages over the Gabor filters. Gabor filters have been observed to over represent the low frequency components and under represent the high frequency components in any encoding [71]. Furthermore, a Gabor filter will have DC-component in its even-symmetric component if the bandwidth is greater than one octave [49], [72]. In contrast, a Log-Gabor filter with zero DC-component can always be constructed at any arbitrary bandwidth. The Log-Gabor filters are expected to better encode natural images due to the extended tails at the high frequency end [71]. The frequency response of Log-Gabor in the frequency domain is defined as follows:

$$G(f) = \exp\left(\frac{-\log\left(\frac{f}{f_0}\right)^2}{2\log\left(\frac{\sigma}{f_0}\right)^2}\right), \tag{2.8}$$

where f_0 denotes the central frequency and σ is the scaling factor. However, the denominator term σ/f_0 is usually expressed as a constant ratio value, σ_f, in order to obtain constant shape ratio filters [49]. Figure 2.7 shows an example of the Log-Gabor filter visualized in spatial domain. The matching of any two Log-Gabor encoded features can be done similarly as to the Section 2.2.1. Binary codes are constructed by quantizing the Log-Gabor filter response and the similarity can be measured by using the Hamming distance.

2.2.3 Ordinal Filters

Sun *et. al* proposed to encode iris features based on the ordinal measures, *i.e.*, relative comparison, between the building blocks constructed from the normalized iris region pixels [52]. The ordinal iris features can be extracted by using multilobe differential filters (MLDF), as defined as follows:

$$MLDF = C_p \sum_{i=1}^{N_p} \frac{1}{\sqrt{2\pi\sigma_{pi}}} \exp\left[\frac{-\left(X-\mu_{pi}\right)^2}{2\sigma_{pi}^2}\right] - C_n \sum_{j=1}^{N_n} \frac{1}{\sqrt{2\pi\sigma_{nj}}} \exp\left[\frac{-\left(X-\mu_{nj}\right)^2}{2\sigma_{nj}^2}\right]. \tag{2.9}$$

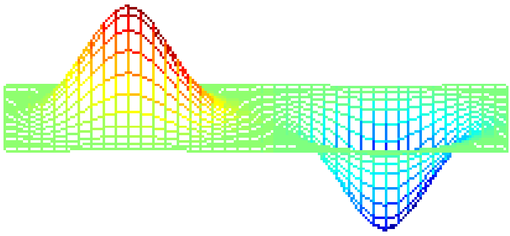

(a) Number of lobes = 2; orientation = 0; distance = 0

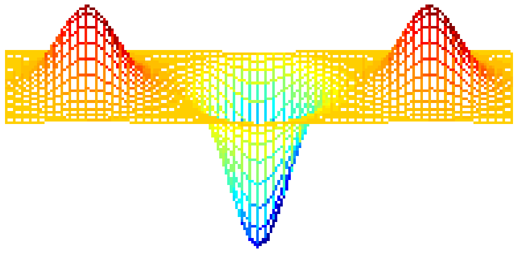

(b) Number of lobes = 3; orientation = 0; distance = 0

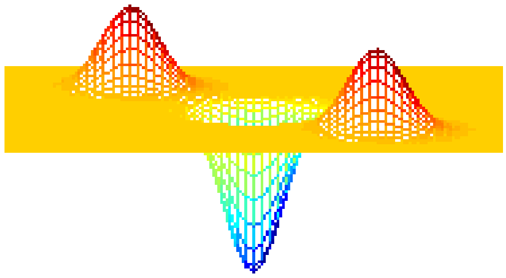

(c) Number of lobes = 3; orientation = 45-degree; distance = 0

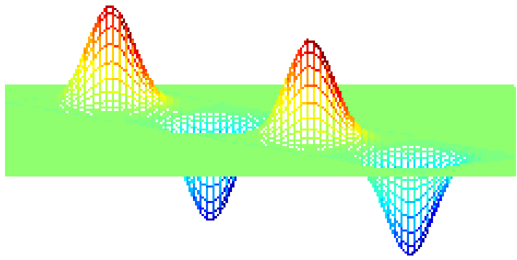

(d) Number of lobes = 4; orientation = 45-degree; distance = 0

Figure 2.8: Examples of the multilobe differential filters. All filters are constructed with the basic lobe size of 21×21 and $\sigma = 3.5$.

where μ and σ denote the center position and standard deviation the Gaussian filter, respectively; N_p and N_n indicate the numbers of positive and negative lobes, respectively; C_p and C_n are two coefficients used to ensure zero sum of the MLDF, *i.e.*, $C_p N_p = C_n N_n$. The MLDF offers a number of settings such as *scale*, *interlobe distance*, *orientation* and *number of lobes* to flexibly construct the filter which can be more adaptive to image structure. Figure 2.8 shows some examples of the MLDF constructed with different settings. The MLDF filter response is quantized into binary representation based on the sign of the filter response. Therefore, the matching of two ordinal features can be computed using the Equation (1.5).

2.2.4 Fragile Bits

The existence of the fragile (inconsistent) bits in the binary iris code was investigated by Hollingsworth *et al.* [47], [48], [73]. Such inconsistent bits are observed to be mainly caused by the coarse quantization of the phase response, particularly those near the axes of the complex plane. However, other possible causes such as segmentation, template alignment and choice of filter may possibly affect the consistency of bits in the binary iris code. In their papers, iris features were encoded with 1D Log-Gabor filters[e] and the phase response was quantized in order to obtain the binary iris code C. The procedure for estimating the fragile bits can be summarized as follows:

i. Given K iris codes $\boldsymbol{C}^j = \{C_i^j\}_{i=1}^K$ belong to class j. C_1^j is employed as a reference image.

ii. Align the rest of the iris codes $\{C_i^j\}_{i=2}^K$ with respect to the reference image by circularly shifting the iris bits. The rotation which produced the minimum Hamming distance was used for alignment.

iii. Calculate the frequency f that a bit is *flipped*, *i.e.*, a bit has a different value from the corresponding bit in the reference image. A threshold τ is used to mask the fragile bits. For example, Table 2.1 shows five iris codes ($K = 5$) and each of them consists of six bits. The last row indicates the frequency that a bit is flipped. Let $\tau = 0.3$, then a bit is considered as *fragile* if $f \geq \tau$. In this particular example, three bits are identified as fragile bits, and therefore are masked in order to exclude from matching.

Table 2.1: Estimation of fragile bits.

i	Iris Bits					
1 (reference)	1	0	0	1	1	0
2	0	0	0	1	0	0
3	0	0	1	0	0	1
4	0	0	0	1	1	0
5	1	0	0	1	0	1
$f =$	**0.6**	0	0.2	0.2	**0.6**	**0.4**

[e] Other feature encoding methods which generate the binary templates can be employed as well.

2.2.5 Personalized Weight Map

Ref. [62] provides an improvement work based on the phenomenon of fragile bits in the binary iris codes [48]. Instead of using a hard threshold τ to detect fragile bits, they proposed to weight every bit according to their stability/consistency, as can be derived from the fragile bit estimation approach. Therefore, the weight w for i-th bit for some K iris codes from class j can be obtained as follows:

$$w_i = 2\frac{m_1^2 + m_0^2}{(m_1 + m_0)^2} - 1, \tag{2.10}$$

where m_1 and m_0 indicate numbers of times the bit i being 1 and 0, respectively; and $m_1 + m_0 = K$. The set of the computed weight values is referred to as weight map, *i.e.* $W_j = \{w_1, \ldots, w_n\}$. The generated weight map W has the same dimensionality as the iris code which consists of n total bits. As similarly to [48], the weight map is considered to be personalized as it is computed for every user registered into the system. The similarity score between a query iris code $IrisCode_{query}$ and a gallery iris code $IrisCode_{gallery}$ with its corresponding weight map $W_{gallery}$ can be calculated using a modified Hamming distance, as given as follows:

$$HD_{gallery} = \frac{\|IrisCode_{query} \oplus IrisCode_{gallery}\| \times W_{gallery}}{\|W_{gallery}\|} \tag{2.11}$$

2.2.6 Other Methods

In ref. [56], iris features are encoded using 2D discrete Fourier transform (DFT). The similarity of the two DFT encoded features is measured using the phase correlation technique. The phase correlation produces a distinct sharp peak if the two features are similar, or vice versa. In ref. [54], the discrete cosine transform (DCT) is used to encode iris features. A binary code is generated from the zero-crossings of the differences between the DCT coefficients of adjacent patch vector. A modified Hamming distance function is used in their method to compute the similarity between two DCT encoded features. Krichen *et al.* use real-valued response from the Gabor filters to encode the iris features [57]. The similarity of two encoded iris features is computed using global and local normalized phase correlation method. Pillai *et al.* presents the first work by framing the iris recognition into sparse representation framework [74], [61]. A sparse dictionary is constructed from real-valued phase response of Log-Gabor filter generated from set of training images. Matching is performed by computing the approximation error between the query and the sparse recovery features. Ref. [75] presents another iris recognition approach based on the sparse representation techniques. Several key point based approaches (*e.g.* SIFT [76], DAISY [77]) are also suggested by several researchers for feature encoding and matching [78], [79], [80].

2.3 Summary

The survey as reported in [25] has shown the dramatically growth of the iris biometrics research in recent years. This chapter reviewed several promising approaches as reported from the iris biometric literatures, particularly, iris segmentation methods, feature encoding and matching methods. These approaches are mostly developed based on the eye images acquired from close distance using NIR illumination and under constrained environment. Therefore, further application of these approaches to the iris recognition at-a-distance and under less constrained environments pose several challenges (see CHAPTER 3). For example, illumination level of the eye images acquired under less constrained environments is expected to be varying and therefore it is challenging for the approaches [51], [56] to predetermine a hard threshold for localizing pupillary boundary. As such, development of effective segmentation and recognition strategies for the iris recognition at-a-distance and under less imaging constraints is highly desirable.

CHAPTER 3

Iris Recognition under Less Constrained Environments

Almost all existing commercial iris recognition systems are designed to operate under constrained environment, which expect high amount of cooperation from users to provide their eye images within very limited depth of view of the acquisition device (typically between 1-3ft.). In order to provide sufficient illumination, NIR in the range between 700-900 nm is commonly used to illuminate iris/eye region. Another advantage of using NIR illumination is to better reveal the iris textures and provide sufficient contrast between the iris and pupil regions. Recently, there have been some promising efforts to acquire iris/eye images under less constrained environments using visible imaging in order to overcome several limitations of the existing NIR-based iris recognition systems. In this chapter, we provide review on recent development of the iris biometrics, as well as the technologies to enable the iris recognition *at-a-distance* and under *less constrained environments*.

3.1 Relaxed Imaging Setup

Recent trend in the development of the biometric technologies has been driven more toward forensic and surveillance applications, especially after the tragedy of September 11 [6]. Such increasingly demand in the high security biometrics-based solutions are aimed to provide covert and negative identification, for example, identify suspect from a crowd. Therefore, relaxation of the rigid imaging constraints as imposed by the conventional NIR-based iris systems is necessary in order to allow iris images to be acquired at-a-distance and under less constrained environments. In order to overcome such limitations, Proença *et al.* proposed to use *visible imaging* for eye image acquisition and they had successfully imaged the eye images from up to eight meters away and under less constrained environments [39],

Figure 3.1: Less constrained imaging setup in a laboratory environment (picture from [40]).

[40]. Figure 3.1 shows the imaging setup in a laboratory environment used by Proença *et al.* for image acquisition. They had used a camera with CMOS sensor, *i.e.* Canon EOS 5D, with 12.8 million effective pixels to acquire eye images [40].

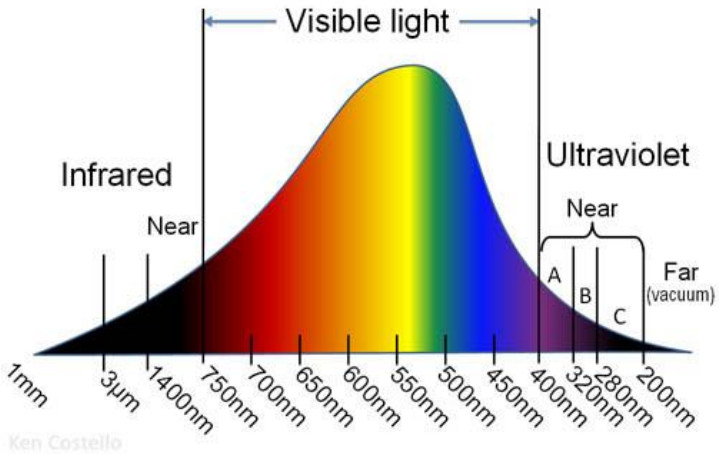

Figure 3.2: Electromagnetic spectrum (picture from [81]).

Visible imaging is referred to the use of imaging devices (*e.g.* filter, image sensor) which is sensitive to capture the electromagnetic radiation in the wavelength

Table 3.1: Comparison between NIR and visible illumination based iris recognition [65].

	NIR Illumination	*Visible Illumination*
User cooperation	High	Low
Image quality	Good	Degraded by noise
Application	Forensics, surveillance	Banking, national identity, physical and logical access
Imaging cost[f]	High	Low
Medical concern	High	Low
Recognition accuracy	High	Low
Key challenges	Technology is considered matured, nationwide large-scale applications are available	Robust iris segmentation, feature encoding

range between 400nm and 750nm (visible spectrum), as depicted in Figure 3.2. As mentioned earlier, the NIR illumination must be used in precaution in order to avoid the possible risk which can cause permanent eye damage. This is due to the fact that the human eye is not sensitive to the NIR illumination, and therefore does not instinctively respond with natural precautionary mechanisms such as blinking, aversion, and pupil contraction. In contrast, the visible spectrum does not have such limitation/constraint as the electromagnetic radiation within this range of spectrum can be perceived by the human eye, which can offer a more relaxed imaging environment to acquire images at-a-distance. Table 3.1 attempts to comparatively summarize the iris recognition at-a-distance using NIR and visible imaging. The advancement of the imaging technology has enabled the images to be conveniently acquired at-a-distance and under less constrained environments. Therefore, development of robust and efficient iris recognition approaches which can work under such relaxed imaging constraints can be highly essential.

3.1.1 Limitations and Challenges

Despite the flexibility offered by the visible imaging setups, the quality of the images acquired under such less constrained environments are usually degraded as

---

[f] The imaging cost we refer not only the camera itself but the acquisition setup in whole, for example, NIR illumination panels and band-pass filter [34], [35].

compared to those acquired under constrained environment using NIR imaging. The influences from the commonly observed noise sources such as illumination changes, occlusions from eyeglasses, eyelashes, hair and reflection is found to be severer in the eye images acquired using visible imaging, which pose the challenges to perform reliable and accurate iris recognition. Figure 3.3 shows several challenging eye

(a) C119_S1_I15 (b) C518_S1_I7

(c) C2_S1_I15 (d) C13_S1_I15

(e) C92_S2_I12 (f) C511_S1_I3

Figure 3.3: Sample eye images from UBIRIS.v2 database [40].

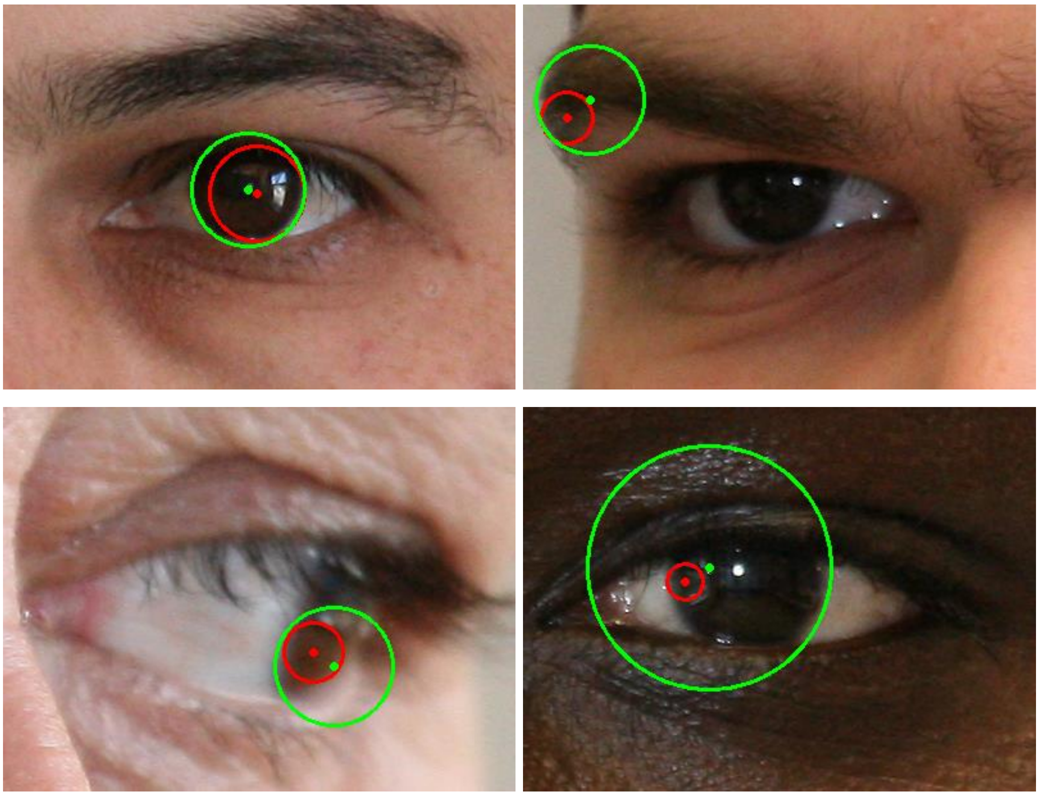

Figure 3.4: Segmentation results using gradient-based approach on eye images from UBIRIS.v2 database.

images which were acquired using visible imaging under less constrained environments. It can be observed from these images that the image quality is severely degraded due to the influences from noise. In addition, there is no clear contrast between iris and pupil regions for those darkly pigmented irises, which poses challenges for conventional gradient based approaches (see Section 2.1) to perform the iris segmentation, as depicted in Figure 3.4. Due to significant variations in segmented iris image quality, the existing feature encoding techniques may not be adequate to accurately characterize the iris features for those noisy iris images. Figure 3.5 shows two sets of the normalized iris images for two different users, each of the sets was acquired under different imaging setup. As can be observed, the normalized iris images in Figure 3.5(b) suffer more from the image quality and spatial variations. Therefore, robust feature encoding techniques which can be more tolerant to such variations, *e.g.* scale change, illumination change, defocus and translation, are of highly desired.

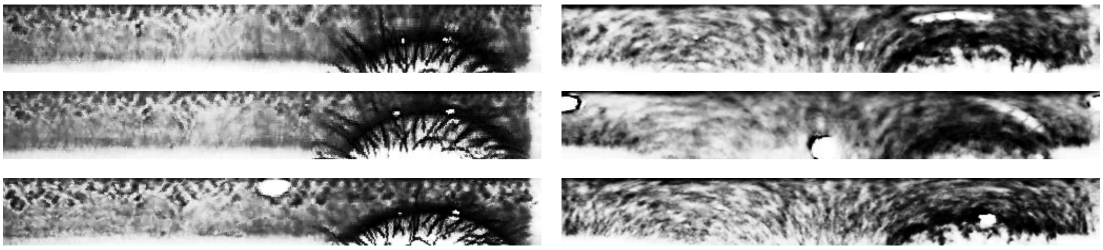

(a) Normalized iris images of same user acquired under constrained environment (Subject ID: 001, from CASIA.v3-Lamp database)

(b) Normalized iris images of same user acquired under less constrained environments (Subject ID: C079, from UBIRIS.v2 database)

Figure 3.5: Examples of normalized iris images acquired under constrained and less constrained environments.

3.2 Iris Segmentation

Distantly acquired eye image using visible imaging and under less constrained imaging environments requires development of robust segmentation algorithms in order to automatically extract the iris region. This section provides review on recent promising iris segmentation approaches developed for the eye images acquired at-a-distance and under less constrained environments, using either visible or NIR imaging.

3.2.1 Tan *et al.* Method

The iris segmentation proposed by Tan *et al.* placed on the first rank in the NICE.I (Noisy Iris Challenge Evaluation - Part I) competition [59], [82]. The NICE.I competition was initiated by SOCIA Lab in University of Beira Interior, Portugal with the objective to promote further research on the development of robust iris segmentation algorithms for those noisy iris images[g]. In their proposed algorithm,

[g] We use noisy iris images to refer to the iris/eye images acquired using visible imaging at-a-distance and under less constrained environments.

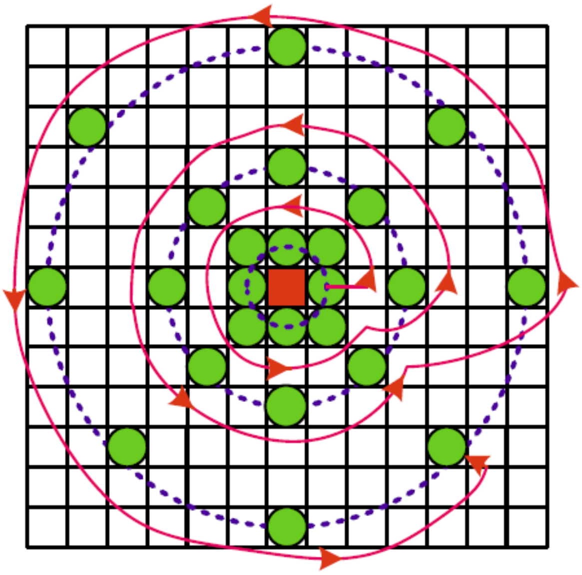

Figure 3.6: Integro-differential based constellation model (picture from [59]).

image pixels in a given eye image are first clustered based on the point-to-region distance and eight-neighbor connection. Iris region is selected from the clustered regions based on some heuristic rules. In order to localize pupillary and limbic boundaries, an integro-differential based constellation model is proposed, as depicted in Figure 3.6. The integro-differential operator is used to iteratively search for the local maximum from the sampling points as defined in the constellation model. In order to speed up the search, a "stop-at-once" strategy is used. In other words, if any of the sampling points returned an integro-differential score which is larger than the existing largest score (center point in the constellation model), the current iteration is stopped and a new search is started with the constellation model centered at the point which obtained the local maximum from the previous iteration. The eyelid localization, eyelash and shadow detection are performed based on the approaches as presented in [53].

3.2.2 Proença's Method

Proença proposed a neural-network (NN) based pixel-level classification approach to perform iris segmentation for the iris images acquired using either visible or NIR

(a) Classified sclera pixels

(b) Proportion of sclera features in east direction

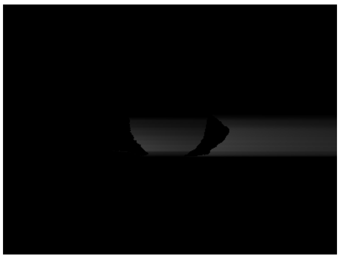

(c) Proportion of sclera features in west direction

(d) Proportion of sclera features in north direction

(e) Proportion of sclera features in south direction

Figure 3.7: Proportion of sclera features computed from classified sclera pixels.

illumination [60]. His proposed approach can be generally divided into three stages: (i) sclera classification stage, (ii) iris classification stage and (iii) boundary refinement stage. The sclera classification stage is aimed to perform binary classification of image pixels into either sclera or non-sclera category. To perform the classification, a 20-dimensional feature set as defined in Equation (3.1) is computed for every image pixel.

$$\left\{x, y, hue_{0,3,7}^{\mu,\sigma}(x,y), cb_{0,3,7}^{\mu,\sigma}(x,y), cr_{0,3,7}^{\mu,\sigma}(x,y)\right\}, \tag{3.1}$$

where (x, y) denotes the pixel coordinate; $hue()$, $cb()$ and $cr()$ respectively denote the square regions of the hue, blue-chroma and red-chroma color components centered at (x, y) with the radiuses specified as subscript, while the superscripts indicate the mean μ and standard deviation σ operations computed over the defined square regions. In the iris classification stage, an 18-dimensional feature set as defined in Equation (3.2) is computed for every pixel for binary classification.

$$\left\{x, y, sat_{0,3,7}^{\mu,\sigma}(x,y), cb_{0,3,7}^{\mu,\sigma}(x,y), p_{\leftarrow,\rightarrow,\uparrow,\downarrow}(x,y)\right\}, \tag{3.2}$$

where $sat()$ denote the square region of the saturation color component; $p_{\leftarrow,\rightarrow,\uparrow,\downarrow}(x,y)$ denotes the proportion of sclera features at the directions west (←), east (→), north (↑) and south (↓) at location (x,y), as shown in Figure 3.7. In order to provide adaptation for iris images acquired using NIR illumination, Proença employs the pixel intensity I with the modified feature sets $\left\{x, y, I_{0,3,5,7,9}^{\mu,\sigma}(x,y)\right\}$ and $\left\{x, y, I_{0,3,5,7,9}^{\mu,\sigma}(x,y), p_{\leftarrow,\rightarrow,\uparrow,\downarrow}(x,y)\right\}$ to perform sclera and iris classification, respectively. The boundary of the segmented iris region is further refined by using the polynomial regression technique.

3.2.3 Tan and Kumar's Method

Tan and Kumar developed a pixel-level classification approach similarly as to [60]. A six-dimensional feature set as defined in Equation (3.3) is used to perform classification of image pixels into either iris or non-iris category [65].

$$\{x_1, x_2, I(x_1, x_2), Z_{mn}^{l}(I, x_1, x_2)\}, \tag{3.3}$$

where (x_1, x_2) denotes the pixel coordinate; I is the image enhanced by using the retinex algorithm; Z_{mn} denotes the Zernike moments of order m and repetition n, computed over the square region with radiuses as indicated by $l = \{2,5,7\}$. They had provided the performance comparison between NN and SVM (support vector machine), which are two of the popular supervised machine learning models, to perform iris pixel classification. A set of post-processing operations such as boundary refinement, eyelid localization, reflection removal, eyelashes and shadow removal are also developed to further mitigate the possible classification errors from the classifier. Their proposed approach has shown to be effective to provide a unified segmentation framework to perform iris segmentation on iris images acquired using either visible or NIR illumination.

3.2.4 Other Methods

Approach [83] employed the well-known integro-differential operator for limbic and pupillary boundaries localization. The lower eyelid is modeled as circular arc and is localized using the similar segmentation operator with the additional supplementary intensity information. The upper eyelid and eyelashes are estimated based on a goodness of fit measure computed from the color (RGB) information. Almeida exploited information from different color spaces to perform the iris segmentation [84]. A number of seed points which serve as candidate pupil centers are placed in a gray level image with enhanced contrast. A greedy search based on gradient-based circular model is performed around the square region centered at each seed point to localize the pupillary boundary. Similarly, the limbic boundary is localized by performing the greedy search of circle in red channel image from a set of seed points. The localization of eyelids is performed based on a circular arc model in an image constructed from green and blue channels. Approach presented in [85] used an AdaBoost eye detector to search for the presence of the eye. A *k*-means clustering is applied to the gray level image of the detected eye region in order to coarsely cluster the image pixels into iris, sclera, skin, pupil and eyelashes categories. In order to localize the limbic boundary, a modified Hough transform is performed on the edge map computed from the *k*-means clustered image. While an integro-differential operator is used to localize the pupillary boundary and the upper eyelid. For lower eyelid localization, RANSAC (random sample consensus) algorithm is employed to estimate a set of candidate edge points for parabolic curve fitting. Jeong *et al.* employed two circular edge detectors to simultaneously localize the pupillary and limbic boundaries [86]. A parabolic Hough transform is employed to localize the eyelids from the candidate edge points computed from a set of masks. A set of convolution kernels and statistically established information of intensity distribution (*e.g.* mean, standard deviation) are used to detect the eyelashes. In approach [87], a modified circular Hough transform is used to localize both the pupillary and limbic boundaries from the estimated iris region. While a linear Hough transform is employed to localize the upper and lower eyelids. In approach [88], the pupillary and limbic boundaries are approximated using a technique similarly as to [43]. A thresholding method is applied to a Gabor filtered image to detect the separable eyelashes, while variance information is used to detect non-separable eyelashes and reflection. A Grow-cut based iris segmentation approach is presented in [89]. Detection of eyelids, eyelashes and reflection is achieved using the approaches as described in [65].

3.3 Feature Encoding and Matching

Table 3.2: Top three ranking from the NICE.II competition [90].

Ranking	**Username / Ref.**	**Affiliation**	**Country**	**Decidability Index (d')**
1	CASIA [64]	Chinese Academy of Sciences	China	2.5748
2	Betaeye [91]	Northeastern University	China	1.8213
3	UBI [92]	University of Beira Interior	Portugal	1.7786

Feature encoding for the iris images acquired distantly using visible illumination and under less constrained environments can be very challenging mostly due to the degradation in image quality and the image variations such as scale change, illumination change, defocus and translation. Currently, there are very limited efforts in the literature that attempt to address such limitations of feature encoding and matching algorithms on visible illumination images, with notable exceptions like those reported in the NICE.II (Noisy Iris Challenge Evaluation - Part II) competition [90], [93], [94]. The primary objective of the NICE.II competition is to provide evaluation on the robustness of iris encoding and matching methods for noisy images acquired under less constrained imaging conditions. Table 3.2 summarizes the top three iris encoding and matching algorithms from such competition.

3.3.1 Tan *et al.* Method

Tan *et al.* consider multiple features computed from the normalized iris and periocular[h] regions [64]. Boosting algorithm is used to select the most discriminative ordinal filters to encode the iris texture information [52], [95]. In addition, color distribution computed from multiple color spaces such as RGB, HSI and *lαβ* are employed to encode the iris color information. A set of the representative textons (texton dictionary) is constructed based on the *k*-means clustered dense SIFT (DSIFT) features [76] computed from the red, green and blue channels of the normalized training periocular regions. The constructed texton dictionary is used to classify the DSIFT features computed from the normalized periocular region of a query image. Such multiple features computed from the iris and periocular regions are combined using score level fusion technique to generate a single matching score which can be useful for decision making.

3.3.2 Wang *et al.* Method

Wang *et al.* use the 2D Gabor filters with multiple orientations to encode iris features from global and local regions of a normalized iris image [91]. Two distinct AdaBoost classifiers which can be more adaptive to two different segmentation scenarios: (i) pupillary boundary can be successfully localized and (ii) pupillary boundary cannot be segmented, are trained respectively in order to select the most discriminative Gabor features.

3.3.3 Santos and Hoyle's Method

In [92], a multiple features strategy by combining information from both iris and periocular regions are also exploited. Iris textures are encoded with 1D Gaussian

[h] Periocular or ocular is referred to the region around the eye (see CHAPTER 6).

wavelet, 2D dyadic wavelet, and 2D Gabor filters. For the first two encoding methods, the zero-crossings of the wavelet transforms are computed to obtain the iris codes. The iris codes of the 2D Gabor response can be obtained by comparing the sign of the filter output (see Section 2.2.1). To extract the periocular features, the approaches as detailed in [96] are employed. The LBP (local binary patterns), SIFT, and HoG (histogram of gradient) features are computed over the periocular region.

3.3.4 Other Methods

Shin *et al.* exploit both color and texture information for iris feature representations. The matching scores computed from the extracted features are combined based on weighted sum rule at score level [97]. Li *et al.* proposed a weighted co-occurrence phase histogram (WCPH) to characterize the local iris texture patterns. Bhattacharyya distance is employed to measure the similarity score between two WCPH features [98]. Marsico *et al.* exploit the LBP and discriminable texton representations for analyzing the local iris textures extracted from vertical and horizontal bands of the normalized iris image [99]. In [100], a sequential forward selection strategy is used to rank a set of 2D Gabor filters, and the most discriminative filters are employed to encode the iris features. Szewczyk *et al.* perform analysis on several wavelet transform approaches and conclude that the use of the reverse biorthogonal dyadic wavelet transform can achieve better recognition accuracy [101].

3.4 Summary

In this chapter, we provide review on recent iris segmentation, feature encoding and matching algorithms which are developed for distantly acquired eye images using visible imaging and under less constrained environments. Iris recognition using such noisy eye images is very challenging as the images are usually suffered from the degradation in the image quality and the image variations. Currently, there are very limited efforts in the literature which are dedicated for the eye images acquired at-a-distance and under less constrained environments using visible imaging, with the exceptions from those reported in NICE. I and NICE. II competitions. Therefore, extensive efforts in the development of iris recognition approaches which can perform more robustly and accurately on those noisy eye images are still required in order to make any inroad to the practical applications such as forensics and remote surveillance applications.

CHAPTER 4

Proposed Segmentation Approach for Iris Images Acquired under Less Constrained Environments

In this chapter, we present an effective iris segmentation solution to automatically extract the iris regions from the eye images which are acquired at-a-distance and under less imaging constrained environments using either NIR or visible illumination. The developed iris segmentation approach exploits random walker algorithm to efficiently estimate coarsely segmented iris images. These coarsely segmented iris images are post-processed using a sequence of operations which can effectively improve the segmentation accuracy. The robustness of the proposed iris segmentation approach is ascertained by providing comparison with several competing iris segmentation algorithms from the literature using three publicly available UBIRIS.v2, FRGC and CASIA.v4-distance databases. Our experimental results achieve improvement of 9.5%, 4.3% and 25.7% in the average segmentation accuracy, respectively for the UBIRIS.v2, FRGC and CASIA.v4-distance databases, as compared to the most competing approaches.

4.1 Methodology

Figure 4.1 shows the block diagram of the proposed iris segmentation approach which can be effective to segment iris images acquired at-a-distance and under less constrained environments, using either visible or NIR imaging. The face and eye detection module is aimed to provide detection for face or eye-pair region if face image is presented. As such, we employ an open source implementation of the

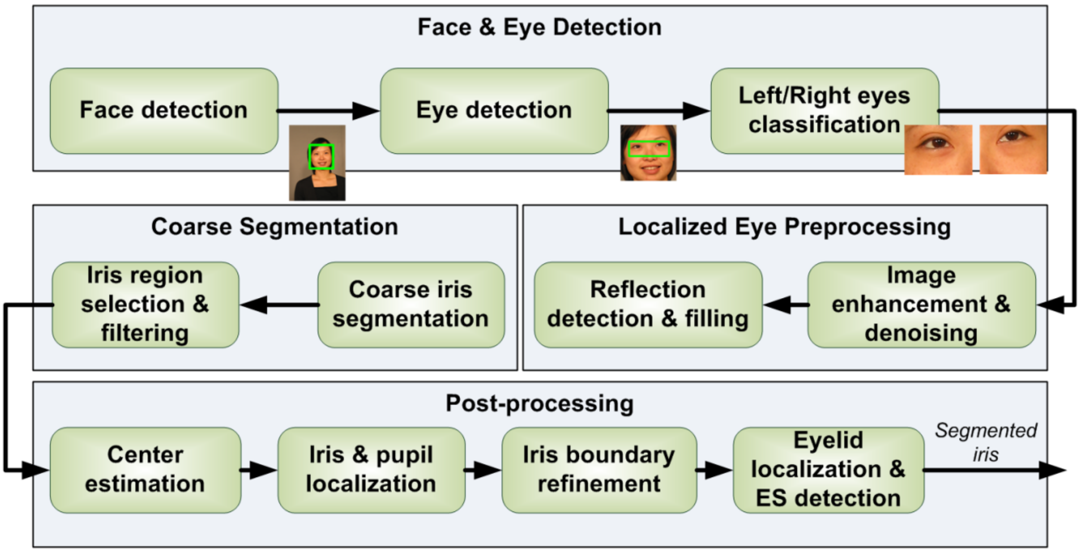

Figure 4.1: Block diagram of the proposed iris segmentation approach.

AdaBoost face and eye-pair detectors[i] to automatically detect the presence of face and eye-pair region [102], [103].

4.1.1 Preprocessing

Illumination variation is a common problem for imaging in real environment mainly due to the uncontrolled light source. Illumination variation not only poses difficulty in iris segmentation but also affects the recognition performance. Therefore, we adopt retinex algorithm as detailed in [104], [105], [106] to address such problem. The algorithm provides high dynamic range compression which has been shown to be effective in improving the overall image quality, especially for those iris images acquired under real imaging conditions. After that, Gaussian filter with standard deviation $\sigma = 1.5$ is applied to the image in order to suppress high frequency contents in the acquired images and help in segmentation. Also, the reflection removal technique reported in [65] is adopted in order to mitigate the influence from the source reflection in the subsequence iris segmentation operations

[i] Note that the objective of this thesis is not to further improve the performance of face and eye detection but intentionally to present a completely automated iris recognition framework for distantly acquired images which can operate under real/varying imaging conditions

4.1.2 Coarse Iris Segmentation

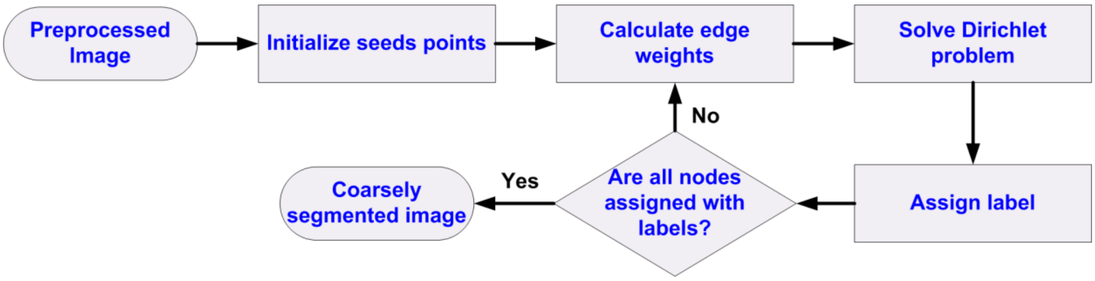

Figure 4.2: Flow chart of coarse segmentation using random walker based algorithm.

The objective of the coarse iris segmentation is to provide a simplistic model to "*classify*" each image pixel into either iris or non-iris category. Such model is intended to provide the classification performance as close to the reported classification method in [65], but with significantly reduced computational cost and complexity. Although it is expected that such simplistic model may not produce classification result as good as to the statistically trained model [65], such limitation is addressed with the post-processing operations (see Section 2.3-2.7) which provide robust solution to further refine the coarsely segmented iris images.

In this work, random walker (RW) algorithm [107] is exploited to provide solution for obtaining the coarsely segmented binary iris mask B_c. The RW algorithm is a general interactive segmentation algorithm and the general procedure is illustrated in Figure 3. In RW algorithm, images are modeled based on the graph theory [108], such that image pixels corresponding to the vertices $v \in \mathbb{V}$ of an undirected graph $\mathbb{G} = (\mathbb{V}, \mathbb{E})$. An edge $e_{mn} \in \mathbb{E} \subset \mathbb{V} \times \mathbb{V}$ is attributed by two vertices v_m and v_n. Each edge is associated with a weight (cost), $\omega_{mn}(\omega_{nm} = \omega_{mn})$, and is calculated by exploiting the gradient information, *i.e.*:

$$\omega_{mn} = \exp\left(-\rho \mathcal{G}_{mn}{}^2\right), \tag{4.1}$$

where $\mathcal{G}_{mn}{}^2$ is the normalized square difference between the intensities at nodes m and n,which can be calculated as follows:

$$\mathcal{G}_{mn}{}^2 = \frac{(g_m - g_n)^2}{\max\{o,p \in \mathbb{V}: e_{mn} \in \mathbb{E}\}\left(g_o - g_p\right)^2}. \tag{4.2}$$

The parameter ρ is the only free parameter which will affect the weighting function in Equation (4.1).

The RW-based iris segmentation requires initialization of seed points which forms a subset of the labeled nodes $\mathbb{V}_l$, and the remaining unlabeled nodes are denoted as $\mathbb{V}_u$, such that $\mathbb{V}_l \cup \mathbb{V}_u = \mathbb{V}$. The $\mathbb{V}_l$ contains the nodes labeled as either foreground (+1) or background (-1), which constitute two initial models to estimate labels for $\mathbb{V}_u$. In order to provide automated initialization of seed points, the following rules are employed:

$$v_{l_k} = \begin{cases} +1 & \text{if } g_k < mod(I) - \varphi_f \sigma(I) \\ -1 & \text{if } g_k > mod(I) - \varphi_b \sigma(I) \\ 0 & \text{Otherwise } \left(v_{l_k} \in \mathbb{V}_u\right), \end{cases} \tag{4.3}$$

where $mod(I)$ and $\sigma(I)$ are the mode and standard deviation of input image I (preprocessed). The weights were empirically computed during the training phase and were set as $\varphi_f = \{1.6,1.6,1.6\}$ and $\varphi_b = \{0.7,0.7,1.25\}$, respectively for the UBIRIS.v2, FRGC and CASIA.v4-distance databases. Then the relationship between the labeled and unlabeled nodes can be expressed using Dirichlet integral, as follows:

$$I_D(\tilde{x}_u) = \frac{1}{2}[\tilde{x}_l^T \quad \tilde{x}_u^T] \begin{bmatrix} L_l & B \\ B^T & L_u \end{bmatrix} \begin{bmatrix} \tilde{x}_l \\ \tilde{x}_u \end{bmatrix} = \frac{1}{2}(\tilde{x}_l^T L_l \tilde{x}_l + 2\tilde{x}_u^T B^T \tilde{x}_l + \tilde{x}_u^T L_u \tilde{x}_u), \tag{4.4}$$

where $\tilde{x}_l$ and $\tilde{x}_u$ denote the responses of the labeled and unlabeled nodes, respectively. L denotes the combinatorial Laplacian matrix defined as:

$$L_{mn} = \begin{cases} \sum_n \omega_{mn} & \text{if } m = n \\ -\omega_{mn} & \text{if} v_m \text{ and } v_n \text{ are adjacent nodes} \\ 0 & \text{otherwise.} \end{cases} \tag{4.5}$$

$$L_{u}\tilde{x}_{u} = -B^{T}\tilde{x}_{l}. \tag{4.6}$$

Nodes $\mathbb{V}_u$ are assigned with labels by solving the minimizer $\tilde{x}_u$ as in Equation (4.6) iteratively.

4.1.3 Initial Iris Center Estimation

The iris image and the corresponding binary iris mask B_c obtained from the coarse iris segmentation stage are exploited to provide information in estimating the initial iris center. In [65], the initial iris center was obtained by measuring the center of mass of the classified iris mask, under the assumption that the classified iris mask is proximate to the actual iris region. However, the B_c obtained from the coarse segmentation stage may not always produce the iris mask which is proximate to the actual iris region. By directly measuring the center of masses from those B_c can cause serious deviation of the initial iris center from the actual one, as illustrated in Figure 4.3(a)-(c). More importantly, such measurement error will be propagated to the subsequence operations and affect the overall iris segmentation performance. Therefore, it is essential to refine the B_c in order to mitigate the influence from the noisy artifact, or in particular, the eyelashes. As such, the mean of the heights μ_h from the masked region of B_c is employed to compute an adaptive threshold $\tau_h = 0.85 \times \mu_h$, which will be utilized to eliminate the column $h_g < \tau_h$, where h indicates the height of the column $g = 1, \dots, N$. The motivation to threshold the h_g is that the heights of the eyelashes regions beyond the iris region are observed to be shorter than the average height of the iris region, as shown from the third and the

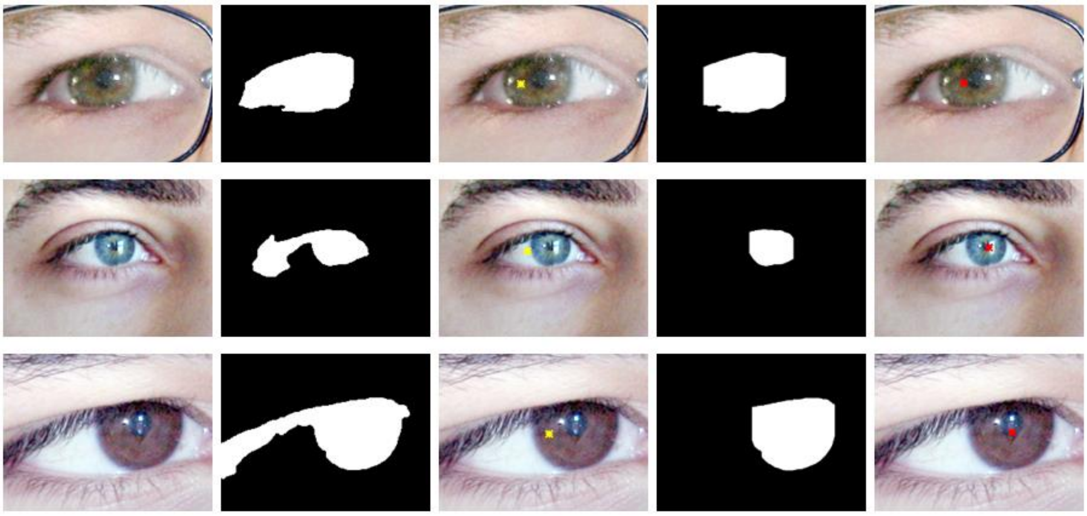

(a) (b) (c) (d) (e)

Figure 4.3: Initial center estimation. (a) Input enhanced image (color images are presented to provide better visualization), (b) Coarse segmented iris mask, (c) The estimated initial center (yellow mark) using (b), (d) Refined R_i, (e) The initial estimated iris center.

fourth sample images in Figure 4.3(d). The center of mass $C = (x_c, y_c)$ is then obtained from the refined binary mask $\tilde{B}_c$, as shown in Figure 4.3 (e).

The C is obtained exclusively from the $\tilde{B}_c$, which does not exploit any of the underlying image feature such as the intensity/color information. Therefore, such additional intensity information will be exploited to further improve the accuracy of the initial estimation of the iris center. Similar as in [65], the red channel plane I_r of the input color image I is employed throughout the experiment. A 2D median filter with respective size of {7×7, 3×3, 9×9} for UBIRIS.v2, FRGC and CASIA.v4-distance is applied to I_r in order to smoothen the intensity variations across image pixels. After that, the smoothened I_r is subject to gamma correction, which takes the following mathematical form

$$I_\gamma(x, y) = 255 \times \left(\frac{I_r(x, y)}{255}\right)^\gamma, \tag{4.7}$$

where I_γ is the gamma corrected of image I_r and (x, y) indicates the image coordinate. The γ is the parameter for gamma correction ($\gamma = \{0.8, 0.8, 1.0\}$ is empirically determined for

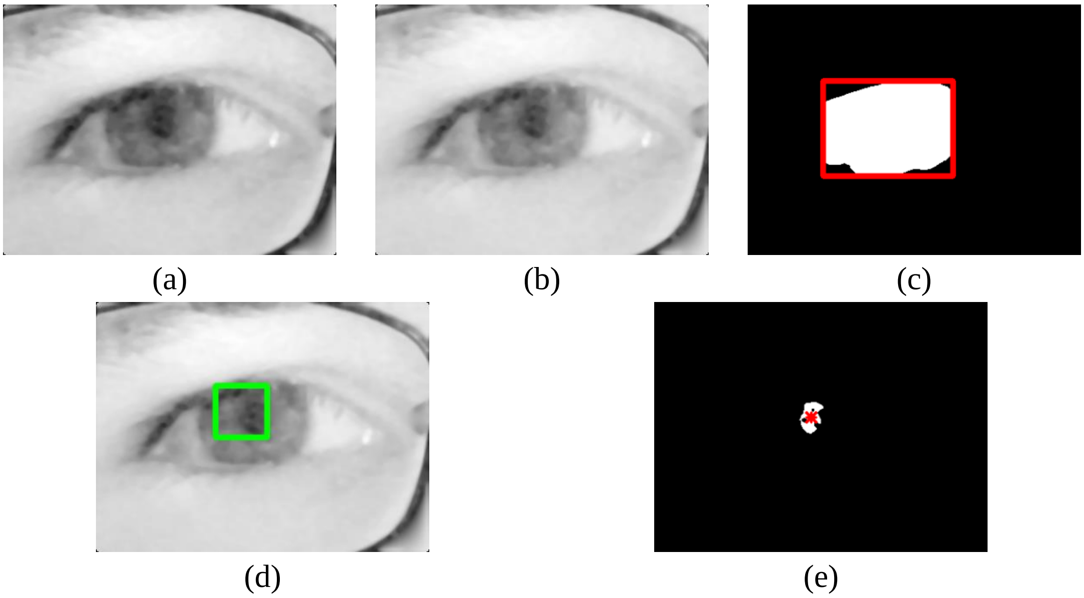

Figure 4.4: Initial center estimation using localized intensity information. (a) Extracted red channel plane, (b) Gamma corrected of image (a), with $\gamma = 0.8$, (c) The corresponding refined mask $\tilde{B}_c$ superimposed with a rectangle indicates the bounding region, (d) The region with the minimum average intensity, (e) Binary mask B_r and its center of mass. The estimated distance between C and $\tilde{C}$, $d(C, \tilde{C}) =$ 20.8945.

three respective databases, *i.e.*, UBIRIS.v2, FRGC and CASIA.v4-distance databases employed in the experiments). Given the refined mask $\tilde{B}_c$ and let's denotes $\boldsymbol{p_i} = (x_i, y_i)$ as the coarsely segmented iris pixels in $\tilde{B}_c$, average intensity of a rectangular region of size $H \times H$ centered at $\boldsymbol{p_i}$ is then computed, where $H = 0.55 \times h_B$ and h_B denotes one half of the height of the bounding region of $\tilde{B}_c$. The region R_i which produces the minimum average intensity will be employed for further processing and other regions are ignored. It is to be noted that such refinement step narrows down the search region for estimating the initial center. The average intensity at each R_i can be computed using the intermediate image representation, *i.e.* integral image (see [103]), which allows the fast computation of the regional mean with just single image scan. Figure 4.4 illustrates the described refinement process and it can be observed from Figure 4.4(d) that the search region for estimating initial center has been reduced. By applying a weighted thresholding method $\tau_\omega = \omega \times \tau_{Otsu}$ to the localized region, a binary mask B_r is then generated.

Table 4.1: Estimated Euclidean distance between iris and pupil centers.

	Min.	Max.	Mean
Distance between iris and pupil centers	1	11.1803	5.1202

The τ_{Otsu} denotes the threshold obtained by using Otsu's thresholding method; the ω denotes the weight and is set to 0.65 for all the employed databases in the experiments. The center of mass $\tilde{C} = (x_{\tilde{c}}, y_{\tilde{c}})$ of B_r is then computed, as illustrated in Figure 4.4(e).

Both of the acquired centers C and $\tilde{C}$ provide the information to estimate the initial center and it is expected that C and $\tilde{C}$ should be close to each other. As such, the Euclidean distance between C and $\tilde{C}$ is measured, *i.e.* $d(C, \tilde{C}) = \sqrt{(x_c - x_{\tilde{c}})^2 + (y_c - y_{\tilde{c}})^2}$. The distance metric is employed in helping to make decision how should the acquired centers C and $\tilde{C}$ to be utilized, with the following rule applied:

Rule 1:

If $d(C, \tilde{C})$ *> Threshold*

Both C *and* $\tilde{C}$ *are employed in the next operation.*

Else

Only C *is employed in the next operation.*

End

The distance threshold is set to 15 for all the employed databases based on the estimated distance from the training images, as summarized in Table 4.1. Note that all the presented parameters are empirically estimated from the training images (see Table 4.2), which is completely independent from the testing dataset.

4.1.4 Iris and Pupil Localization

The coarse segmented iris mask from the previous stage does not provide detailed information about limbic and pupillary boundaries, *i.e.*, the radius of pupil and iris.

By exploiting the information such as the coarse segmented iris mask B_c and the estimated center C from the previous stages, the limbic and pupillary boundaries will be approximated using circular model. Here, the approximation to the limbic boundary is used as an example to describe the developed approach. The pupillary boundary can be approximated in the similar manner[j]. The detailed steps of localizing the limbic boundary are as follows:

i. Firstly, an edge map E_m is obtained by applying Canny edge detector to the smoothed image I_γ. The iris radius is obtained by searching the maximum response A, as given as follows:

$$A = \underset{(x,y,r)}{\arg\max} \sum_{n=0,\ldots,N-1} E_m\left(p_n(x,y,r), q_n(x,y,r)\right), \tag{4.8}$$

$$\begin{gathered} x_c - \Delta o \leq x \leq x_c + \Delta o, \\ y_c - \Delta o \leq y \leq y_c + \Delta o, \\ \varphi_1 \min(h_B, w_B) \leq r \leq \varphi_2 \max(h_B, w_B) : \varphi_1 < \varphi_2, \end{gathered}$$

where x and y denote the coordinates within a bounding region calculated from the estimated center C and a predefined offset $\Delta o = \pm 15$. The r denotes the search radius which is calculated using the weighted half-height h_B and half-width w_B of the bounding region of $\tilde{B}_c$. The weights φ_1 and φ_2 are set to 0.7 (0.3) and 1.3 (0.8) for UBIRIS.v2 and FRGC (CASIA.v4-distance[k]) databases. The quantized N contour points $(\boldsymbol{p}, \boldsymbol{q})$ can be obtained using $p_n(x,y,r) = r\cos\frac{2\pi}{N}n + x$ and $q_n(x,y,r) = r\sin\frac{2\pi}{N}n + y$ respectively.

ii. In case of two estimated centers are obtained from Section 4.1.3, the step (i) is repeated for $\tilde{C}$, which yields $\tilde{A}$. Here, a simple heuristic is employed to check for the segmentation quality Q_s for both A and $\tilde{A}$, as defined as follows:

$$Q_s = \frac{A}{N} \tag{4.9}$$

[j] For NIR illumination based iris images, the order of localization is different. The pupillary boundary is localized first then only followed by the limbic boundary.

[k] The weights are for localizing pupillary boundary as the order of localization is different for the NIR images.

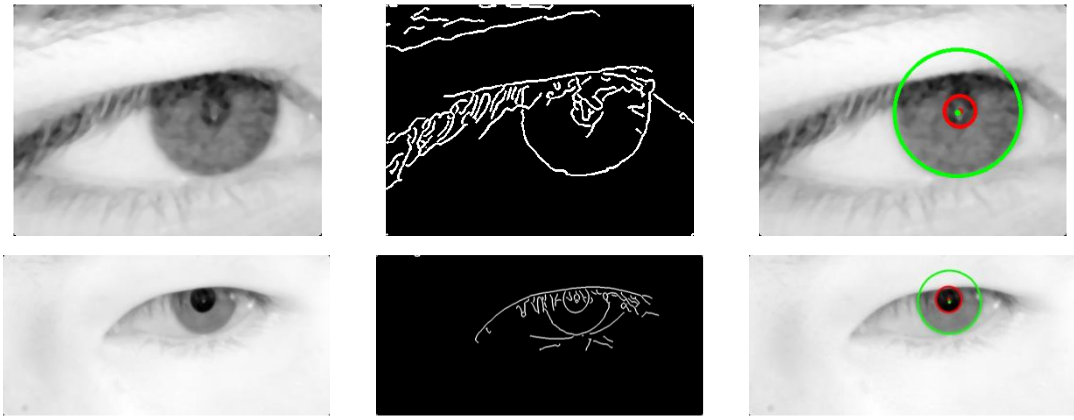

(a) (b) (c)

Figure 4.5: Limbic and pupillary boundaries localization. (a) Input smoothed image I_r, (b) Edgemap of (a), (c) Localized limbic and pupillary boundaries.

where N is the number of sampling points which acts as a normalization factor so that the $Q_s \in [0,1]$. The response which produces the highest score will be employed and the other one is discarded.

The parameters which describe the limbic boundary (x_{ir}, y_{ir}, r_{ir}) should be obtained and are employed to approximate the pupillary boundary $\left(x_{pu}, y_{pu}, r_{pu}\right)$. The (x_{ir}, y_{ir}) serves as the initial center and the predefined offset $\Delta o = \pm 10$. The search radius is calculated using r_{ir} with the weights φ_1 and φ_2 set to 0.2 and 0.6 for UBIRIS.v2 and FRGC databases. For localizing the limbic boundary of NIR illumination based iris images, we adopted different strategy for calculating the search radius, *i.e.* $\min(\varphi_1 r_{ir}, \varphi_1 \max(h_B, w_B)/2) \leq r \leq \varphi_1 \max(h_B, w_B)$, with $\varphi_1 = 1.3$. Figure 4.5 illustrates the described procedures for limbic and pupillary boundaries localization for both visible (first row) and NIR (second row) illumination based iris images.

4.1.5 Boundary Refinement

Iris segmentation for the iris images acquired under less constrained environments is highly challenging. The simple circular model as employed in Section 4.1.4 to approximate the limbic boundary is not sufficient to accommodate the inherent image variations for the images acquired under such challenging environments. Therefore, boundary refinement approach as developed in this section aims to address for such limitation to further refine the localized limbic boundary as obtained from Section 4.1.4. Statistical intensity information is exploited from two defined regions R_1 and R_2 in order to compute the adaptive threshold to remove non-iris pixels near to the limbic boundary. Such two regions can be obtained with respect to the localized iris (x_{ir}, y_{ir}, r_{ir}) and localized pupil $\left(x_{pu}, y_{pu}, r_{pu}\right)$ information. The region R_1 is defined as $R_1 = \left\{(x, y): x = r\cos\theta + x_{pu}, y = r\sin\theta + y_{pu}, r_{pu} < r \leq r_{pu} + \Delta o\right\}$. The offset Δo delimits the maximum size of the region to be considered, which is set to 20 for all the databases employed in the experiments. In order to mitigate the influence from the eyelid region which may potentially affect the performance, the lower part region of R_1 (half circular ring region) as illustrated in Figure 4.6(a), is considered. Mean μ_{R_1} and standard deviation σ_{R_1} are computed from such half-ring region to represent the statistical information of the iris region. An adaptive threshold is then calculated as $\tau_a = \mu_{R_1} + \beta\sigma_{R_1} : \beta \in \mathbb{R}, \beta > 0$, with the parameter β set to 2 for all the databases employed in the experiments. The region R_2 can be obtained similarly as to R_1, with the $r_{ir} - \Delta o < r \leq r_{ir} + \Delta o$, as illustrated in Figure 4.6(b). The computed adaptive threshold is then applied to the I_γ, *i.e.* $I_\gamma > \tau_a$, and the pixels belong to R_2 are retained. The thresholded pixels can be considered as the outliers whose intensities are deviated to a certain degree from the statistical information of R_1. In order to improve the robustness of the algorithm, an additional constraint is imposed which only the connected pixels to the limbic boundary are retained. Note that our method is different from [59] which they considered the statistical information from two consecutive annular rings near the limbic boundary. The information near to the limbic boundary is observed to be unstable due to the poorly localized limbic boundary. As such, the developed approach exploits the statistical information from the half-ring region (R_1) near to the pupillary boundary for computing the adaptive threshold to refine limbic boundary. The half-ring region is considered to be more stable as it is less likely to be influenced from the eyelashes and eyelid region.

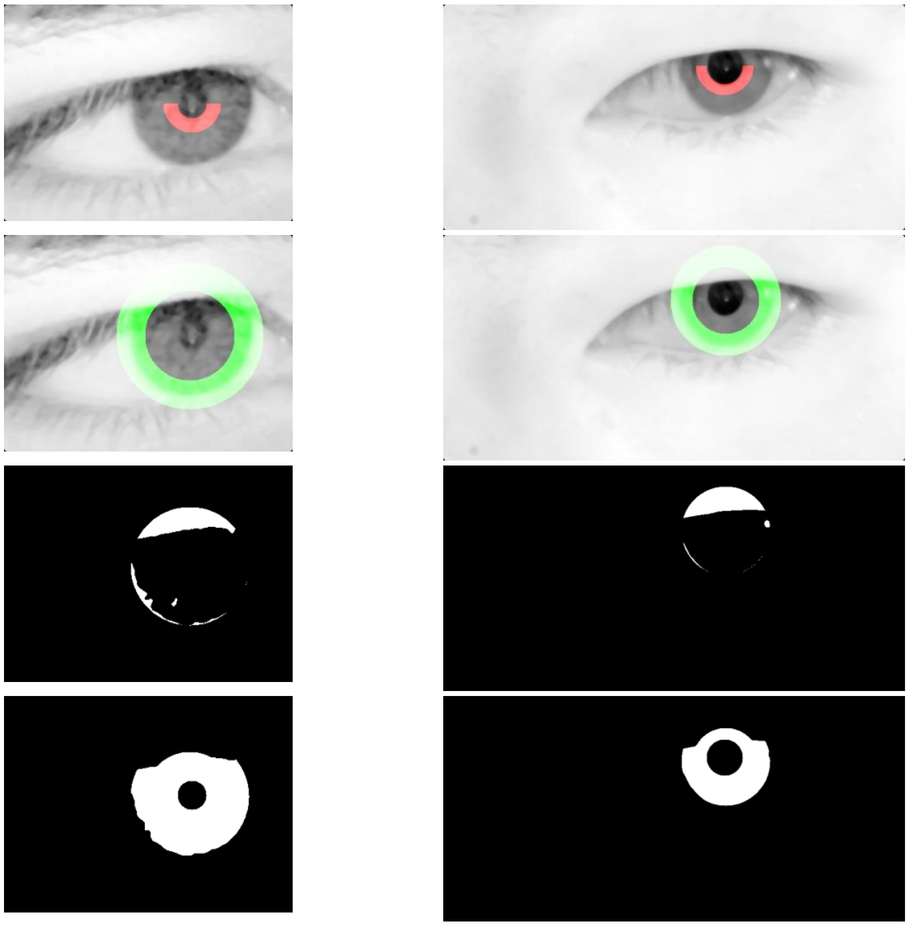

Figure 4.6: Boundary refinement. (a) Half-ring region R_1, (b) Region R_2, (c) Thresholded region, (d) Refined limbic boundary mask.

Figure 4.6 presents two sample results of the proposed boundary refinement method obtained from two of the employed databases, *i.e.*, UBIRIS.v2 (first column) and CASIA.v4-distance (second column).

4.1.6 Eyelid Localization with Adaptive Eyelid Models

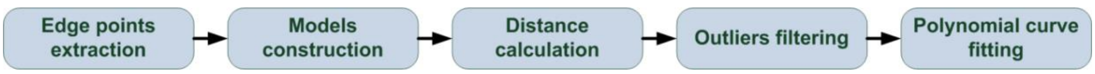

Figure 4.7: Eyelid localization steps.

Figure 4.7 shows the procedure of the developed adaptive eyelid location approach. The localized limbic information $R_{ir} = (x_{ir}, y_{ir}, r_{ir})$ is employed to define the upper and lower eyelid regions. The upper eyelid region can be computed as follows:

(a) Input image

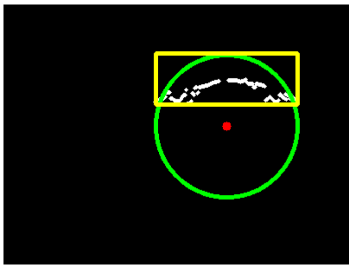

(b) Extracted edge points for upper eyelid from the delimited area

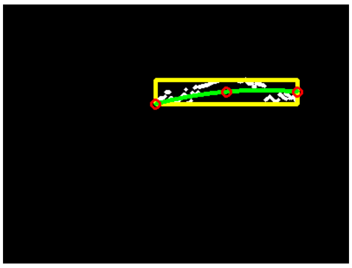

(c) Constructed upper eyelid model $M_{/}$ ($d_1 =$ 115.95),

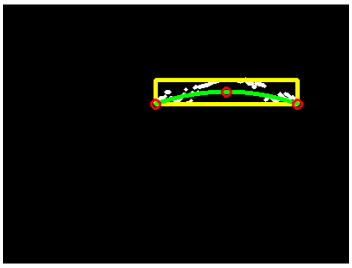

(d) Constructed upper eyelid model $M_{\wedge}$ (d_1 =105.85),

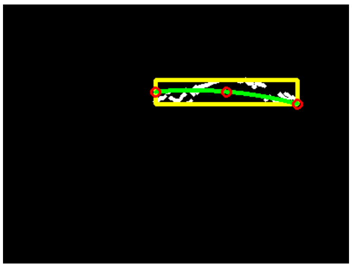

(e) Constructed upper eyelid model $M_{\backslash}$ ($d_1 =$ 128.94)

Figure 4.8: Adaptive eyelid models construction. Note that the edge points shown in the figures were enhanced for better visualization. (Note (c)-(e): Control points C_{M_l} are denoted using red 'o', bounding region is shown using yellow box and the constructed model is shown as green curve).

$$R_{upper} = \{x, y: x_{ir} - r_{ir} \le x \le x_{ir} + r_{ir}, y_{ir} - r_{ir} \le y \le y_{ir} - 0.3 \times r_{ir}\} \qquad (4.10)$$

The edge points $\boldsymbol{p}_{k=1,\dots,K} \in (R_{upper} \cap R_{ir})$ within the intersection region of R_{upper} and R_{ir} (see Figure 4.8(b)) are extracted as the candidate points for the construction of the eyelid models. Three eyelid models $M_{l=\{/,\wedge,\backslash\}}$ which represent the general eyelid shapes are adaptively constructed by exploiting the information of the bounding region of $\boldsymbol{p}_k$. Each of the model requires three control points which can be obtained from the bounding region of $\boldsymbol{p}_k$, as defined as follows: $C_{M_{/}} = \{(x_{min}, y_{max}), (x_c, y_c), (x_{max}, y_c)\}$, $C_{M_{\wedge}} = \{(x_{min}, y_{max}), (x_c, y_c), (x_{max}, y_{max})\}$, and $C_{M_{\backslash}} = \{(x_{min}, y_c), (x_c, y_c), (x_{max}, y_{max})\}$. The x_{min}, y_{min} (x_{max}, y_{max}) denote the minimum (maximum) *x*- and *y*-coordinate of the bounding region while x_c, y_c denote the middle point of the bounding region. The three eyelid models are then constructed by applying a second degree polynomial interpolation to the calculated control

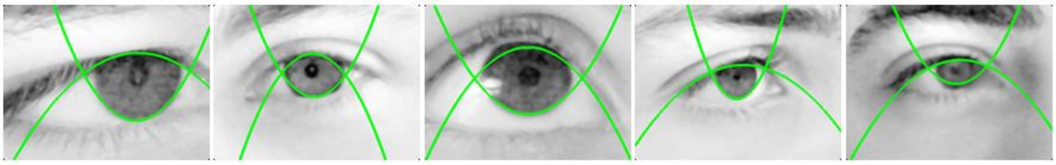

Figure 4.9: Sample eyelid localization results obtained using the adaptive eyelid model.

points C_{M_l}, as illustrated in Figure 4.8(c)-(e). In order to measure the best representative eyelid model among M_l, $L1$ distance d_1 between $\boldsymbol{p}_k$ and $\boldsymbol{p}_{M_l}$ is firstly calculated. The model which produces the minimum d_1 is considered as the best representative eyelid model and is employed as a reference model to eliminate outlier edge points.

Let's denote $\mu_{\widetilde{d_{1k}}}$ and $\sigma_{\widetilde{d_{1k}}}$ respectively as the mean and standard deviation of the distance $\widetilde{d_{1k}} = |\boldsymbol{p}_k - \boldsymbol{p}_{M_{lk}}|$ between the nominated eyelid model and the $\boldsymbol{p}_k$. Outlier edge points can be detected by performing the following statistical test:

$$\epsilon_k = \frac{\left(\widetilde{d_{1k}} - \mu_{\widetilde{d_{1k}}}\right)^2}{\sigma_{\widetilde{d_{1k}}}{}^2}. \tag{4.11}$$

The edge point $\boldsymbol{p}_k$ whose $\epsilon_k > 3$ is considered as the outlier point and is excluded for the subsequent operation. A second degree polynomial curve is fitted to the remaining candidate edge points in order to eliminate the non-iris region (upper/lower eyelid region). Figure 4.9 presents some sample results obtained from the developed eyelid localization technique. Localization of the lower eyelid region can be performed similarly as to the upper eyelid region. The proposed eyelid localization using adaptive eyelid models is inspired by the work in [53] which three representative eyelid models were trained for each upper and lower eyelid to eliminate the outlier points. One of the advantages of the proposed localization method is that it requires no prior training for the eyelid models while providing the similar functionality as in [53] to regulate the extracted edge points. The eyelid models are adaptively constructed by exploiting the localized information from each segmented iris and therefore provide superior localization capability than the globally trained models.

4.1.7 Eyelashes and Shadow Masking

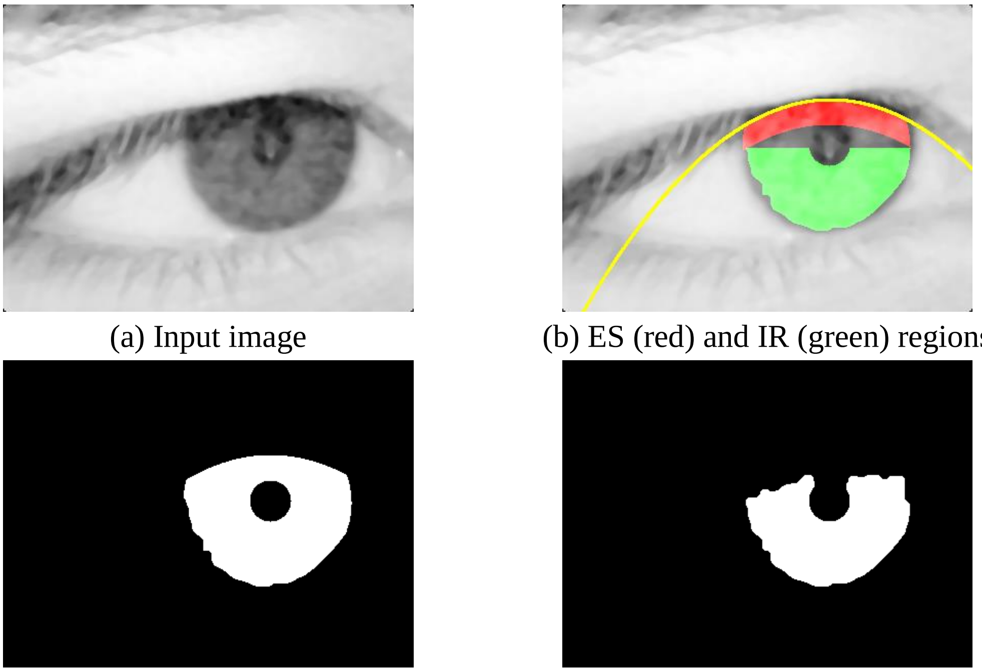

(a) Input image (b) ES (red) and IR (green) regions

(c) Iris masks before ES masking (d) Iris masks after ES masking

Figure 4.10: Eyelashes and shadow masking.

Eyelashes and shadow (ES) are one of the commonly observed noisy artifacts which occlude portion of iris region. The proposed ES masking method is similarly as to [65] by exploiting statistical information of the localized iris region to detect those noisy pixels. Firstly, the localized iris region is virtually divided into two regions namely ES region and IR region. ES region is defined as the region calculated from the localized upper eyelid to a distance $d = 0.3 \times r_{ir}$ while IR region is defined as the lower half annular region of the localized iris, as illustrated in Figure 4.10(b). Mean $\mu(\text{IR})$ and standard deviation $\sigma(\text{IR})$ of the IR region which describe the intensity distribution of the localized iris region are calculated. Such information is then employed to calculate two adaptive thresholds: $\tau_{low} = \mu(\text{IR}) - \delta_1\sigma(\text{IR})$ and $\tau_{high} = \mu(\text{IR}) + \delta_2\sigma(\text{IR})$, with the weights set to $\delta_1 = 3.5$ and $\delta_2 = 2.5$. The computed thresholds are employed to detect noisy pixels within ES region whose intensity $I < \tau_{low}$ or $I > \tau_{high}$. In addition, the τ_{high} serves as the complementary to the Section 4.1.6 to further eliminate eyelid pixels which may not be successfully removed in the earlier operation. Figure 4.10 illustrates the described ES masking method and it can be observed that the proposed method was effectively eliminated outlier pixels within the ES region

4.2 Experiments and Results

4.2.1 Databases and Evaluation Protocol

Table 4.2: Overview of the three employed databases.

	UBIRIS.v2	**FRGC**	**CASIA.v4-distance**
Operating illumination	visible	visible	NIR
Acquisition distance (meter)	4 – 8	N/A	≥ 3
Original image size	400 × 300	1200 × 1600	2352 × 1728
No. of training images / subjects	96 / 19	40 / 13	79 / 10
No. of test images / subject	904 / 152	500 / 150	502 / 67

Three publicly available databases namely: (i) UBIRIS.v2 [40], [90], (ii) FRGC [109], [10], and (iii) CASIA.v4-distance [110] were employed to evaluate the performance of the proposed segmentation method. The images from the first two databases were distantly acquired using visible imaging while the images from the third database were acquired using NIR imaging. Table 4.2 provides summarized information about the employed databases for the conducted experiments. It is worth noting that all the employed training images were independent from the test images.

- **UBIRIS.v2**: The full database consists of a total of 11102 images from 261 subjects. The images were acquired under less constrained imaging conditions with subject at-a-distance and on the move. The standoff distance (distance between subject and the camera) range between 4 and 8 meters. As similarly to [65], only subset of the images was employed in the experiment. The subset consists of 1000 images from 171 subjects. The eye images of the first 19 subjects were employed as training images for parameters selection and the rest of 904 images were employed as test images.

- **FRGC**: The images from the high resolution still images category were considered in our experiments. As similarly to [65], only subset of images was employed. The subset images were selected from the session 2002-269 to 2002-317 of Fall 2002. We employed the same procedure as reported in [65] for automatically localizing eye regions from these images.
- **CASIA.v4-distance**: The full database consists of a total of 2567 images from 142 subjects. The images were acquired using NIR imaging with the subjects 3 meters away from the camera. Images from the first 10 subjects were employed as training images for parameters selection. While the first left eye images from the subjects 11 – 77 were employed as test images to evaluate the segmentation performance.

In order to ascertain the performance of the proposed segmentation approach, we employ the identical protocol as adopted in the NICE.I competition [82]. The average segmentation error $\overline{E_1}$ is defined as follows:

$$\overline{E_1} = \frac{1}{N \times c \times r} \sum_{c\prime \in c} \sum_{r\prime \in r} O(c', r') \otimes C(c', r'), \tag{4.12}$$

where O and C correspond to the ground truth and segmented iris masks respectively; c and r denote the total numbers of columns and rows of the image; N is the total number of images. The XOR operator '$\otimes$' serves to evaluate the disagreeing pixels between O and C.

4.2.2 Performance Comparison

The proposed iris segmentation method reported average segmentation errors of 1.72%, 1.76% and 0.81% on UBIRIS.v2, FRGC and CASIA.v4-distance databases, respectively. The improvement over the method reported in [65] was respectively 9.5%, 4.3% and 25.7% on these three databases. We have also provided comparison

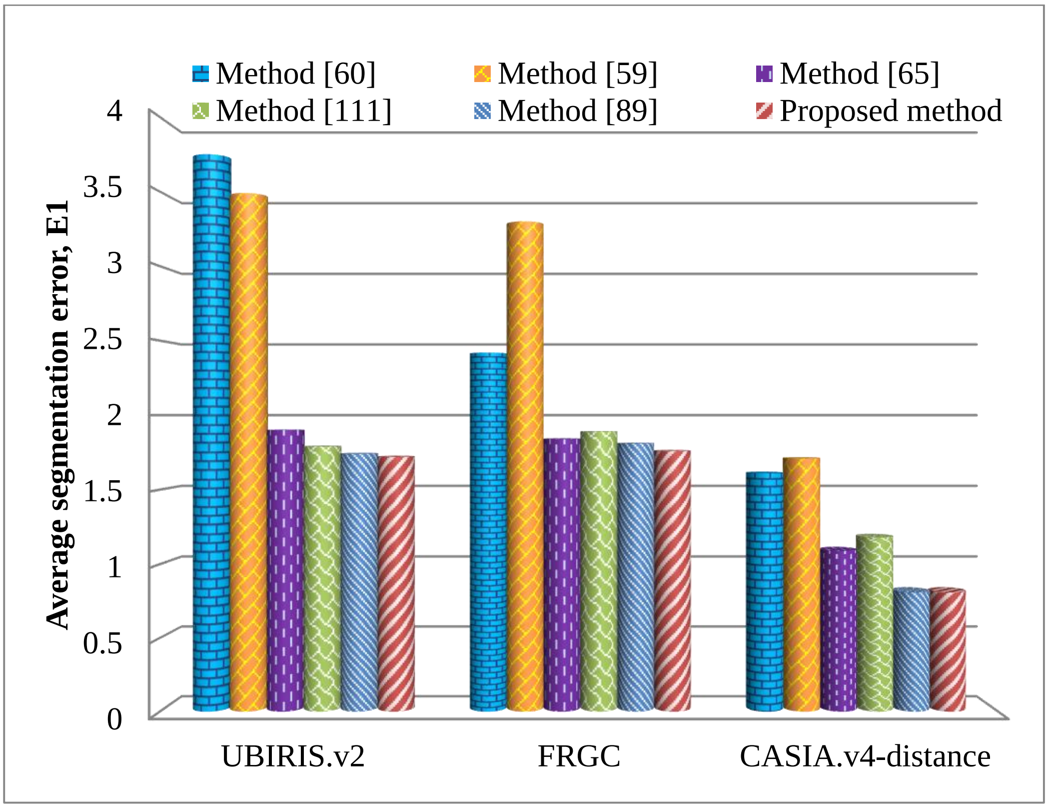

(a) Average segmentation errors of different segmentation methods

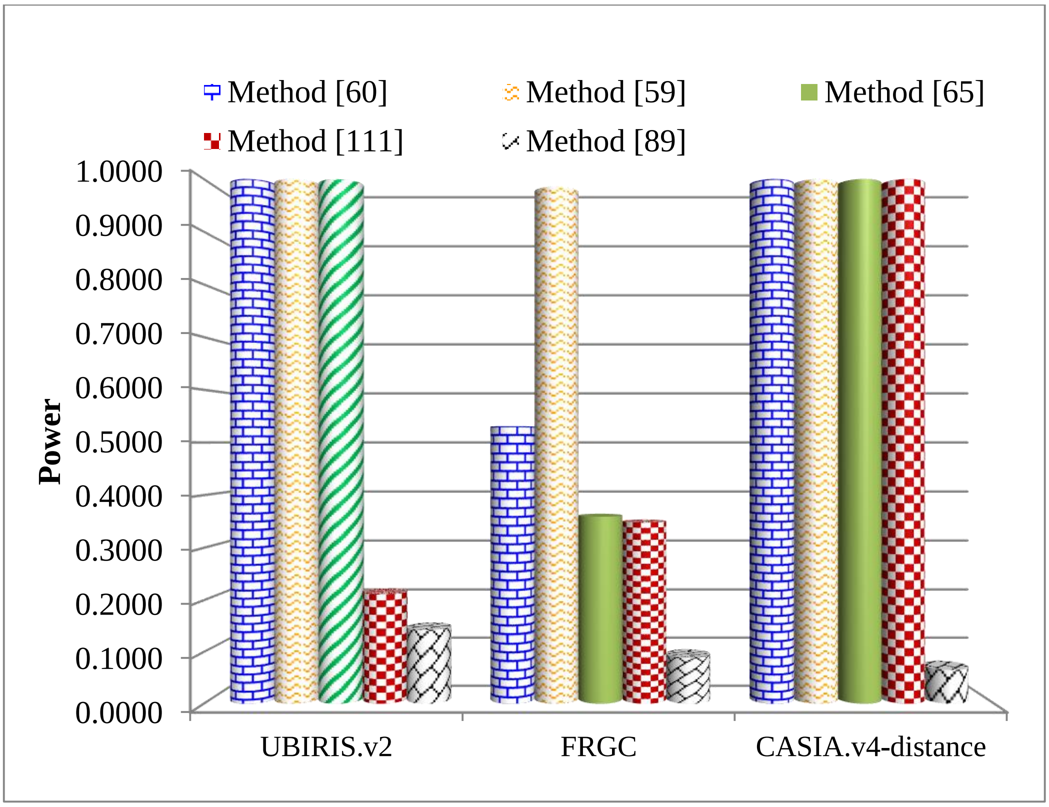

(b) Statistically significant differences of different segmentation approaches

Figure 4.11: Segmentation performance.

against other competing iris segmentation methods [59], [60], [65], [89], [111] as shown in Figure 4.11. This figure also illustrates statistical significance of the performance improvement over respective state-of-art approaches (*p*-value at significance level of $\alpha = 0.05$ using independent two-sample test technique [112]). It can be observed that the proposed segmentation method outperforms the other segmentation approaches reported in the literature [59], [60], [65], [89], [111] on the three employed databases. It is worth noting that the approaches [89], [111] employed the post-processing operations as developed in the Sections 4.1.3 – 4.1.7 to further refine the coarsely segmented iris images, and thus reported similar average segmentation errors. Therefore, the robustness of the developed post-processing operations is further ascertained from the competing segmentation performance obtained from the approaches [89], [111]. Figure 4.12 provides several sample results from the three employed databases as obtained by the proposed segmentation method. The proposed segmentation technique not only achieved better segmentation accuracy but also has the advantage in time efficiency. Table 4.3 summarizes the average execution time for computation of image features in the iris segmentation stage. All the experiments were conducted in Matlab environment and executed on Intel 2.93 GHz processor with 4 GB RAM. As can be observed from Table 4.3, the proposed segmentation technique significantly reduced the computational complexity in performing the iris segmentation. In [65], localized Zernike features are computed for every single pixel, which may explains the reason why significant amount of time is required.

Table 4.3: Average execution time.

	Average Execution Time (second)		***Improvement (%)***
	Method [65]	**Proposed Method**	
UBIRIS.v2	136.3	0.75	99.4
FRGC	51.1	0.39	99.2
CASIA.v4-distance	368.2	1.53	99.6

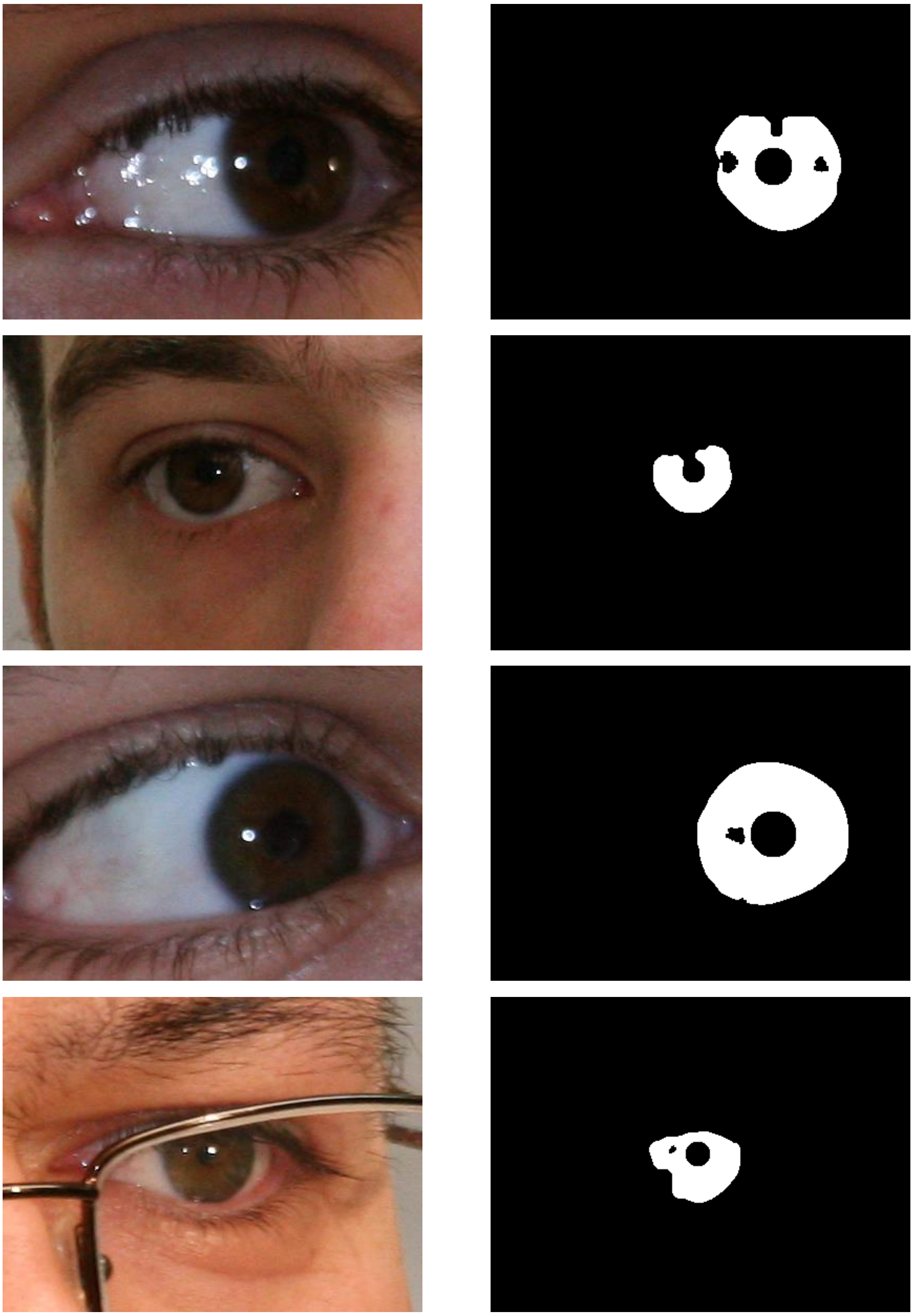

(a) Sample results from UBIRIS.v2 database (IDs: C102_S2_I14, C107_S1_I2, C109_S2_I14, C518_S1_I7)

(b) Sample results from FRGC database (IDs: 04243d88, 04265d84, 04302d15)

(c) Sample results from CASIA.v4-distance database (IDs: S4078D01, S4088D02, S4100D02)

Figure 4.12: Sample segmentation results.

4.3 Summary

In this chapter, a promising iris segmentation approach to automatically extract the iris regions from the distantly acquired eye images under less constrained environments is presented. The developed iris segmentation approach is computationally attractive (Table 4.3) as compared to the previously proposed approaches especially for *visible illumination based databases*. However, further efforts are still required to improve the efficiency of the iris segmentation algorithm in order to make it feasible for any possible online deployment in applications like remote surveillance. The experimental results obtained from the three publicly available at-a-distance databases: UBIRIS.v2, FRGC and CASIA.v4-distance, clearly demonstrate the superior performance of the proposed segmentation technique, which suggest average improvements of 9.5%, 4.3% and 25.7% in the segmentation accuracy as compared to the approach [65] on the three employed databases, respectively.

CHAPTER 5

Proposed Feature Encoding and Matching Approaches for Iris Images Acquired under Less Constrained Environments

Accurate iris recognition from the distantly acquired face or eye images requires development of effective strategies which can account for significant variations in the segmented iris image quality. Such variations can be highly correlated with the consistency of encoded iris features and the knowledge that such fragile bits can be exploited to improve matching accuracy. A non-linear approach to simultaneously account for both local consistency of iris bit and also the overall quality of the weight map is proposed. Our approach therefore more effectively penalizes the fragile bits while simultaneously rewarding more consistent bits. In order to achieve more stable characterization of local iris features, a Zernike moment-based phase encoding of iris features is proposed. Such Zernike moments-based phase features are computed from the partially overlapping regions to more effectively accommodate local pixel region variations in the normalized iris images. A joint strategy is adopted to simultaneously extract and combine both the global and localized iris features. The superiority of the proposed iris matching strategy is ascertained by providing comparison with several state-of-the-art iris matching algorithms on three publicly available databases: UBIRIS.v2, FRGC, CASIA.v4-distance. Our experimental results suggest that proposed strategy can achieve significant improvement in iris matching accuracy over those competing approaches in the literature, i.e., average improvement of 54.3%, 32.7% and 42.6% in equal error rates, respectively for UBIRIS.v2, FRGC, CASIA.v4-distance.

5.1 Methodology

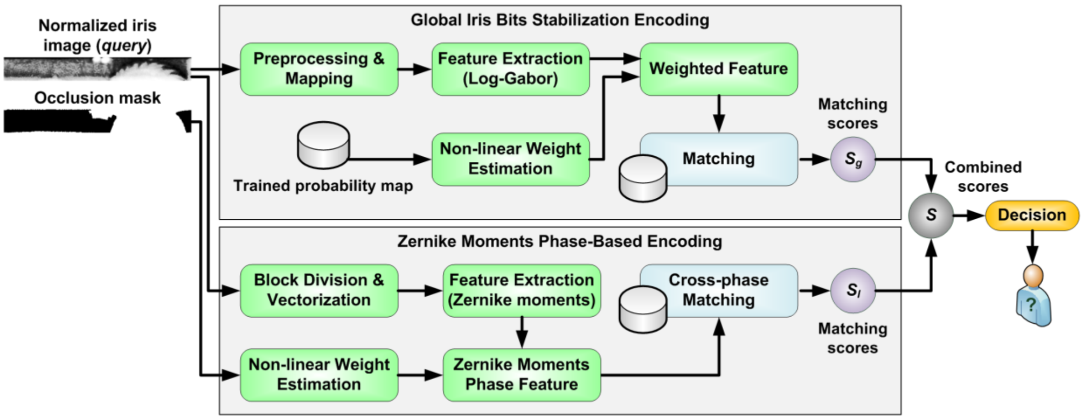

Figure 5.1: Block diagram of the proposed joint iris recognition strategy using global and localized (ZMs phase-based encoding) iris features encoding.

Figure 5.1 shows the block diagram of the proposed iris matching strategy which consists of a global iris bits stabilization encoding strategy (Section 5.1.1) and a localized Zernite Moments (ZMs) phase-based encoding strategy (Section 5.1.2). The global iris bits stabilization encoding strategy is motivated from the recent promising approaches in [48], [62], and exploits the weight maps in such manner that higher (lower) weights are assigned to the quantized iris bits which appear to be stable/consistent (fragile). Such weighting strategy is observed to be more effective especially for the noisy iris images acquired under less constrained environments by emphasizing (penalizing) the high (low) discriminative iris features. As such, a non-linear weighting approach based on the power law is proposed to adaptively weight the extracted global iris features. In spite of having better discriminative power over the conventional approaches [31], [43], [51], [65], [66], the global iris encoding strategy is still not adequate to accurately characterize the iris features extracted from the distantly acquired eye images under less constrained environments, which are generally have higher variations (*e.g.* scale change, illumination change, defocus and translation). In order to achieve more stable characterization of local iris features, we propose a new iris extraction scheme using phase encoding information of the ZMs. The ZMs have been shown to constitute robust image features which are less sensitive to noise, information redundancy, viewpoint change, partial occlusion, *etc*.

[113], [114], [115], [116], and therefore can be used as powerful descriptor to account for such variations in at-a-distance eye images. The localized ZMs features are computed from the partially overlapping image blocks extracted from the normalized iris image. The phase information in the computed ZMs encoded features from the image blocks is further exploited to construct a feature vector which represents the localized iris features. The advantages of employing such localized phase-based encoding strategy are two folds. Firstly, the local pixel variations can be better recovered from the localized iris region. Such localized phase-based encoding strategy can be more tolerant to feature distortion (due to nature of features) in local region pixels, and therefore can be exploited to complement the global encoding strategy in order to achieve more accurate recognition accuracy. Secondly, the phase encoding information of the ZMs has shown to offer more discriminative power than the magnitude information in local region pixels, as also in [116]. In order to mitigate the effect from the identified occluded iris pixels, a parameter γ is introduced to weight the computed ZMs features. This parameter γ is estimated from the occlusion mask which is automatically obtained during the iris segmentation stage. A joint strategy is employed to simultaneously combine both the extracted global and localized iris features. Such combined information can allow us to make better decisions and benefit from the outcome of matching performance using local texture matches which are more tolerant to variations/noise, and also the global iris texture matches which have its strength in less noisy iris region pixels.

5.1.1 Global Iris Feature Representation

A. Preprocessing for Normalized Iris Images

The accuracy of the iris segmentation and the effectiveness of the feature encoding are the essential core for any successfully iris recognition application. Most of the commonly observed noise sources such as occlusions from eyelashes, eyelid, hair, eyeglasses and specular reflections in the eye images can be usually identified and

(a) Normalized iris image (ID: S4011D00)

(b) Remapped normalized iris image

(c) smoothed version of (b).

Figure 5.2: Overlapping block strategy (Note that the actual image size of (b) and (c) are larger than the (a), and therefore they are resized to better utilization of space).

masked during the iris segmentation process. However, the eye images acquired at-a-distance and under less constrained environments are tend to be noisier not only due to the influences from the commonly observed noise sources but also from the imaging quality variations. Such phenomenon is even more noticeable from the eye images acquired using visible illumination imaging. In order to mitigate such influences, preprocessing is firstly applied to the normalized iris images by employing an overlapping block strategy, as given as follows:

$$f_{b,s}: \mathbb{R}^2 \rightarrow \mathbb{R}^2 \tag{5.1}$$

where f is a function to extract the image blocks of size $b \times b$ from the normalized iris image I, sliding at an interval of s pixels in both the horizontal and vertical directions. The interval s is defined as half of the block size, *i.e.* $s = b/2$ for all the employed databases in this paper. The remapped normalized iris images contain blocking artifacts as a result of the overlapping block operation. Such blocking artifacts are undesired as may introduce spurious frequency content during the iris feature extraction stage. In order to alleviate the effect from the blocking artifacts, a two-dimensional median filter of size $b \times b$ is applied to the remapped normalized iris images, as illustrated in Figure 5.2. The employed overlapping block strategy is observed to achieve improved recognition performance. There are two possible reasons to justify the advantages of the overlapping block strategy. Firstly, the information redundancy is achieved across the neighboring image blocks. Such redundant information can be exploited to better account for spatial variations in the normalized iris images, especially for those acquired under less constrained environments. Secondly, the smoothing operation by employing the median filter not only mitigates the effect from the blocking artifacts but also simultaneously suppresses the noise in each image block.

B. Iris Bits Stabilization

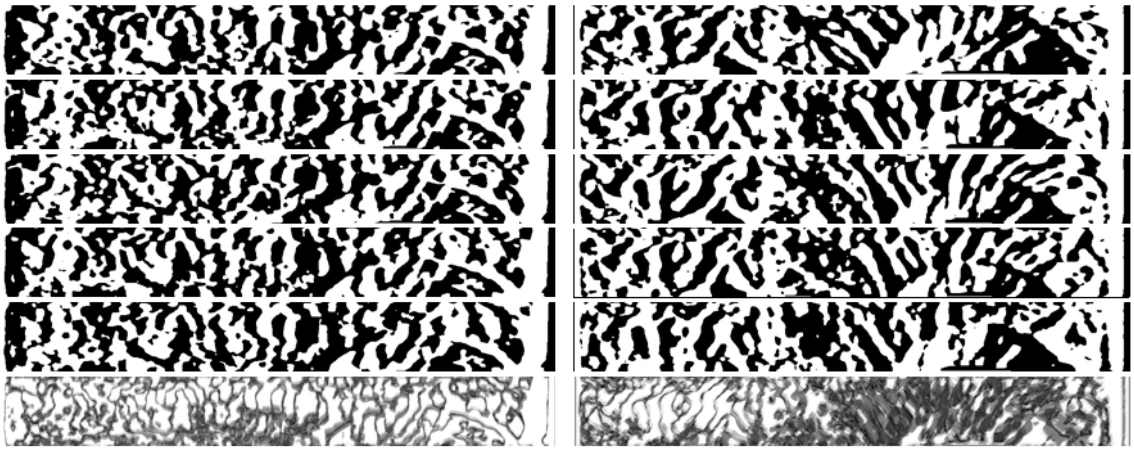

Figure 5.3: Examples of the trained probability map (last row) computed from five iris codes (first five rows) from CASIA.v4-distance database (Image IDs: {S4011D00, S4011D01, S4011D02, S4011D03, S4011D04}, {S4023D00, S4023D01, S4023D02, S4023D03, S4023D04}). Brighter pixel indicates the bit is more stable while darker pixel indicates otherwise.

The existence of the fragile bits has been observed and effectively used in [48] to improve the matching accuracy. Ref. [62] further extended this work based on the knowledge of fragile bits by weighting each bit to achieve improved recognition performance. The eye images acquired under less constrained environments are often degraded by noise, and the observation shows that the occurrence of noise is even more evident in the eye images acquired under visible illumination [60], [64], [65]. Therefore, the previous strategy as in [48], [62] can be further exploited to

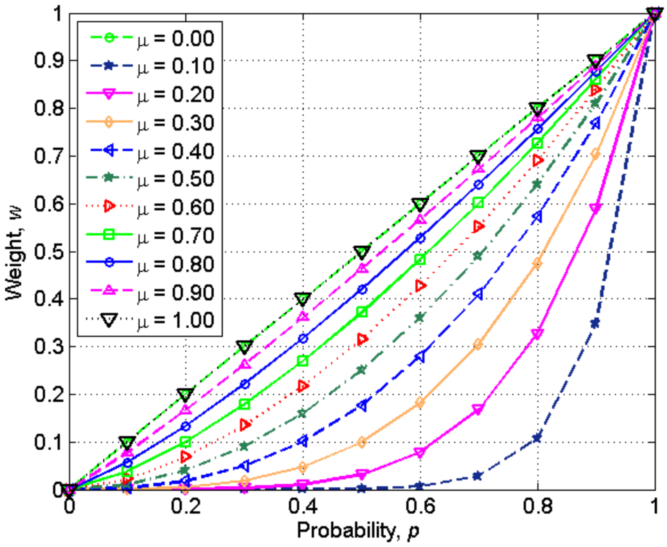

Figure 5.4: The influence of μ on the bit probability.

work on the noisy eye images which are acquired under less constrained environments. The fragile bits which are estimated from the training images can be considered as an outcome from the noise perturbation.

As such, we propose a nonlinear weighting strategy to quantify the consistency of each iris bit in the remapped normalized iris image. The iris bit which is more consistent will be assigned with higher weight (close to one) to emphasize its importance while the iris bit which is less consistent is assigned with a lower weight (close to zero). Given K preprocessed training normalized iris images $\{\hat{I}_i^j\}_{i=1}^K$ of j-th class, we first obtain the corresponding iris code representations $\boldsymbol{C}^j = \{C_i^j\}_{i=1}^K$. Next, the consistency of n-th bit can be estimated from the $\boldsymbol{C}^j$ by measuring the number of times that the n-th is fragile. Note that the $\boldsymbol{C}^j$ is aligned with respect to the minimum Hamming distance obtained from the circular bit shifting before the consistency of iris bits is estimated. Let θ_n denote the number of times that n-th bit is fragile. Then the consistency of n-th bit can be indicated based on a probability value, as defined as follows:

$$p_n^j = 1 - \frac{\theta_n}{K} \in [0, 1]. \tag{5.2}$$

Hence, a probability map $P^j = \{p_1^j, p_2^j, \dots, p_N^j\}$ can be obtained based on the knowledge of the fragile bits estimated from some iris codes $\boldsymbol{C}^j$. The P^j has the identical dimension as the iris code of N bits, with each p_n^j corresponding to the consistency of the *n*-th iris bit. Figure 5.3 shows two examples of the probability maps obtained from the five iris codes. It can be observed that the iris bits where are estimated to be more consistent have higher probability values (higher intensity values), while the iris bits which are less consistent are indicated by lower probability values (lower intensity values).

In order to more effectively emphasize (penalize) those bits which are highly consistent (inconsistent), a non-linear weighting strategy is introduced as follows:

$$w_n^j = \left(p_n^j\right)^{\alpha^j}, \tag{5.3}$$

$$\alpha^j = \begin{cases} \dfrac{|P_{max}|}{\mu^j} = \dfrac{1}{\mu^j} & \text{if } \mu^j > 0 \\ 1 & \text{if } \mu^j = 0 \end{cases} \tag{5.4}$$

where $\mu^j = {}^1\!/_N \sum_{n=1}^{N} p_n^j$; P_{max} indicates the maximum probability value of P. The α^j takes the similar form as crest factor (peak-to-average ratio) which is employed to indicate the overall quality of the P^j. Figure 5.4 illustrates the influence of the stability factor on the computed stability map P^j . The weighting function in Equations (5.3) and (5.4) exhibit several interesting properties which can be summarized as follows:

- The weighting function *preserves* the local consistency value for the highly consistent (inconsistent) bits, *i.e.* when $p_n^j = \{0,1\}$, regardless of the crest factor α^j. As such, the weights for those highly consistent (inconsistent) bits will not be affected by α^j.
- For $\mu^j = \{0, 1\}$, which are the two special cases when the crest factor at its extremum, the weight remains the same, i.e. $w_n^j = p_n^j$.

- For $K = 1$, the computed weight map $W^j = \{w_1^j, w_2^j, \dots, w_N^j\}$ is identical to the generated iris code C^j , such that the $w_n^j = \{0,1\}$. Therefore, the Equation (5.3) can be considered as the generalized representation for the conventional iris code representation.

The similarity between a query iris code C_{query} and reference gallery iris code $C_{gallery}^j$ of class j can be computed using a modified Hamming distance function as given below [62]:

$$HD^j = \frac{\|(C_{query} \oplus C_{gallery}^j) \times W^j\|}{\|W^j\|}. \tag{5.5}$$

5.1.2 Zernike Moments Phase-based Encoding

Zernike moments are well known to extract scale, rotation and translation invariance features and are employed in many image processing applications, including in iris segmentation [65], [117], image reconstruction [114], [115], *etc*. However, prior attempts *only* exploited the magnitude information of the ZMs in order to benefit from the rotation invariance property. The coarse phase information (iris code) as detailed in [31], [43] has been successfully employed to characterize the iris texture. Such an approach for iris matching has shown to achieve accurate iris matching for large-scale iris recognition applications but under constrained and NIR-based image acquisition. However, large image variations such as scale changes, illumination changes, geometric transformation, *etc*., are often encountered in case of the iris images acquired at-a-distance and under the less constrained environments, which further increase the difficulty in performing the iris encoding and matching for such noisy iris images. The ZMs have been shown to constitute robust image features which are tolerance to those commonly observed image variations in the remotely acquired iris images [113], [114], [115], [116]. As such, we develop a new iris encoding and matching strategy by exploiting the phase information of the ZMs extracted from the partially overlapping local iris region pixels. The motivation of using ZMs phase-only information to encode such localized iris texture information are as follows: (i) The phase information has been demonstrated to provide better discriminative power than the magnitude information, while retaining the scale invariant properties of the ZMs to accommodate inherent image variations from less constrained imaging [116]; (ii) the local pixel variations can be better recovered from the localized iris region rather than those accumulated globally from the phase difference in conventional iris encoding. Such phase encoding information of the ZMs from the local region pixels is expected to be more tolerant to the feature distortions than the global encoding scheme, and therefore can be used to complement the global iris features matching to achieve more accurate performance.

A. Zernike Moments

The Zernike moments with order β and repetition α constitute a set of orthogonal basis functions $\{V_{\beta\alpha}(\rho, \tilde{\theta})\}$ which are defined over a unit circle in the polar coordinates as follows [114], [116]:

$$V_{\beta\alpha}(\rho, \tilde{\theta}) = R_{\beta\alpha}(\rho) e^{j\alpha\tilde{\theta}} \tag{5.6}$$

$$R_{\beta\alpha}(\rho) = \sum_{k=0}^{p} (-1)^k \frac{(\beta - k)!}{k!\,(p-k)!\,(q-k)!} \rho^{\beta - 2k}, \tag{5.7}$$

where $p = (\beta - |\alpha|)/2$ and $q = (\beta + |\alpha|)/2$; β is a non-negative integer and α is an integer that satisfies the conditions: $|\alpha| \leq \beta$ and $\beta - |\alpha| = \text{even}$. ZMs for an image function $I(\rho, \tilde{\theta})$ can be obtained by projecting the $I(\rho, \tilde{\theta})$ onto $\{V_{\beta\alpha}(\rho, \tilde{\theta})\}$, as represented by:

$$Z_{\beta\alpha} = \frac{\beta + 1}{\pi} \int_0^{2\pi} \int_0^1 I(\rho, \tilde{\theta}) V_{\beta\alpha}^*(\rho, \tilde{\theta})\, \rho \; d\rho\, d\tilde{\theta}, \tag{5.8}$$

where $V_{\beta\alpha}^*$ denotes the complex conjugate of Equation (5.6).

B. Localized Iris Representation

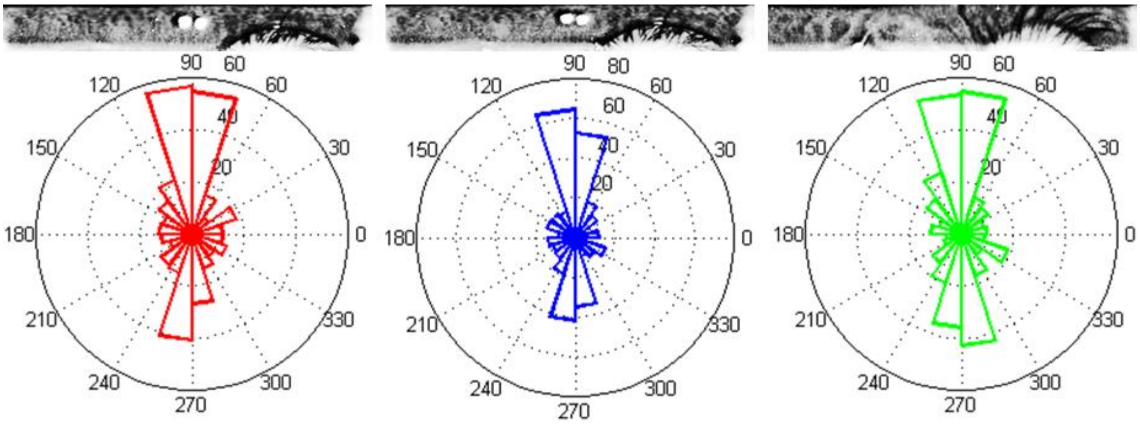

(a) S4011D00 (b) S4011D01 (c) S4023D01

Figure 5.5: Phase angle information for three Zernike features respectively computed from the normalized iris images from CASIA.v4-distance database. Features (a) and (b) are computed from the images of the same class. The varying angles represent the encoded iris features using the phase information of the ZMs. The similarity scores between (a) and (a), (a) and (b), and (a) and (c) are $s(a,a) = 0$, $s(a,b) = 16.624$ and $s(a,c) = 27.218$, respectively.

The localized ZMs features are computed from the image blocks B of size $\tilde{b} \times \tilde{b}$ extracted from the normalized iris image I, sliding at an interval of $\tilde{s}$ pixels in both the horizontal and vertical directions. The interval $\tilde{s}$ is defined as half of the block size, *i.e.* $\tilde{s} = \tilde{b}/2$ for all the employed databases in this paper. Let N_B denote the total number of extracted image blocks $\{B_i\}_{i=1}^{N_B}$. The ZMs from order one up to order β at repetition α are computed for each B_i, which form a feature vector $\boldsymbol{Z}$ as represented as follows:

$$\boldsymbol{Z} = \gamma \left[Z_{1\alpha}^{1}, Z_{2\alpha}^{1}, \dots, Z_{\beta\alpha}^{1} | \dots | Z_{1\alpha}^{N_B}, Z_{2\alpha}^{N_B}, \dots, Z_{\beta\alpha}^{N_B} \right]^T. \tag{5.9}$$

The parameter $\gamma \in [0,1]$ is introduced in Equation (5.9) which serves to mitigate the effect of the occlusion noise to the computed Zernike features. Such γ is defined and can be computed as follows:

$$\gamma = \frac{2\xi}{1+\xi^2} \tag{5.10}$$

$$\xi = 1 - \frac{O_{noise}}{W \times H}, \tag{5.11}$$

where O_{noise} denotes the total number of occluded iris pixels (white) which are identified from the automatically extracted $W \times H$ occlusion mask from the iris segmentation phase.

In order to measure the similarity s between two given feature vectors $\boldsymbol{Z}_{query}$ and $\boldsymbol{Z}^{j}_{gallery}$ of class j, we employ a phase distance function which can be described as follows:

$$s^j = \left\| \varphi\left(\frac{\boldsymbol{Z}_{query} \circ \boldsymbol{Z}^{*j}_{gallery}}{\left|\boldsymbol{Z}_{query} \circ \boldsymbol{Z}^{*j}_{gallery}\right|} \right) \right\|_2 = \|\varphi(R)\|_2 \tag{5.12}$$

$$\varphi(R) = \arctan\left(\frac{\mathrm{Imag}(R)}{\mathrm{Real}(R)}\right), \tag{5.13}$$

where $\mathrm{Real}(.)$ and $\mathrm{Imag}(.)$ respectively denote the real and imaginary parts of R; '$\circ$' denotes the entry-wise product; '$*$' denotes the complex conjugate. Higher similarity between phase angles of the ZMs will result in lower values of S (close to zero) while higher dissimilarity will result in higher values. It can be observed that the phase information computed from the iris images of the same subject, for example in Figure 5.5(a) and (b), are highly correlated.

5.2 Experiments and Results

In this section, we detail on the experiments and present results from the rigorous experimentation on three publicly available databases: UBIRIS.v2 [40], [90], FRGC [10], [109], and CASIA.v4-distance [110] to ascertain the performance from the proposed iris matching strategy. The three employed databases were *distantly* acquired (ranging from 3-8 meters) under less constrained environments using either *visible* or *NIR* imaging, and therefore appropriate for the research problem focused in this thesis. All the employed iris images in the conducted experiments use automated iris segmentation approach as described in CHAPTER 4, which has shown to be more accurate as it achieves superior segmentation accuracy on both the iris images acquired under visible and NIR illumination. In order to ascertain the performance of the proposed feature encoding and matching strategy, we employ the two most commonly used performance metrics in the iris biometrics literature, *i.e.*, Equal Error Rate (EER) and the decidability index (*d*'), as described in Section 1.1.2.

5.2.1 Databases and Evaluation Protocol

Table 5.1: Numbers of images and subjects of the employed databases[1].

Database	**UBIRIS.v2**	**FRGC**	**CASIA.v4-distance**
Illumination type	Visible	Visible	NIR
Number of images	863	1085	934
Number of subjects	151	149	128

All the experiments performed in this work use subsets of images from the three employed databases, as summarized in the Table 5.1. The segmented iris images from UBIRIS.v2, FRGC, and CASIA.v4-distance databases are respectively normalized to the sizes of 512×64, 256×32 and 512×64. The global iris features are extracted by employing 1D log-Gabor filter [49], and the parameters *wavelength* and *SigmanOnf* for the three employed databases are given in Table 5.2. Such parameters are obtained from a set of training images which are independent from the test images. For CASIA.v4-distance database, the images from the first 10 subjects are employed to train the log-Gabor parameters, while the first eight left eye images from the rest of the 128 subjects are employed for testing or performance evaluation. For UBIRIS.v2 database, a subset of 1000 images from 171 subjects as

[1] This table shows the effective numbers of images and subjects used in the experiments. Some images were excluded in the experiments due to the limitations of eye detector or iris segmentation algorithm.

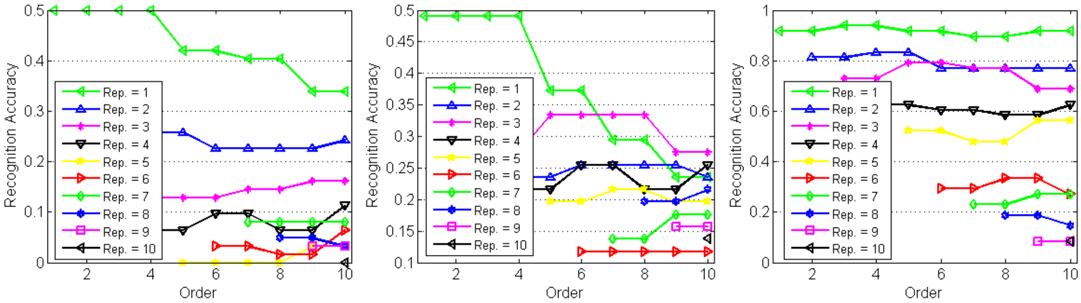

(a) UBIRIS.v2 (b) FRGC (c) CASIA.v4-distance

Figure 5.6: Parameters selection for Zernike-moments phase-based encoding on three employed databases with the corresponding window sizes {25, 17, 25}.

Table 5.2: Parameters employed by the proposed approach.

Parameter / Database	*Global Feature*		*Localized ZMs phase-based Feature*		
	Wavelength	SigmaOnf	Block size	Order	Repetition
UBIRIS.v2	59	0.32	25	1	1
FRGC	40	0.35	17	1	1
CASIA.v4-distance	20	0.25	25	3	1

released in [90] is employed in the experiments. The 96 images from the first 19 subjects are employed for selecting the log-Gabor parameters[m] while the rest of the segmented eye images are employed as independent test images for the performance evaluation. Similarly, a subset of high-resolution still images from the FRGC database is employed in the experiments. The eye images are selected from session 2002-269 to 2002-317 of Fall2002 and Spring2003 by using an open source eye detector provided in OpenCV [102], which comprise a total of 1085 images from 149 subjects. For the color images, we employ the luma-channel (Y) of the YCbCr after the color space conversion from the RGB color space. As for the performance evaluation, we further divide the remaining images into gallery dataset and test dataset. The gallery dataset is employed in training the weight maps as detailed in Section 5.1.1. In addition, subsets of the images from the gallery dataset of the employed databases are randomly chosen in order to determine the parameters for the localized Zernike moments representations as detailed in Section 5.1.2. In this

[m] We use same protocol as in previous work in [65] and [66].

paper, we employ the *first five images* (or at most[n][o]) as the gallery dataset while the remaining images as the test dataset. The ZMs features with parameters (n, m) range from $(1, 1)$ and to $(10, 10)$ are computed on the image blocks of various sizes. Figure 5.6 shows such parameters estimation computed from the training images of the three employed databases. The choices of the parameters are quite consistent with several reported works [113], [114], [116], as higher-order moments are more sensitive to image noise. The decline in the recognition accuracy can be observed on the noisy datasets from the UBIRIS.v2 and FRGC databases when higher-order moments are employed in computation of ZMs features but remain stable on the CASIA.v4-distance dataset (with relatively less influence from the noise on the NIR iris dataset).

5.2.2 Comparison Between Real-valued and Quantized ZM Phase-based Features

In this section, we provide comparison between the real-valued (ZMs) and the binary quantization (ZMs_{bin}) of the ZMs phase-based features. Figure 5.8 and Figure 5.9 respectively show the receiver operating characteristic and cumulative match characteristic curves computed from the three employed databases. It can be observed that the real-valued ZMs phase-based features generally achieve better recognition accuracy as compared to the quantized features, especially on the visible illumination based iris dataset.

[n] The number of images is varying for each distinct subject for UBIRIS.v2 and FRGC databases as some poor segmented/quality images were filtered out by the completely automated segmentation algorithm [66].
[o] The total numbers of generated genuine/imposter scores are 276/41400, 287/42476 and 337/42462 from UBIRIS.v2, FRGC and CASIA.v4-distance databases, respectively.

5.2.3 Combination of Global and Local Matching Scores

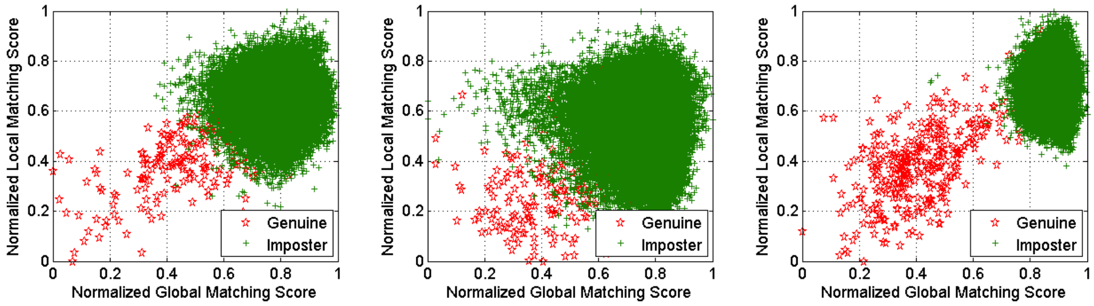

(a) UBIRIS.v2 (b) FRGC (c) CASIA.v4-distance

Figure 5.7: Normalized matching score distributions for the proposed global and local encoding approaches.

In order to simultaneously employ both global and localized iris features, the presented approaches in Sections 5.1.1 and 5.1.2 are combined at score level based on the weighted sum rule: $score = w_1 \times score_1 + w_2 \times score_2$ and $w_1 + w_2 = 1$. The receiver operating characteristic and cumulative match characteristic curves on the three employed databases are shown in Figure 5.10 and Figure 5.11 respectively. It can be observed that the recognition performance from the phase encoding information of ZMs clearly outperforms the magnitude encoding information of ZMs on three employed databases. Such results have further confirmed that the phase information of ZMs can offer more discriminative power than the magnitude information. The distribution of genuine and imposter matching scores for the test data on each of the three databases considered in this work is shown in Figure 5.7. This figure suggests that the simultaneous use of matching scores from the global and local iris region pixels can be used to achieve better matching accuracy. These experimental results illustrate significantly improved performance and suggest the superiority of the proposed joint strategy of using matching information from both the global and localized iris features. The combined scores from the global and localized iris features achieve better discrimination than employing either global or localized iris representation alone.

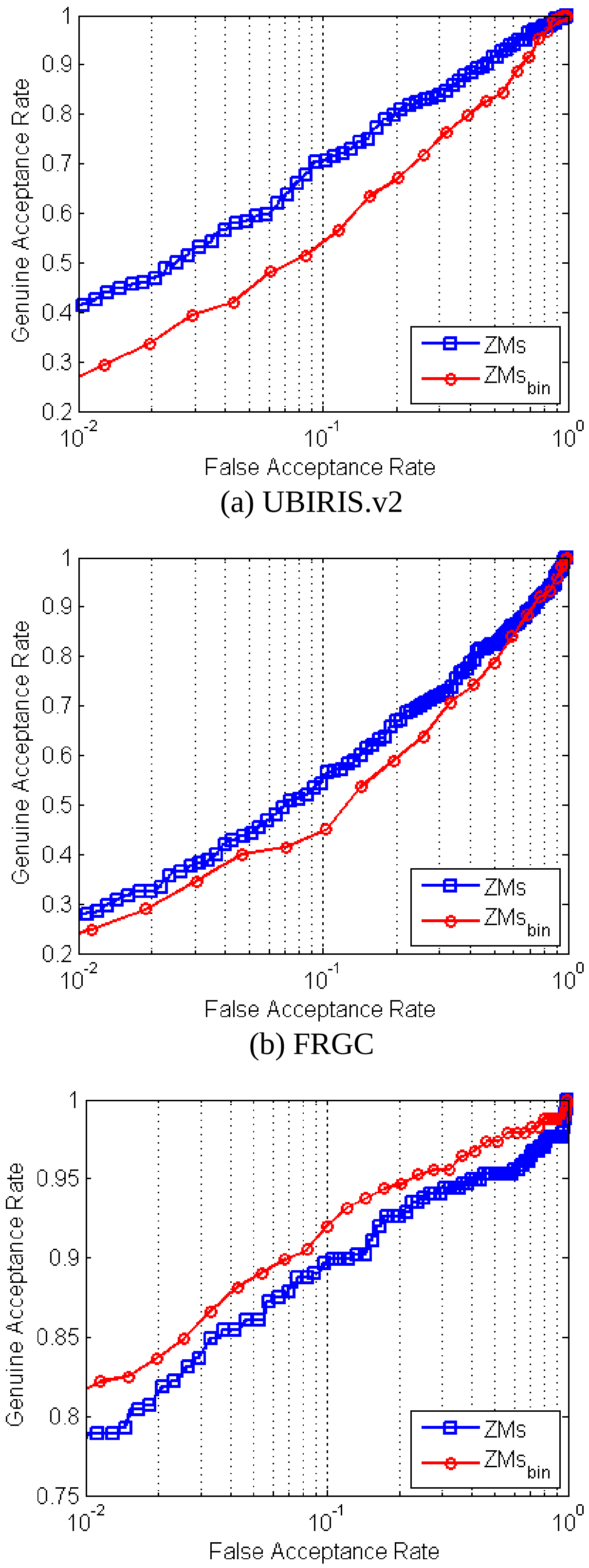

(a) UBIRIS.v2

(b) FRGC

(c) CASIA.v4-distance

Figure 5.8: Receiver operating characteristic curves from the proposed ZMs phase-based encoding approach.

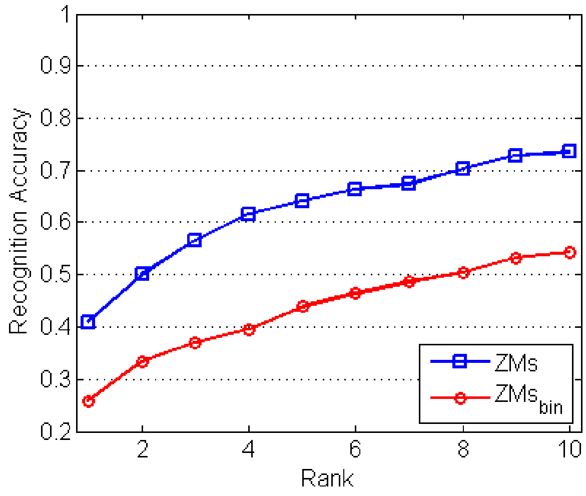

(a) UBIRIS.v2

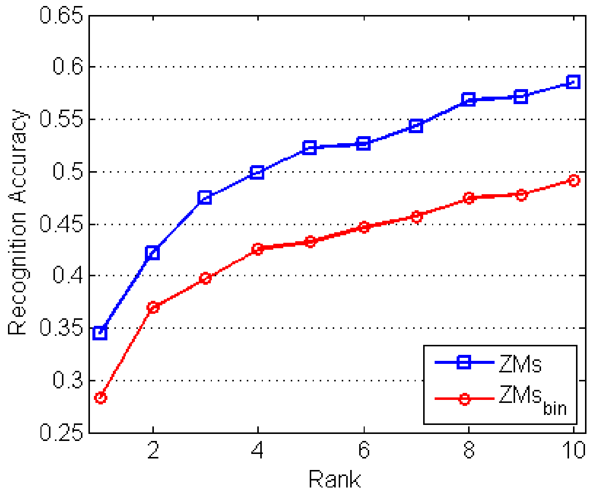

(b) FRGC

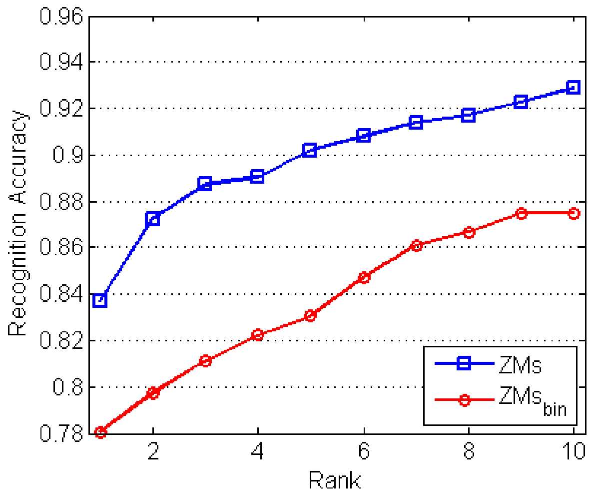

(c) CASIA.v4-distance

Figure 5.9: Cumulative match characteristic curves from the proposed ZMs phase-based encoding approach.

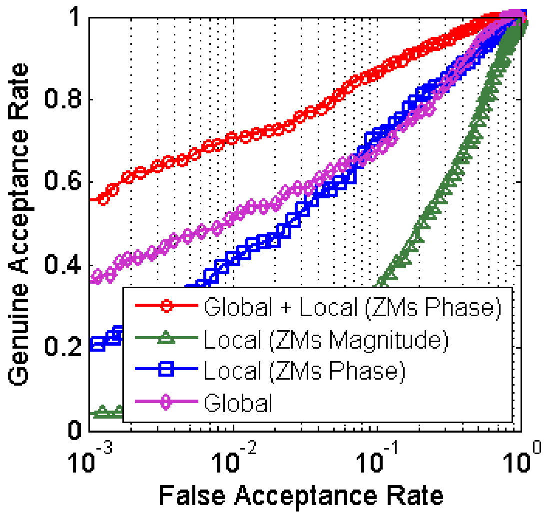

(a) UBIRIS.v2

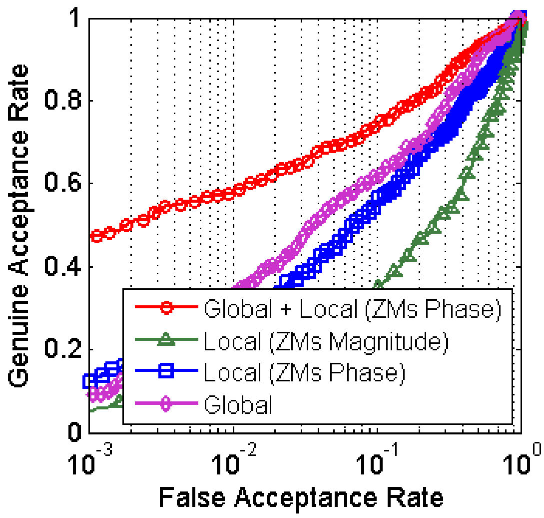

(b) FRGC database

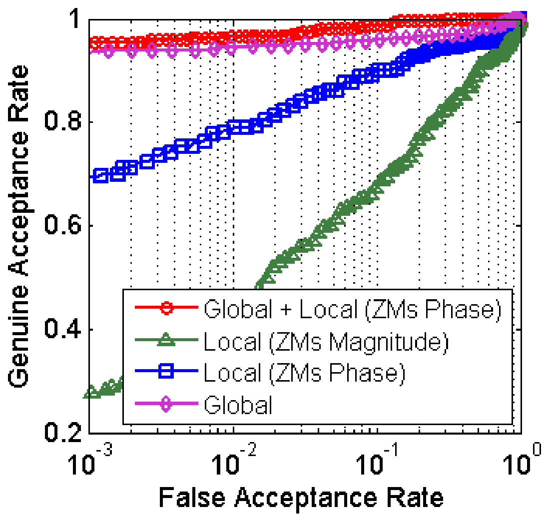

(c) CASIA.v4-distance

Figure 5.10: Receiver operating characteristics from the proposed.

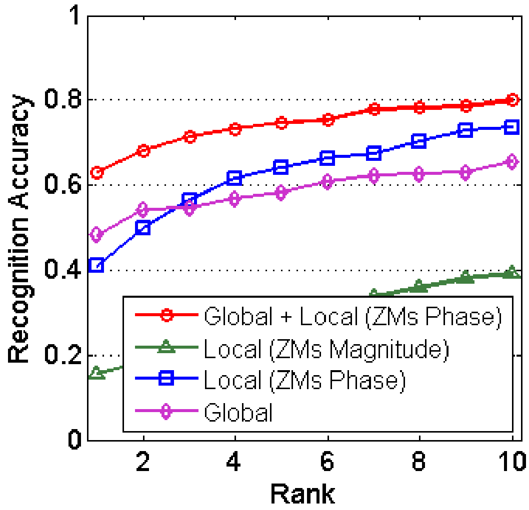

(a) UBIRIS.v2

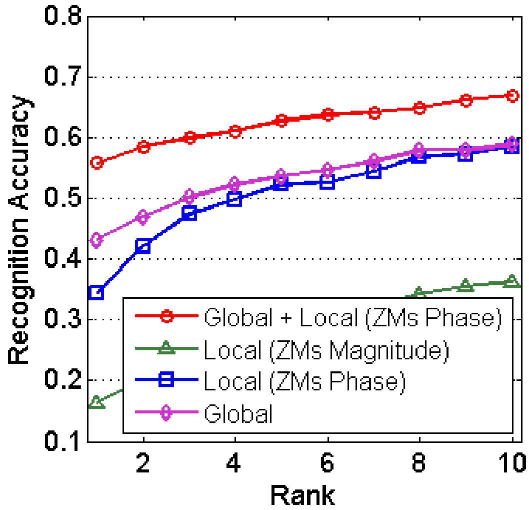

(b) FRGC

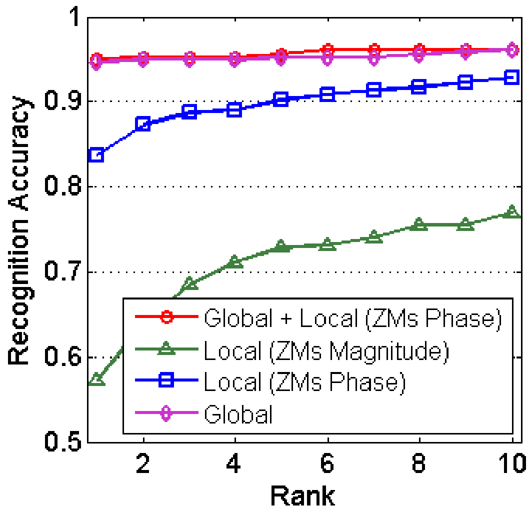

(c) CASIA.v4-distance database

Figure 5.11: Cumulative match curves from the proposed approach.

5.2.4 Performance Comparison

We have also provided comparison with several competing iris matching approaches presented in the literatures: Fragile Bits [47], [48], Personalized weight map (PWMap) [62], band-limited phase only correlation (BLPOC) [56], log-Gabor [66] and Sparse [61][p]. The ROC and CMC curves obtained for the various approaches using the same protocol are respectively shown in Figure 5.12 and Figure 5.13. The EER and the *d*'[q] are two most common performance metrics employed in the iris biometrics in the literature [52], [62], [94]. The estimated recognition performance from the various iris matching approaches in this work as indicated using EER and *d*' are summarized in the Table 5.3. The proposed iris matching approach outperforms the other approaches in both the EER and the decidability index. Figure 5.14 illustrates the percentages of improvement for the proposed approach in terms of EER as compared to the other methods. In summary, the proposed iris matching approach achieves significant improvement over several state-of-the-art iris matching techniques, which suggests average percentage of improvement of *54.3%, 32.7%* and *42.6%* respectively on UBIRIS.v2, FRGC and CASIA.v4-distance databases.

Table 5.3: The Equal Error Rate and decidability index obtained by the different approaches from the three employed databases.

	UBIRIS.v2		**FRGC**		**CASIA.v4-distance**	
Method	**EER**	***d*'**	**EER**	***d*'**	**EER**	***d*'**
Sparse [61]	0.1922	1.5842	0.2397	1.4298	0.0445	3.4345
PWMap [62]	0.2608	1.37	0.2681	1.1448	0.0564	3.4170
Fragile Bits [48]	0.2534	1.0923	0.2961	0.8284	0.0418	3.3054
BLPOC [56]	0.4022	0.4528	0.4396	0.2773	0.1136	2.6748
Log-Gabor [66]	0.2745	0.9266	0.2960	0.8280	0.0385	3.1525
Proposed	**0.1196**	**2.5735**	**0.1986**	**1.8899**	**0.0290**	**6.4735**

[p] The source code is publicly available at:
http://www.umiacs.umd.edu/~jsp/Research/SRRecognition/SparseRecognitionCancelability_PAMI2010.zip
[q] Decidability index is employed in NICE.II competition as performance indicator to evaluate the performance of iris encoding and matching algorithms.

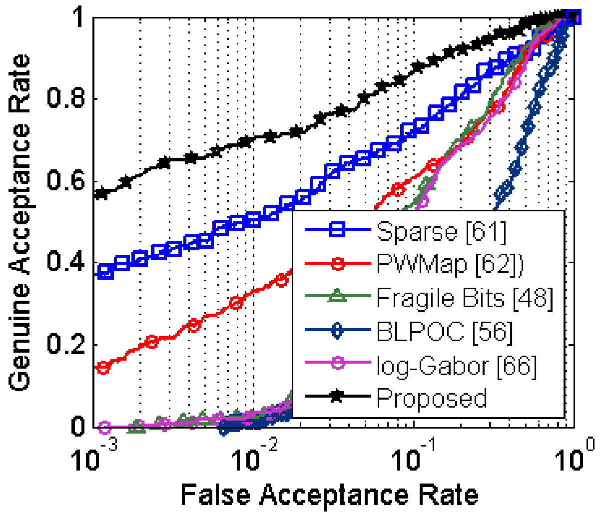

(a) UBIRIS.v2

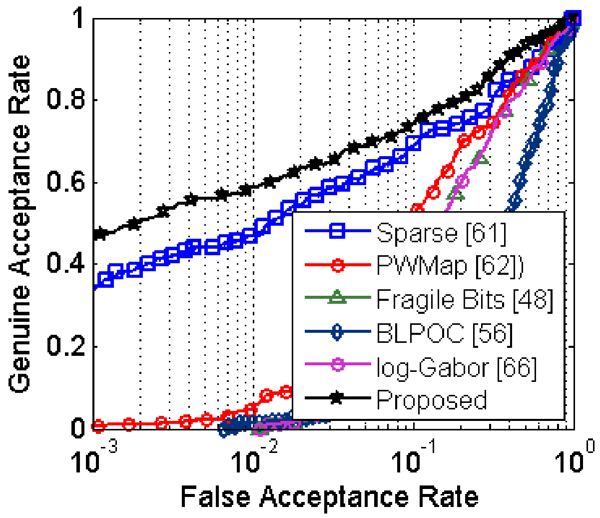

(b) FRGC

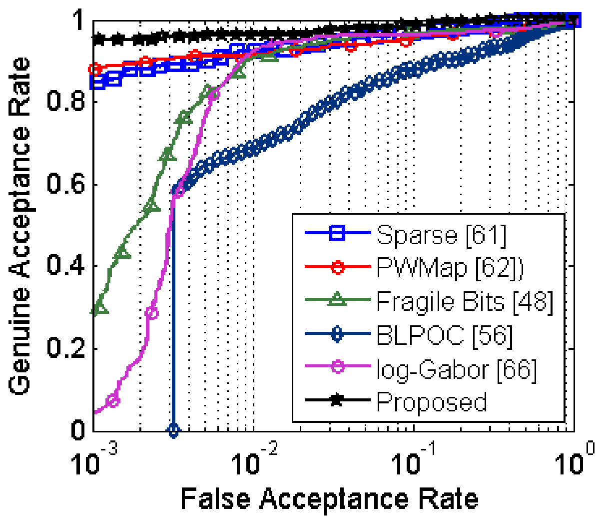

(c) CASIA.v4-distance

Figure 5.12: Receiver operating characteristics from various approaches.

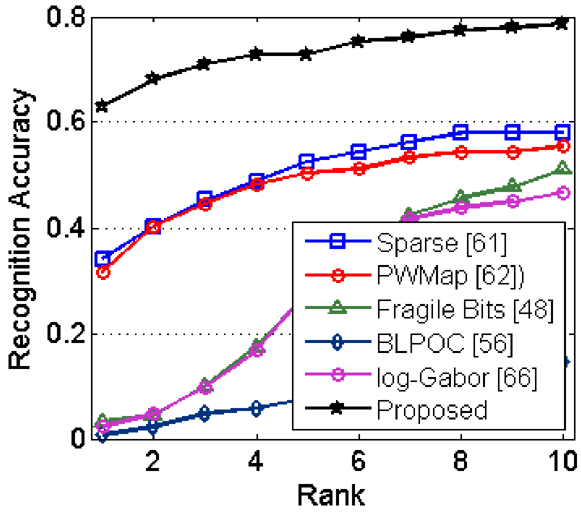

(a) UBIRIS.v2

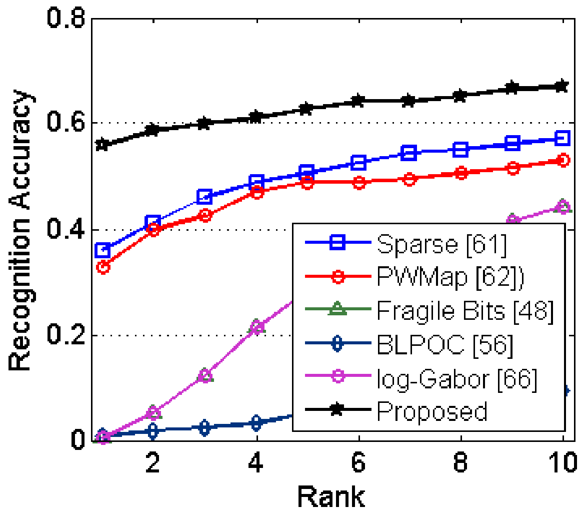

(b) FRGC

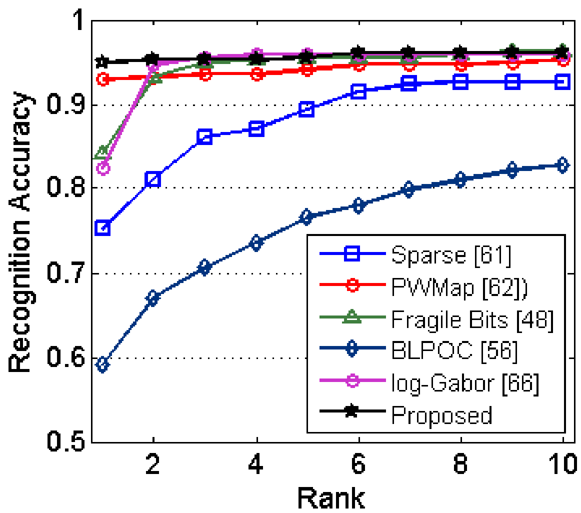

(c) CASIA.v4-distance

Figure 5.13: Cumulative match curves from various approaches.

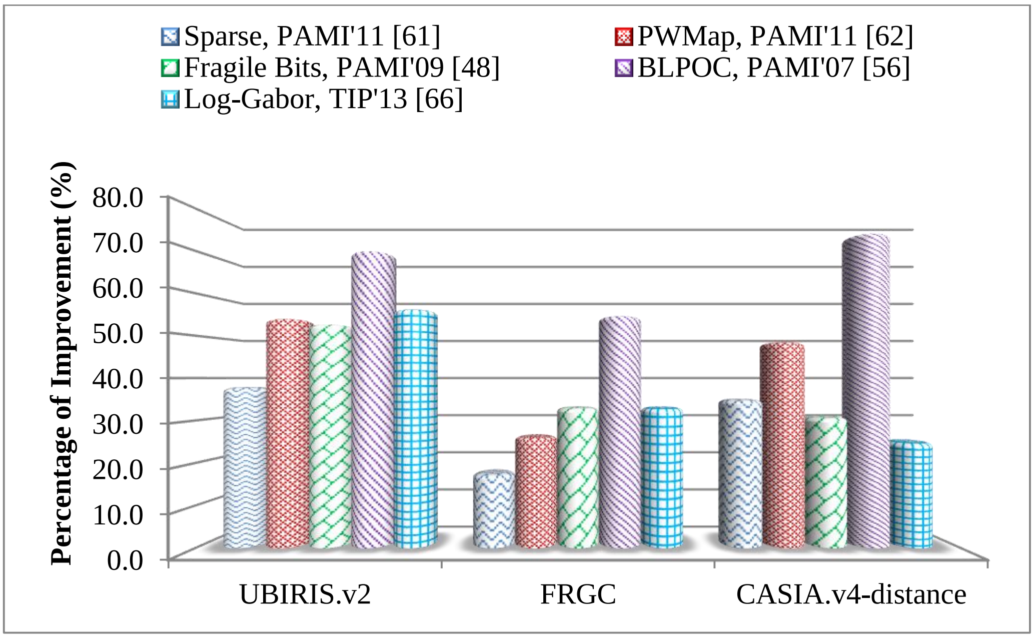

Figure 5.14: Expected improvement in Equal Error Rate as compared to the competing approaches in literature.

In order to establish a fairer comparison, we made another attempt to compare our proposed strategy with the combination of the best two methods reported from each of the employed databases. The matching information from the two methods are combined at score level based on the weighted sum rule, and the parameter employed for such fusion is summarized in Table 5.4. As Figure 5.15 shows, the proposed strategy is again outperforms the joint strategy of the best two reported methods from our experiments, which further ascertain the effectiveness of the proposed joint global and localized iris encoding and matching strategy. The superiority of using such joint matching strategy can be mostly attributed to the complementary matching information from both the global and localized iris region pixels. As mentioned earlier, the localized iris encoding strategy can be more tolerant to imaging variations and noise, while the global iris encoding strategy has its strength in less noisy iris region pixels, as can be well reflected by the fusion weights as employed for our joint matching strategy. For the two very challenging visible illumination eye/face databases, *i.e.*, UBIRIS.v2 and FRGC, more weights are assigned to the localized encoding method. For the CASIA.v4-distance database in which better quality of the eye images can be expected, more weight is assigned

Table 5.4: Parameter employed for score combination.

Database	Method		Weight		Rank-one Recognition Rate
	Method 1	Method 2	w_1	w_2	
UBIRIS.v2	PWMap [62]	Sparse [61]	0.49	0.51	49.6%
	Proposed (Global)	Proposed (Local)	0.43	0.57	**63%**
FRGC	PWMap [62]	Sparse [61]	0.49	0.51	48.4%
	Proposed (Global)	Proposed (Local)	0.485	0.515	**55.8%**
CASIA.v4-distance	PWMap [62]	Fragile Bits [48]	0.61	0.39	93.8%
	Proposed (Global)	Proposed (Local)	0.7	0.3	**95%**

matching information from the joint strategy of global and localized iris encoding can provide more accurate recognition accuracy for the iris recognition at-a-distance and under less constrained environments.

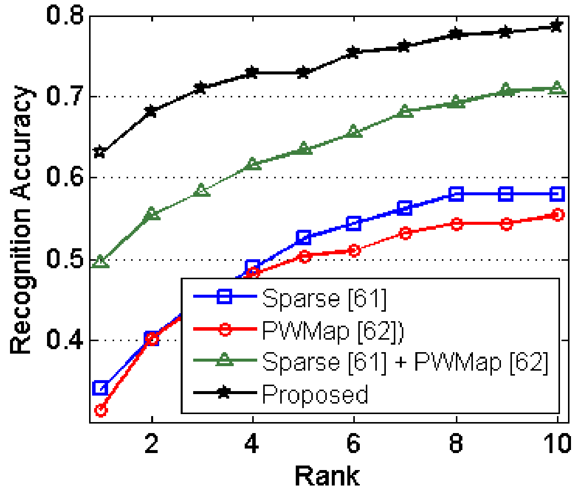

(a) UBIRIS.v2

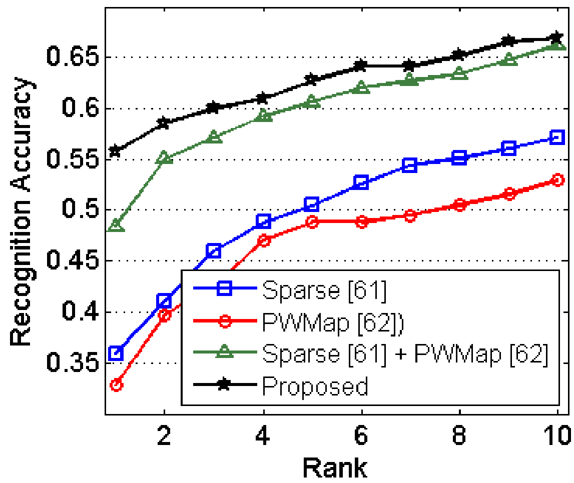

(b) FRGC

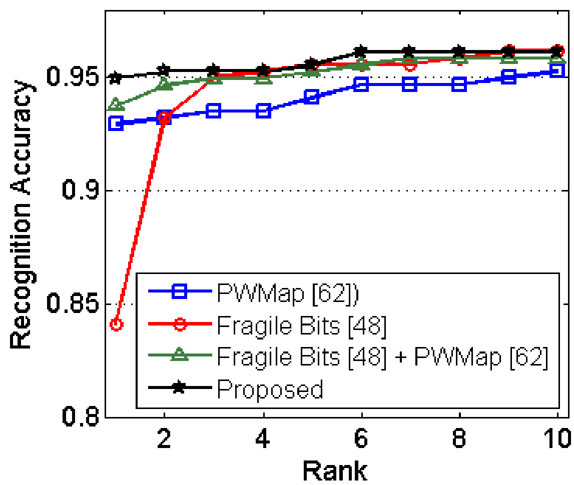

(c) CASIA.v4-distance

Figure 5.15: Cumulative match curves from the comparison with the best two reported iris matching methods.

5.2.5 Discussion

The recognition performance achieved by the proposed approach is quite encouraging, especially for the iris images acquired remotely using visible illumination and under less constrained environments. For example, the estimated decidability index of 2.5735 on UBIRIS.v2 database is comparable to the reported result from the winning algorithm ($d' = 2.5748$) in NICE.II competition [90]. Such competition employed decidability index as the performance metric in the evaluation of the iris matching algorithms participated in the competition. It is worth noting that the iris matching strategy investigated in this chapter only employs the iris features and does not consider the multimodal (*e.g. periocular*) strategy as in the case of [64], which has been declared as winning algorithm in the NICEII competition. Therefore, if we employ such combination strategy, the recognition performance improvement can also be expected (see CHAPTER 6). In addition, the participated algorithms in NICE.II competition were evaluated on the noise-free iris images[r], which may not be well-suited to provide accurate estimation of the actual performance for a deployable iris recognition system. As such, all the presented iris matching approaches in this paper were evaluated on the iris images which were segmented by employing a fully automated iris segmentation approach [66] (see CHAPTER 4). Therefore, our experimental results can better reflect the actual performance of *at-a-distance* iris recognition strategy acquired under *less constrained environments*.

In spite of the superiority in the recognition performance as demonstrated from our experiments, the memory requirement and computational complexity are other important considerations should also be investigated. As such, we also analyze the memory requirements and the computational complexity of the proposed iris matching strategy based on the parameters as provided in Table 5.2. In order to provide the complexity analysis which can be independent across different implementation environments, we also employ the similar analysis approach as in [62] to investigate the complexity of the iris matching algorithm proposed in this paper. For the global iris feature representation, higher memory is required due to

[r] The iris images are manually segmented and can be considered to have less influence (neglectable) from segmentation errors.

the remapping operation (Section 5.1.1). For example, the remapped dimension for a normalized iris image from the UBIRIS.v2 is 1024×128 bits (16 kB). The corresponding weight map requires 128 kB of the memory storage, such that the fraction values are quantized into the integers of range $[0{,}255]$ (1 byte). The memory storage required by the localized iris representation depends on a number of factors: (i) total number of image blocks, (ii) order of ZMs, (iii) repetition of ZMs, and (iv) size of occlusion mask. The occlusion mask has the same dimensionality as the normalized iris image. For example, the dimension of occlusion mask for the UBIRIS.v2 is 512×64 bits (4 kilobytes). Due to the remapping operation in the global iris feature representation phase, the incurred computational cost in iris matching is expected to increase. For example, the global iris feature representation computed from the UBIRIS.v2 requires 2048 XOR operations on a 64-bit machine, 131072 element-wise weight multiplication operation (MUL) and a multiplication for the $1/\|W^j\|$ (can be precomputed during the weight map training phase). The

Table 5.5: Memory requirement and the computational cost of the proposed iris matching strategy.

Database	**Memory requirement per template (kilobyte)**		**Computational cost (matching)**	
	Global	***Localized***	***Global***	***Localized***
UBIRIS.v2	16 + 128	3.125 + 4	2048XOR + 131072MUL + 1MUL	200MUL + 200DIV + 200DIV + 200MUL + 200INC
FRGC	4 + 32	1.8125 + 1	512XOR + 32768MUL + 1MUL	116MUL + 116DIV + 116DIV + 116MUL + 116INC
CASIA.v4-distance	16 + 128	6.25 + 4	2048XOR + 131072MUL + 1MUL	400MUL + 400DIV + 400DIV + 400MUL + 400INC

incurred computational cost for the localized iris feature representation depends on the dimension of the computed feature vector. For instance, the dimension of the feature vector computed from a normalized iris image of the UBIRIS.v2 is $\mathbf{C}^{200}$ (complex number). The matching requires 200 element-wise multiplication operations, 200 element-wise division operations (DIV), 200 element-wise division operations to extract phase angles, and 200 multiplication (square) and incremental sum (INC) operations (approximation to the L2-norm). Table 5.5 summarizes the incurred memory storage and the computational cost as required by the proposed iris matching strategy on each of the employed databases. It is obvious to observe that higher computational cost is required for the global iris feature representation, which is mainly due to the employed block overlapping operation to account for spatial variations in the iris images acquired at-a-distance and under less constrained environments. In contrast, the localized iris feature representation requires much lower computational cost, which is mainly attributed to the low order moments of the computed ZMs features.

5.3 Summary

In this chapter, a promising iris encoding and matching strategy for the iris images acquired at-a-distance, using both NIR and visible imaging, under less constrained environments is investigated. Such iris images acquired at-a-distance and under less constrained imaging conditions are often degraded due to noise introduced by multiple sources, and therefore it is more likely to distort the iris texture details (*e.g.* scale, rotation, blur, off-angle, occlusion, *etc*.). Therefore, the segmented iris images following the iris normalization step reveals the distorted texture details which can be varying even for the iris images from the same class. The approach presented in this chapter exploits a *global iris bits stabilization encoding strategy* and a *localized ZMs phase-based encoding strategy* to robustly recover the iris features. Our strategy has been to simultaneously ascertain the matching information from the local region pixels (which is more tolerant to the distortion) while also evaluating the matching information for the features which can preserve global matches from more stable texture patterns/regions. A joint strategy to simultaneously employ the encoded global and localized iris features can benefit from both of these approaches. The experimental results obtained from three publicly available databases: UBIRIS.v2, FRGC, CASIA.v4-distance, establish the superiority of the proposed iris matching strategy and achieve average improvement of *54.3%*, *32.7%* and *42.6%* in EER, respectively. Despite the encouraging results obtained by the proposed iris matching strategy, further efforts are required to improve the matching accuracy, especially for the visible-light iris matching in order to make any inroads to the commercial applications. Efficiency of the iris matching algorithm and the recognition accuracy are the two prime criterions for selecting an algorithm for the deployment. Therefore further efforts should also be directed to develop more efficient iris matching algorithms which can simultaneously operate on images acquired in dynamic spectral illumination under less constrained environments.

CHAPTER 6

Periocular Recognition

Periocular or ocular is referred to the region around the eye [96]. Such region is typically acquired simultaneously with the eye without incurring additional hardware cost, and therefore can be exploited to further improve the recognition accuracy of the iris recognition at-a-distance and under less constrained imaging conditions. In this chapter, we provide evaluation on several commonly employed feature extraction methods such as SIFT [76], [118], GIST [119], LBP [120], HoG (histogram of oriented gradients) [121] and LMF (Leung-Malik Filters) [122] for computation of periocular features. The strategy to jointly exploit iris and periocular strategy suggests promising results and achieves improvements of 63.6%, 43.5% and 28.3% in equal error rates, respectively from the UBIRIS.v2, FRGC and CASIA.v4-distance database, as compared to the reported results in CHAPTER 5.

6.1 Methodology

6.1.1 Segmentation of Periocular Region

Currently, there is no clear definition about what the size of the periocular region should be, *e.g.* refs. [96], [123] use the periocular region which is quite different from the [124]. However, the automated segmentation of periocular region, *e.g.* those in [96], [123], is more challenging in less constrained imaging environment as the size of the periocular region is highly dependent on the distance between the user and the camera. Ref. [96] provides a promising solution to address such issue by employing the localized iris information (x_{ir}, y_{ir}, r_{ir}) to compute a rectangular region centered at the iris center, which is invariant to both scale and translation.

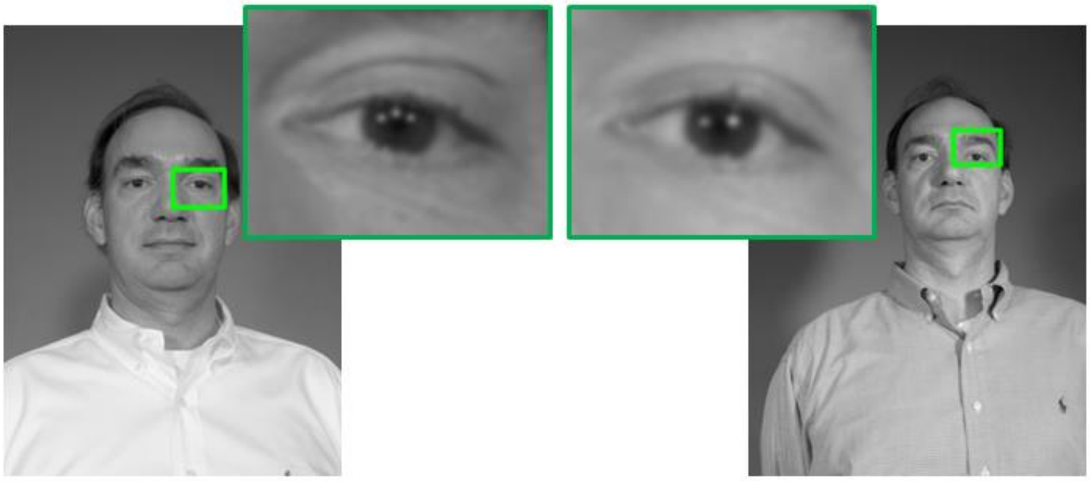

Figure 6.1: Segmentation of periocular regions from face images acquired at-a-distance (left eyes are employed for better illustration and comparison).

Firstly, the input image is normalized (upscaling/downscaling) *w.r.t* a scale factor $s_f = {}^{r_{norm}}/_{r_{ir}}$, where r_{norm} is to the normalized iris radius. Such normalization operation results in the shifting of the original localized iris center (x_{ir}, y_{ir}) in the normalized eye image I_{s_f}, and the updated iris center is given as $(\widetilde{x_{ir}}, \widetilde{y_{ir}}) = s_f(x_{ir}, y_{ir})$. The periocular region R_{pe} is then defined as the rectangular region of size $\grave{w} \times \grave{h}$ centered at $(\widetilde{x_{ir}}, \widetilde{y_{ir}})$. The $\grave{w}$ and $\grave{h}$ correspond to the width and the height of R_{pe}, which are defined as $\grave{w} = r_{norm} \times f_w$ and $\grave{h} = r_{norm} \times f_h$, respectively. The factors f_w and f_h are fixed for all the images from the same dataset to ensure the consistent size of the R_{pe} can be obtained. We set $f_w = \{6,6,8\}$ and $f_h = \{4,4,6\}$ for the UBIRIS.v2, FRGC and CASIA.v4-distance databases, respectively. Figure 6.1 shows the sample segmentation of the periocular regions from the same subject.

6.2 Experiments and Results

Recognition performance of using periocular biometrics has been shown to be encouraging [96], [123], [124], [125] and can be further exploited to improve the recognition accuracy of the iris recognition at-a-distance and under less constrained environments. In this section, we first provide the performance comparison between several commonly used periocular feature extraction methods: SIFT [76], [118], GIST [119], LBP [120], HoG (histogram of oriented gradients) [121] and LMF (Leung-Malik Filters) [122], as obtained from the rigorous experiments conducted on three publicly available databases with images acquired at-a-distance and under less constrained environments using either visible or NIR imaging. Such comparison can be advantageous in order to select the feature extraction method which can be more adaptive to each of the employed database. Later on, a joint strategy is employed to combine the simultaneously acquired iris and periocular matching scores, which has been shown to be effective to provide more accurate recognition accuracy especially for the distantly acquired visible illumination based eye images.

6.2.1 Comparison between Different Feature Extraction Methods

Table 6.1: Overview of the three employed databases.

	UBIRIS.v2	**FRGC**	**CASIA.v4-distance**
Operating illumination	visible	visible	NIR
Acquisition distance (meter)	4 – 8	N/A	≥ 3
Original image size	400 × 300	1200 × 1600	2352 × 1728
No. of training images / subjects	96 / 19	40 / 13	79 / 10
No. of test images / subject	904 / 152	500 / 150	995 / 131

The experiments were conducted with the identical protocol as described in [66] on three publicly available databases namely: (i) UBIRIS.v2 [40], [90], (ii) FRGC [109], [10], and (iii) CASIA.v4-distance [110]. Table 6.1 provides the summarized information about the dataset as employed in the experiments. Two types of experiments namely *Experiment I* and *Experiment II* were carried out in order to investigate the performance of the feature extraction methods on *global* and *local* periocular regions.

- *Experiment I*: The segmented periocular region R_{pe} (see Section 6.1.1) was employed in this experiment[s]. Such segmented region is referred as *local* periocular region in this chapter. Figure 6.2 shows the cumulative match

[s] Iris segmentation for this experiment was performed using the automated iris segmentation approach as detailed in CHAPTER 4.

characteristic curves of the different periocular extraction methods obtained from the three employed databases. The best of the rank-one recognition rates of *38.5%* and *53.1%* are reported from the DSIFT method on the UBIRIS.v2 and FRGC databases respectively. While the best of the rank-one recognition rate of 83.3% is reported from the LMF method on CASIA.v4-distance database.

- *Experiment II*: In [124], the periocular features were computed directly from the localized eye region (the detected eye region) without involving segmentation step as described in Section 6.1.1. Therefore, the periocular region is considered as the immediate region detected by the eye detector[t], which is referred as *global* periocular region in this thesis. Such global periocular region is particularly useful if the iris segmentation fails or the segmented iris image does not meet the minimum quality requirements to be

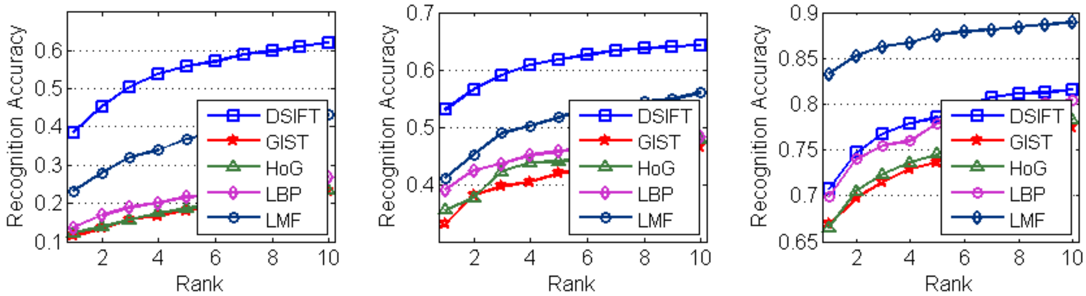

(a) UBIRIS.v2 (b) FRGC (c) CASIA.v4-distance

Figure 6.2: Cumulative match characteristic curves of different periocular feature extraction methods computed on local periocular regions.

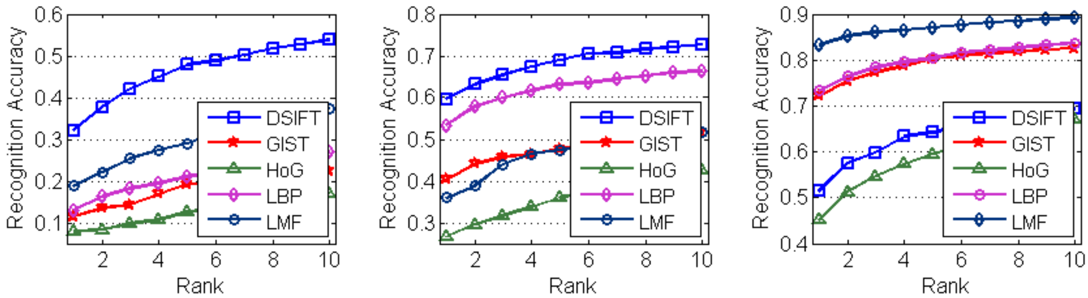

(a) UBIRIS.v2 (b) FRGC (c) CASIA.v4-distance

Figure 6.3: Cumulative match characteristic curves of different periocular feature extraction methods computed on global periocular regions.

[t] Note that the UBIRIS.v2 database provides the localized eye images and therefore eye detection is not required for the images from this database.

(a) UBIRIS.v2

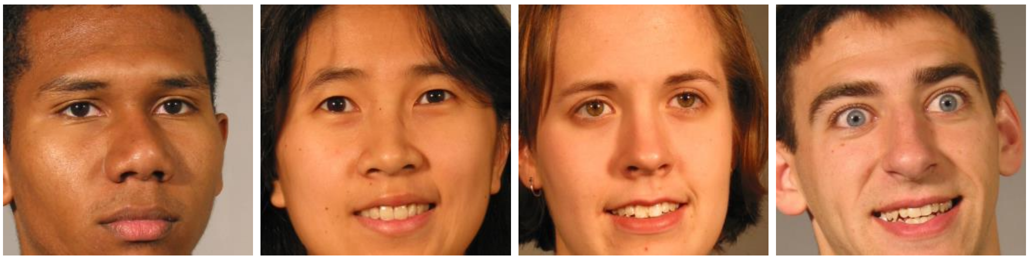

(b) FRGC

(c) CASIA.v4-distance

Figure 6.4: Sample images from the three employed databases.

used for the recognition. Unlike the local periocular region, the size and the location of the global periocular region is less consistent as such region is highly dependent on the detected eye region. For that reason, experiment II was carried out to objectively investigate the performance of the various feature extraction methods considered in this chapter on such global periocular region. Figure 6.3 shows the cumulative match characteristic curves of the various periocular extraction methods obtained from the three employed databases. The best of the rank-one recognition rates of 32.2% and 59.7% is observed from the DSIFT method on the UBIRIS.v2 and FRGC databases, respectively. The rank-one recognition rate of 83.2% is reported from the LMF method on the CASIA.v4-distance database.

It can be observed that the experimental results on the UBIRIS.v2 database reported the lowest recognition accuracy among the three employed databases. One of the possible reasons of such discouraging performance may due to the lack of the

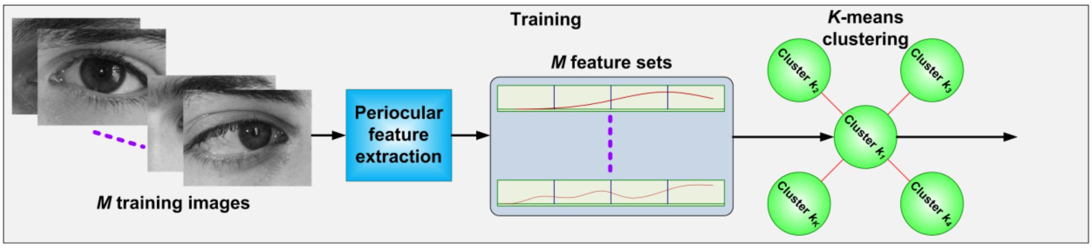

(a) Training stage

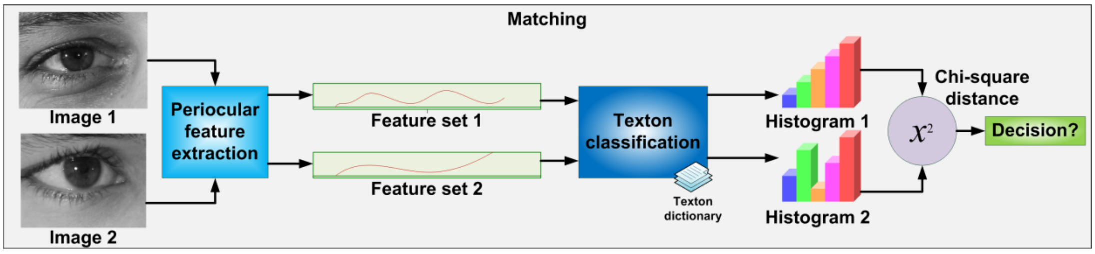

(b) Classification and matching stage

Figure 6.5: Block diagrams of the developed periocular recognition approach.

adequate periocular region (*e.g.* eyebrow, malar fold and nasojugal fold) for feature recovery. The eye images provided from the UBIRIS.v2 database were *pre-cropped* and therefore are not adequate to represent a more complete structure of the periocular region, as compared to the images from the FRGC and CASIA.v4-distance databases, as depicted in Figure 6.4. The best recognition accuracy is observed from the DSIFT method on the local periocular region for the UBIRIS.v2 database. For the FRGC database, the best recognition accuracy is observed from the DSIFT method on the global periocular region. While similar recognition performance is observed from the LMF method on both the local and global periocular regions for the CASIA.v4-distance database.

Promising recognition performance using periocular features has been ascertained through the *Experiment I* and *II*. As such, the procedure of the best performing methods, *i.e.*, DSIFT and LMF is further detailed in this section, as can also be seen from Figure 6.5. The developed periocular recognition approach consists of two stages: (i) training and (ii) classification and matching, which can be generally adopted for both the DSIFT and LMF feature extraction methods. The training stage is aimed to build a texton dictionary which comprises of k primitive representative textons recovered from the computed feature sets. Such feature sets

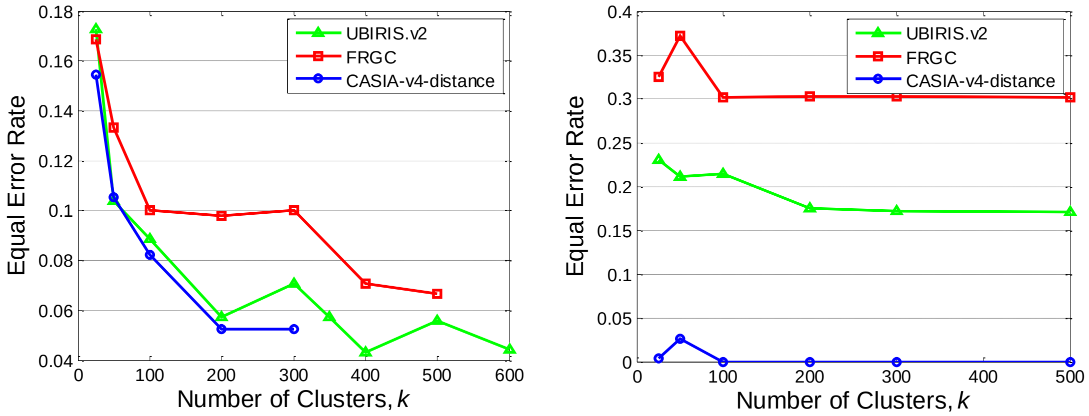

(a) DSIFT (b) LMF

Figure 6.6: Estimation of the parameter k for constructing texton dictionary.

are obtained by applying the feature extraction method (DSIFT/LMF) to the periocular regions (local/global) of M training images. A texton dictionary is then constructed by employing k-means algorithm to recover k primitive representative textons from the computed feature sets. The parameter k was estimated from a discrete set of k-values for both DSIFT and LMF features, as shown in Figure 6.6. In the matching stage, the periocular features are extracted similarly as in the training stage. The extracted features are classified using the constructed texton dictionary to form a texton distribution as represented by a k-bin histogram H. Therefore, the similarity between two given k texton distribution H_1 and H_2 can be computed using chi-square distance (CSD), as given as follows:

$$CSD(H_1, H_2) = \frac{1}{2}\sum_{j=1}^{k}\frac{\left(h_{1j} - h_{2j}\right)^2}{h_{1j} + h_{2j}}, \tag{6.1}$$

where $\{h_{11}, \dots, h_{1k}\} \in H_1$ and $\{h_{21}, \dots, h_{2k}\} \in H_2$. Lower CSD value indicates higher similarity between the two texton distributions while higher CSD value indicates otherwise.

6.2.2 Combination of Iris and Periocular Matching Scores

The simultaneously acquired periocular region features can be further exploited to achieve more accurate recognition accuracy for the iris recognition at-a-distance and under less constrained environments. We show that by combining the matching information from the both the extracted iris (see CHAPTER 5) and periocular features, the recognition performance can be significantly improved, especially for the visible illumination based images. We followed the identical protocol [u] as presented in Section 5.2.1 to perform the experiments. The recovered iris features are combined with the best performing periocular features (DSIFT/LMF) based on weighted sum rule at score level. Such joint iris and periocular strategy suggests promising results and achieves improvements of 63.6%, 43.5% and 28.3% in equal error rates, respectively from UBIRIS.v2, FRGC and CASIA.v4-distance databases, as compared to the reported results in CHAPTER 5. The receiver operating characteristic and cumulative match characteristic curves obtained from the three employed databases are respectively provided in Figure 6.7 and Figure 6.8. The performance evaluation presented in the Equal Error Rate and the decidability index is summarized in Table 6.2. It can be observed that such strategy to jointly exploit iris and periocular features reported better recognition performance in the Equal Error Rate on the three employed databases. However, the decidability index for the combination of iris and periocular features on the CASIA.v4-distance dataset is worse than the iris alone. One of the possible reasons may due to that the NIR illumination imaging [v] was used to acquire the periocular images in such dataset.

Table 6.2: The Equal Error Rate and decidability index from joint periocular and iris strategy.

Feature / Database	*Iris*		*Iris + Periocular*	
	EER	***d'***	**EER**	***d'***
UBIRIS.v2	0.1196	2.5735	**0.0435**	**3.5743**
FRGC	0.1986	1.8899	**0.1122**	**2.5407**
CASIA.v4-distance	0.0290	**6.4735**	**0.0208**	5.3199

[u] Such protocol requires of multiple samples (gallery) for stability map estimation.
[v] Recent studies have shown that the visible light periocular images averagely achieve better recognition performance than the NIR periocular images [140].

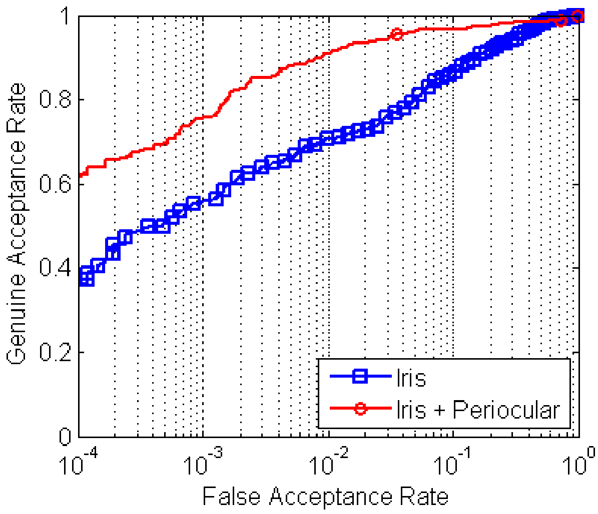

(a) UBIRIS.v2

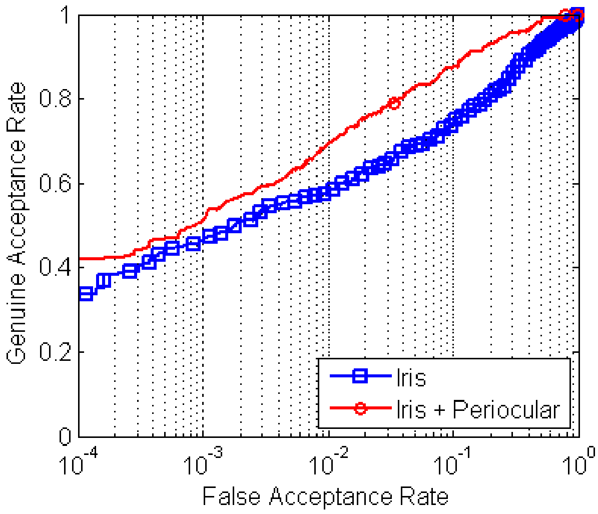

(b) FRGC

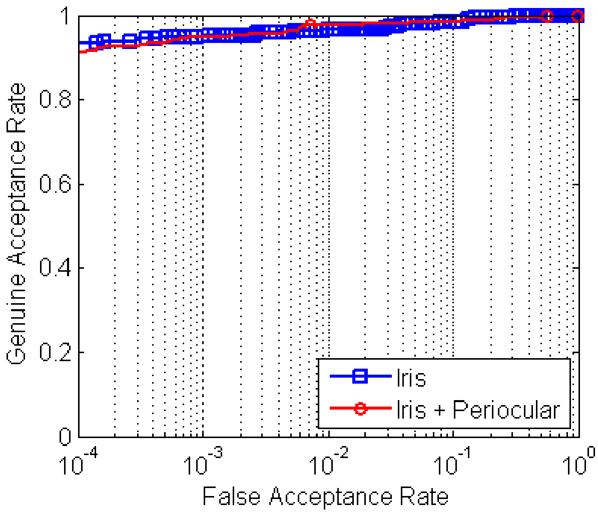

(c) CASIA.v4-distance

Figure 6.7: Receiver operating characteristics from joint periocular and iris strategy.

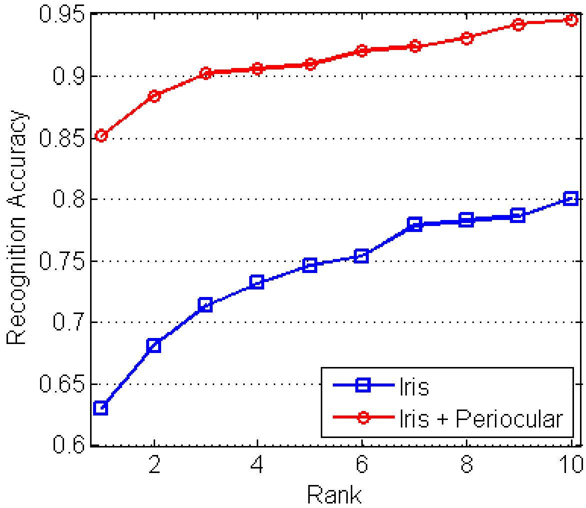

(a) UBIRIS.v2

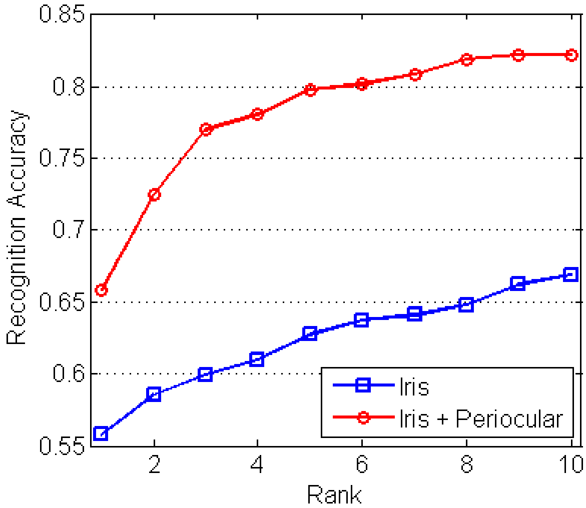

(b) FRGC

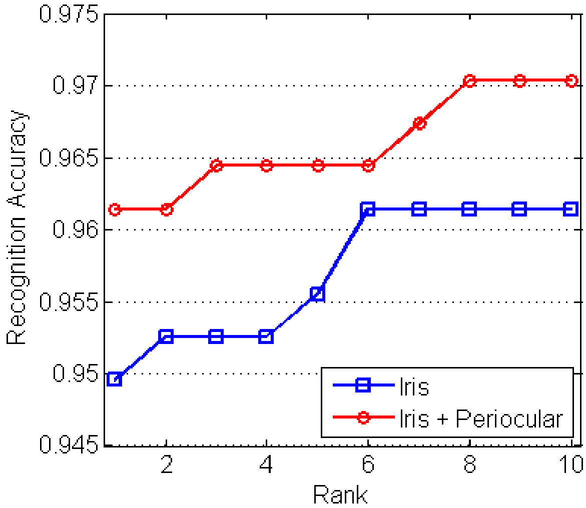

(c) CASIA.v4-distance

Figure 6.8: Cumulative match characteristics from joint periocular and iris strategy.

6.3 Summary

The work described in this chapter exploited the strategy to jointly employ the simultaneously computed iris and periocular features in order to achieve more accurate recognition accuracy for human recognition at-a-distance and under less constrained imaging conditions. The reported experimental results from such joint strategy have shown to be quite promising, especially for the images acquired using visible illumination imaging. The improvements of 63.6%, 43.5% and 28.3% in equal error rates are respectively obtained from UBIRIS.v2, FRGC and CASIA.v4-distance databases, as compared to the reported results in CHAPTER 5.

CHAPTER 7

GeoKey Iris Encoding

In this chapter, we present a computationally efficient iris encoding and matching strategy which may provide solution to address the complexity of the global iris encoding algorithm as detailed in Section 5.1.1. A set of coordinate-pairs which referred as geometric key is randomly generated and exclusively assigned to each subject enrolled into the system. Such geometric key uniquely defines the way how the iris features are encoded from the locally assembled image patches. The recovered features from such locally assembled image patches are expected to be more tolerant to the noise. Scale and rotation changes in the localized iris region can be well accommodated by using the transformed geometric key. The similarity between two recovered iris features can be efficiently computed using Hamming distance. The superiority of the proposed iris encoding and matching strategy is ascertained by providing comparison with several state-of-the-art iris encoding and matching algorithms on three publicly available databases: UBIRIS.v2, FRGC, CASIA.v4-distance, which suggests the average improvements of 36.3%, 32.7% and 29.6% in equal error rates, respectively.

7.1 Methodology

Figure 7.1 shows the block diagram of the proposed iris matching strategy for the iris images acquired at-a-distance and under less constrained imaging conditions. The proposed iris matching strategy comprises of a localized geometric key (GeoKey) encoding scheme and a global phase encoding scheme. The iris images acquired distantly and under less constrained conditions are often influenced from severer level of image variations (*e.g. scale*, *rotation*), and conventional iris encoding and matching techniques are designed to match iris images acquired from

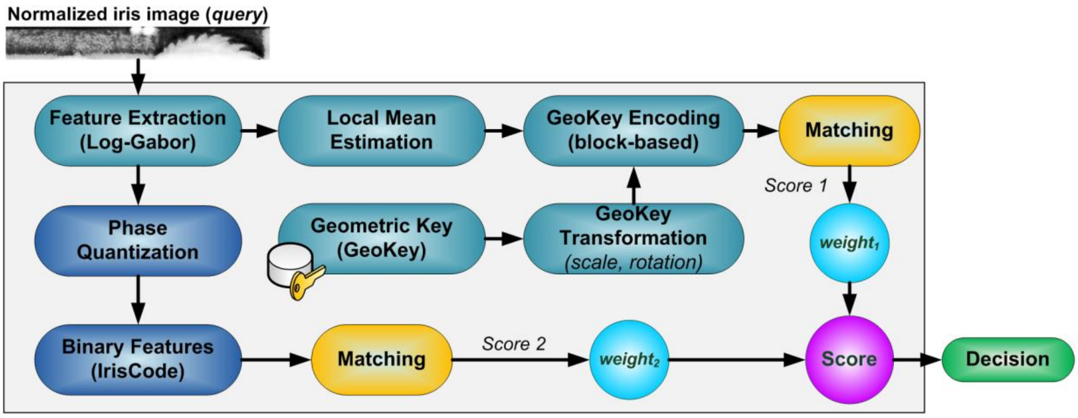

Figure 7.1: Block diagram of the proposed geometric key iris encoding scheme for iris images acquired at-a-distance and under less constrained conditions.

close distance in which iris features are more stable [31], [51], [56]. Therefore, development of feature encoding strategy that can accommodate scale and rotation variations is highly desirable. In this chapter, we propose an iris feature encoding scheme by incorporating the geometry information to encode iris texture information extracted from the localized iris region pixels. Such geometry information is determined by the GeoKey, which is a set of the coordinate-pairs exclusively assigned to each subject enrolled into the system. Therefore, the GeoKey can be considered as a unique key which is personalized to each subject and uniquely defines the geometric location to encode the localized iris features. The proposed GeoKey encoding scheme works on the locally assembled region pixels and therefore can be more tolerant to variations/noise. Furthermore, the GeoKey can be configured to account for scale and rotational changes in the localized iris region by applying simple transformation operations to the GeoKey. It is worth noting that such transformation operations are applied to the GeoKey rather than the iris images, which provide computational efficiency to encode the iris features. In order to exploit the global iris texture, the proposed scheme considers the global iris matchers such as Log-Gabor [49] to encode the global iris features. Such global iris matcher has its strength in less noisy iris region pixels and can be simultaneously computed with the localized GeoKey encoding scheme. The combined information from both the localized and the global iris matchers can provide more accurate matching accuracy and therefore can benefit us to make better decisions.

7.1.1 Generating Geometric Key

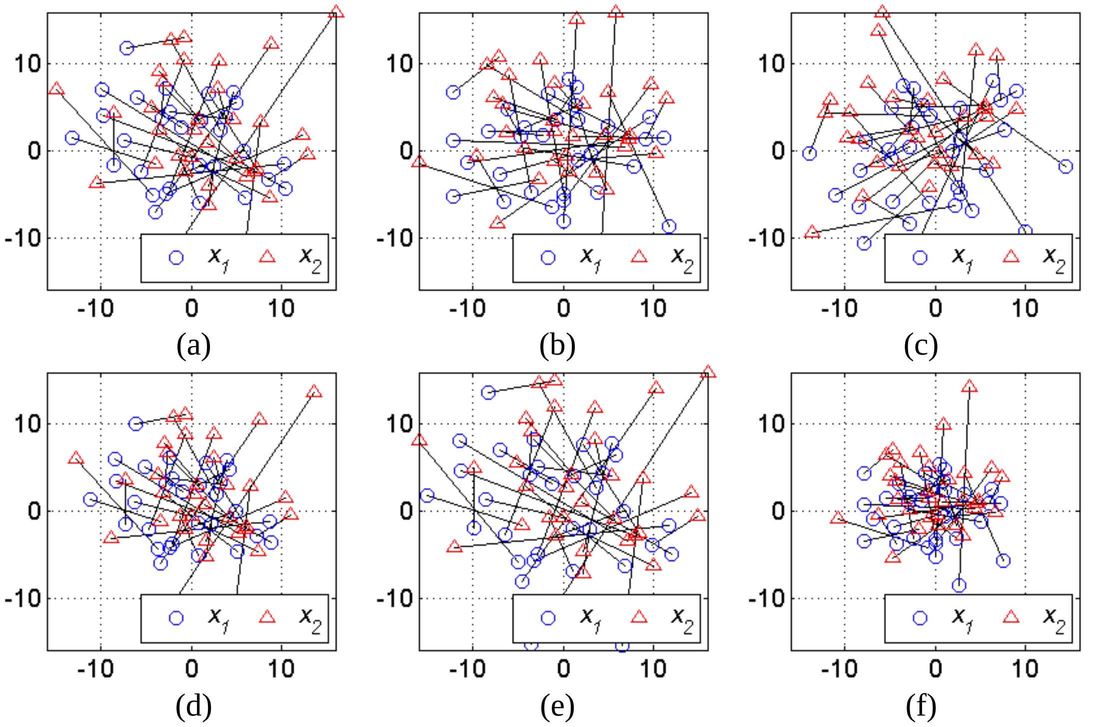

Figure 7.2: Examples of the GeoKey at different configurations ($B = 32; d = 32$). (a) original GeoKey, (b) rotation of (a) at $\theta = 30$-degree, (c) rotation of (a) at $\theta = 60$-degree, (d) scaled of (a) at $s = 0.85$, (e) scaled of (a) at $s = 1.15$, (f) scaled and rotation of (a) at $s = 0.65$ and $\theta = 30$-degree.

Geometric key K is a set of the coordinate-pairs of length d which defines the locations in an image patch of size $B \times B$. Such geometric locations as defined by the GeoKey determine how the iris features are encoded from the localized iris region pixels. We employ the best out of the five configurations as discussed in [126] to generate the coordinate-pairs of length $d \leq B^2$, which is given as:

$$\boldsymbol{K} = \left\{(\boldsymbol{x_1}, \boldsymbol{x_2}) \sim \mathrm{i.i.d.}\, G\left(0, \frac{1}{5}B\right)\right\}_{i=1,\dots,d}, \tag{7.1}$$

where $G(\cdot)$ is a Gaussian kernel with the mean equals to zero and the standard deviation equals to ${}^{1}/{}_{5}\,B$. Suppose there are N enrolled subjects in the system, a total of N GeoKeys $\{\boldsymbol{K}_d^1, \boldsymbol{K}_d^2, \ldots, \boldsymbol{K}_d^N\}$ will be generated and each of the enrolled subjects will be assigned with a GeoKey of length d.

The iris images acquired distantly and under less constrained conditions are often influenced from severer level of imaging variations such as scale and rotation in local region pixels. The proposed GeoKey iris encoding scheme can be configured to conveniently accommodate for such variations in the local region pixels. Unlike the work in [126], we apply the geometric transformations to the GeoKey rather than to the iris images using the Equation (7.2) and/or (7.3), as given below:

$$\widetilde{\boldsymbol{K}}_s = \{SK_{i=1,\ldots,d}\};\ S = \begin{bmatrix} s & 0 \\ 0 & s \end{bmatrix}, \tag{7.2}$$

$$\widetilde{\boldsymbol{K}}_\theta = \{RK_{i=1,\ldots,d}\};\ R = \begin{bmatrix} \cos\theta & \sin\theta \\ -\sin\theta & \cos\theta \end{bmatrix}, \tag{7.3}$$

where S and R represent the scaling matrix and rotation matrix [127], respectively (we use $s = \{0.85, 1, 1.15\}$ and $\theta = \{0°, 30°, 60°, 90°, 120°, 150°\}$ in the experiments). By applying the transformations on the GeoKey can be more computationally attractive as compared to the more demanding image transformation operations. The complexity of the transformations on the GeoKey depends on the key length of the GeoKey, which is typically much lower than the block size, *i.e.*, $d < B^2$ (see Table 7.1). Figure 7.2 shows the examples of GeoKey configured to encode iris features at different orientations and scales.

7.1.2 Geometric Key Encoding

Our iris encoding approach is inspired by the recent works in [126], [128] which have shown to be effective in accommodating the imaging variations from local image regions. In this work, we exploit the iris features computed from the normalized iris images by performing the binary comparisons on the smoothed version of local windows $\mathbf{w}$ of size $S \times S$ using the locations as defined by the

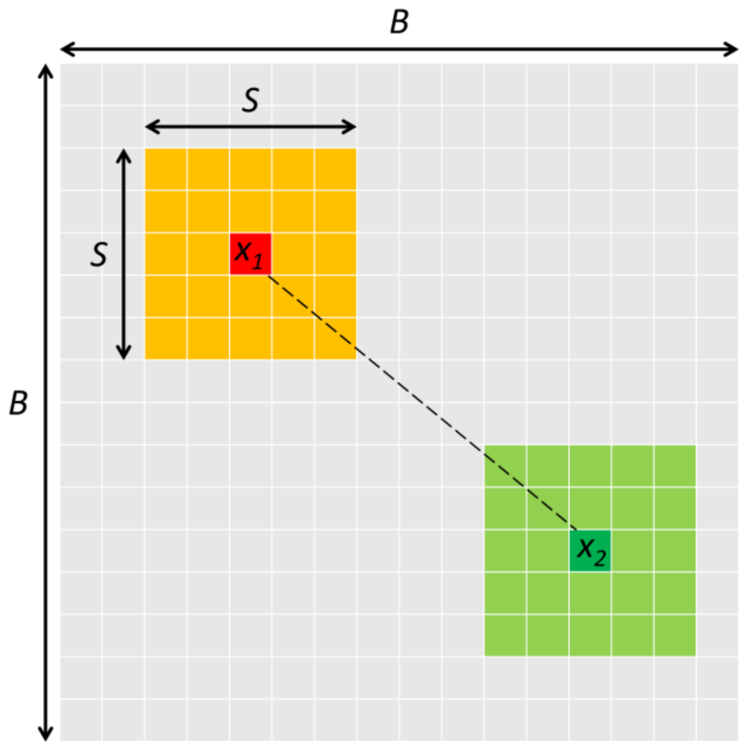

Figure 7.3: Illustration of the GeoKey iris encoding from an image patch of size $B \times B$. The binary test is performed on the local smoothing windows of size $S \times S$ centered at $\boldsymbol{x_1}$ and $\boldsymbol{x_2}$, respectively. Therefore, the $\boldsymbol{x_1}$ and $\boldsymbol{x_2}$ represent the average values of the filter responses computed from the respective local window $\mathbf{w}$.

GeoKey, as illustrated in Figure 7.3. The binary features f from an image patch can be computed as follows:

$$f(\mathbf{w}; \boldsymbol{x_1}, \boldsymbol{x_2} \in \boldsymbol{K}) = \begin{cases} 1 \; if \; L(\mathbf{w}, \boldsymbol{x_1}) < L(\mathbf{w}, \boldsymbol{x_2}) \\ 0 \text{ otherwise}, \end{cases} \tag{7.4}$$

where $L(\mathbf{w}, \boldsymbol{x_1})$ denotes the filter responses from the Log-Gabor in the smoothed version of $\mathbf{w}$ at $\boldsymbol{x_1}$. The computation of the binary features is performed on the smoothed local windows in order to provide more reliable estimation of the iris features from the local iris regions. It is worth noting that the mean values of $\mathbf{w}$ can be efficiently approximated using the integral image technique, which requires only three addition operations and a division operation. Therefore, the proposed GeoKey iris encoding scheme provides a different way from the conventional coarse phase quantization approaches [31], [49] which encodes the iris features by incorporating the geometry information. The encoded iris features are in the binary form and therefore can be efficiently matched using the modified Hamming distance, as given as follows:

$$HD^{j} = \frac{\left\| Code_{gallery}^{j} \oplus \mathbf{F}_{query}\left(\mathbf{W}, \boldsymbol{K}^{j}\right) \right\|}{p \times q}, \tag{7.5}$$

where $Code_{gallery}^{j} \in \mathbb{B}^{p\times q}$ denotes the binary gallery template of class j; $\mathbf{W} = \left[\mathbf{w}_1, \mathbf{w}_2, \dots, \mathbf{w}_{p\times q}\right]$ represents the local windows; $\mathbf{F}_{query}\left(\mathbf{W}, \boldsymbol{K}^{j}\right) \in \mathbb{B}^{p\times q}$ represents the binary query template of size $p \times q$ encoded with the $\boldsymbol{K}^{j}$; '$\oplus$' denotes the XOR operator. In this GeoKey encoding approach, we employ an overlapping block strategy to extract image patches from the normalized iris image at the interval $h = {}^{B}/_{2}$ in both horizontal and vertical directions. Therefore, the width p and height q of the template are depend on the width and height of the normalized iris image, block size $B \times B$, sliding interval h, and the key length d of GeoKey.

The proposed GeoKey iris encoding scheme is designed to provide localized encoding which can be more tolerant to the local region pixel variations such as rotation and scale changes[w]. However, the conventional coarse phase quantization approaches (global iris encoding) such as [31], [49] have its strength to encode the iris features in less noisy iris region pixels. Such coarse phase quantization approaches, *i.e.* Log-Gabor, as employed in our experiments, can be conveniently acquired since that the feature extraction is a *common* procedure prior both the localized and global encoding schemes (see Figure 7.1). Therefore, both the localized and global binarized iris features can be simultaneously computed without incurring expensive computation cost. The combined information from both the localized and the global iris matchers can provide more accurate matching accuracy (see Section 7.2) and therefore can benefit us to make better decisions.

[w] Translation can be addressed by using the conventional circular bit shift operation during the matching phase.

7.2 Experiments and Results

In this section, we detail on the experiments and present results from the rigorous experimentation on three publicly available databases: UBIRIS.v2 [40], [90], FRGC [10], [109], and CASIA.v4-distance [110] to ascertain the performance from the proposed iris encoding and matching strategy. All the iris images employed in the experiments use automated iris segmentation approach described in CHAPTER 4, which has shown to be more accurate as it achieves superior segmentation accuracy for both the iris images acquired using visible and NIR imaging.

7.2.1 Databases and Evaluation Protocol

We followed the identical protocol as detailed in Section 5.2 to carry out the experiments on three publicly available databases. Table 7.1 summarizes all the major parameters used by the GeoKey iris encoding scheme for the three employed databases.

Table 7.1: Parameters employed by the proposed iris encoding scheme.

Parameter / Database	GeoKey Encoding				Log-Gabor Encoding	
	B	***h***	***S***	***d***	***Wavelength***	***SigmaOnf***
UBIRIS.v2	32	16	7	96	59	0.32
FRGC	16	8	5	48	40	0.35
CASIA.v4-distance	32	16	7	128	20	0.25

7.2.2 Combination of Global and Local Matching Scores

In this section, we report experimental results to achieve superior matching accuracy by simultaneously employ both the GeoKey and Log-Gabor recovered iris features. The matching scores computed from both GeoKey encoding scheme and Log-Gabor encoding scheme are combined at score level based on weighted sum rule. Figure 7.4 and Figure 7.5 show the receiver operating characteristic and cumulative match

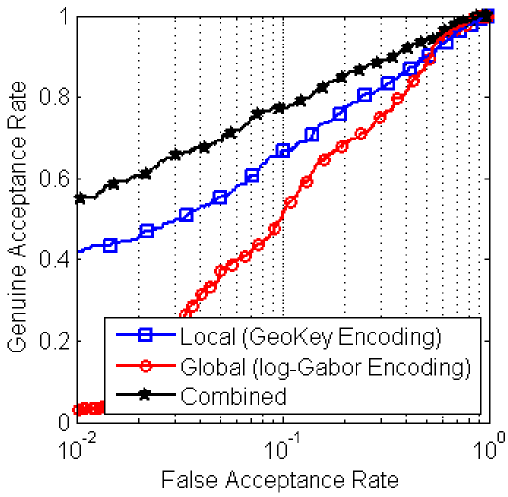

(a) UBIRIS.v2

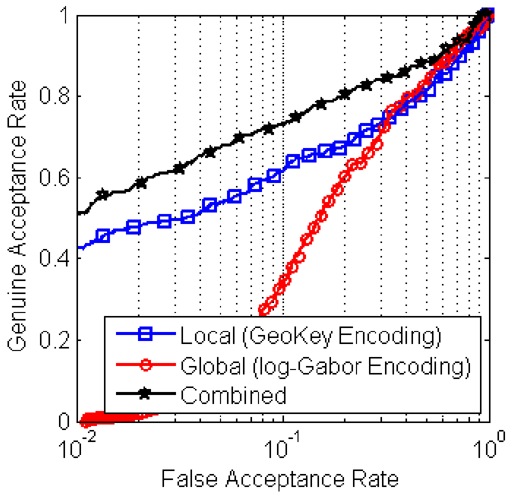

(b) FRGC

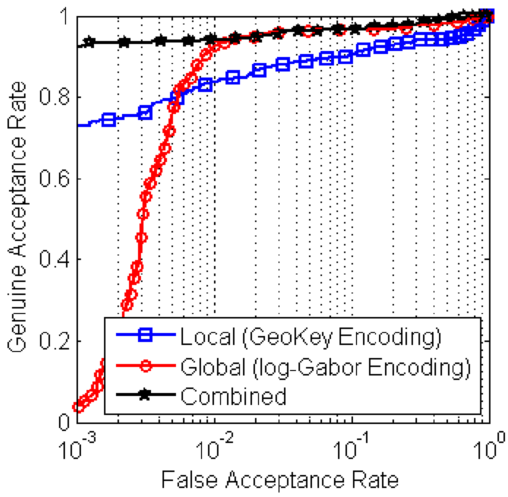

(c) CASIA.v4-distance

Figure 7.4: Receiver operating characteristics from the proposed GeoKey encoding scheme.

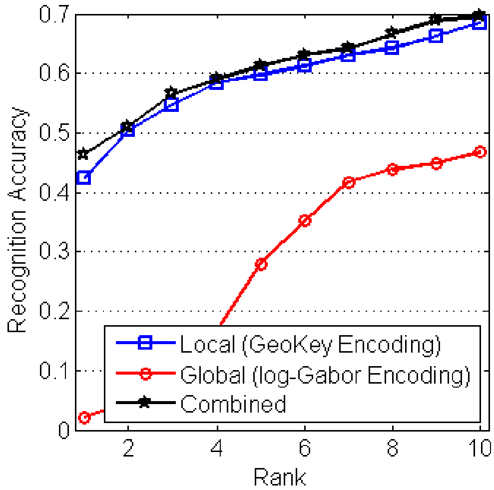

(a) UBIRIS.v2

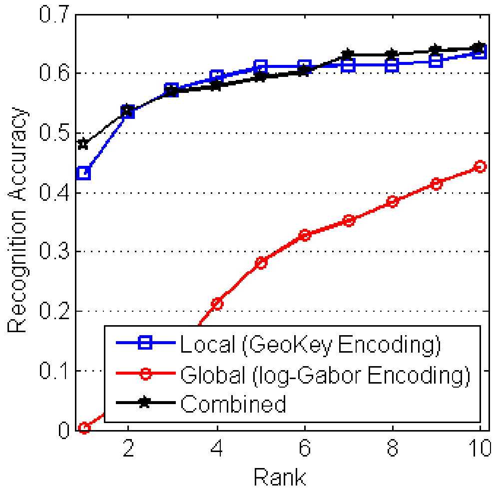

(b) FRGC

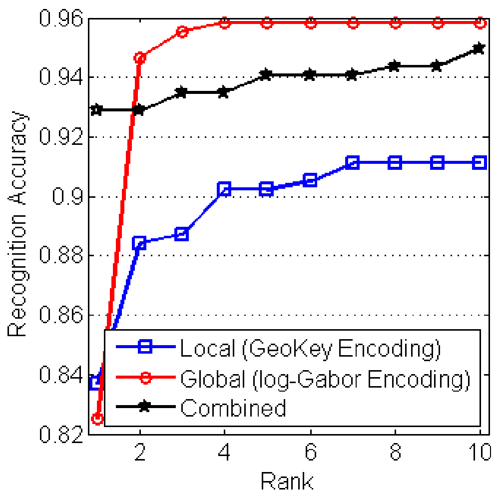

(c) CASIA.v4-distance

Figure 7.5: Cumulative match characteristic curves from the proposed GeoKey encoding scheme.

characteristic curves obtained from the three employed databases. The experimental results suggest that the combined scores from the recovered localized and global iris features can achieve more accurate recognition accuracy than employing either global or localized iris features alone.

7.2.3 Performance Comparison

In order to further ascertain the recognition performance of the proposed iris encoding scheme for the distantly acquired iris images under less constrained environments, we have also provided comparison with several competing iris encoding approaches from the literatures: Fragile Bits [47], [48], Personalized weight map (PWMap) [62], band-limited phase only correlation (BLPOC) [56], Log-Gabor [66] and Sparse [61]. The proposed GeoKey iris encoding scheme has shown its superiority by outperforming the other state-of-the-art iris encoding approaches in both the Equal Error Rate and decidability index, as can be observed from Table 7.2. The percentage of improvement in the EER as compared to other competing iris encoding approaches is provided in Figure 7.6. The proposed GeoKey iris encoding scheme achieves significant improvement over several competing iris encoding techniques, which suggests average improvements of *36.3%*, *32.7%* and *29.6%* in the equal error rates on UBIRIS.v2, FRGC and CASIA.v4-distance databases, respectively. Figure 7.7 and Figure 7.8 show the receiver operating characteristic and cumulative match characteristic curves obtained from various iris matching approaches.

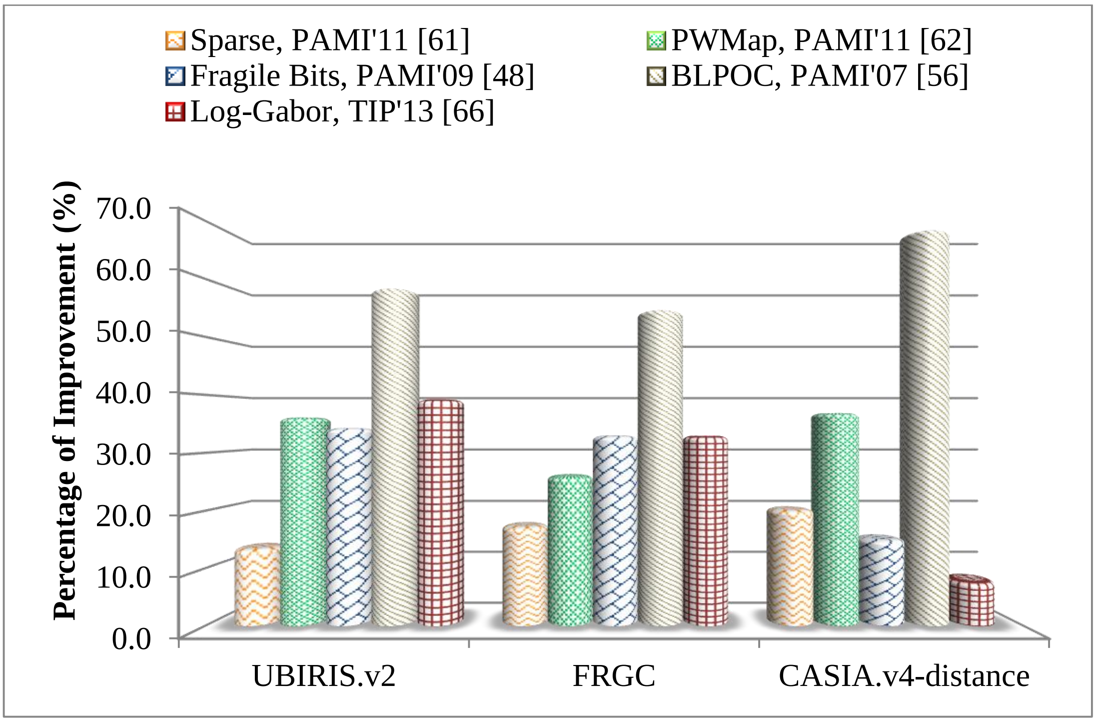

Figure 7.6: Expected improvement in Equal Error Rate as compared to several competing approaches from the literature.

Table 7.2: The Equal Error Rate and decidability index obtained by the different approaches from the three employed databases.

	UBIRIS.v2		FRGC		CASIA.v4-distance	
Method	**EER**	***d'***	**EER**	***d'***	**EER**	***d'***
Sparse [61]	0.1922	1.5842	0.2397	1.4298	0.0445	3.4345
PWMap [62]	0.2608	1.37	0.2681	1.1448	0.0564	3.4170
Fragile Bits [48]	0.2534	1.0923	0.2961	0.8284	0.0418	3.3054
BLPOC [56]	0.4022	0.4528	0.4396	0.2773	0.1136	2.6748
Log-Gabor [66]	0.2745	0.9266	0.2960	0.8280	0.0385	3.1525
Proposed	**0.1667**	**2.0774**	**0.1987**	**1.7166**	**0.0356**	**5.3243**

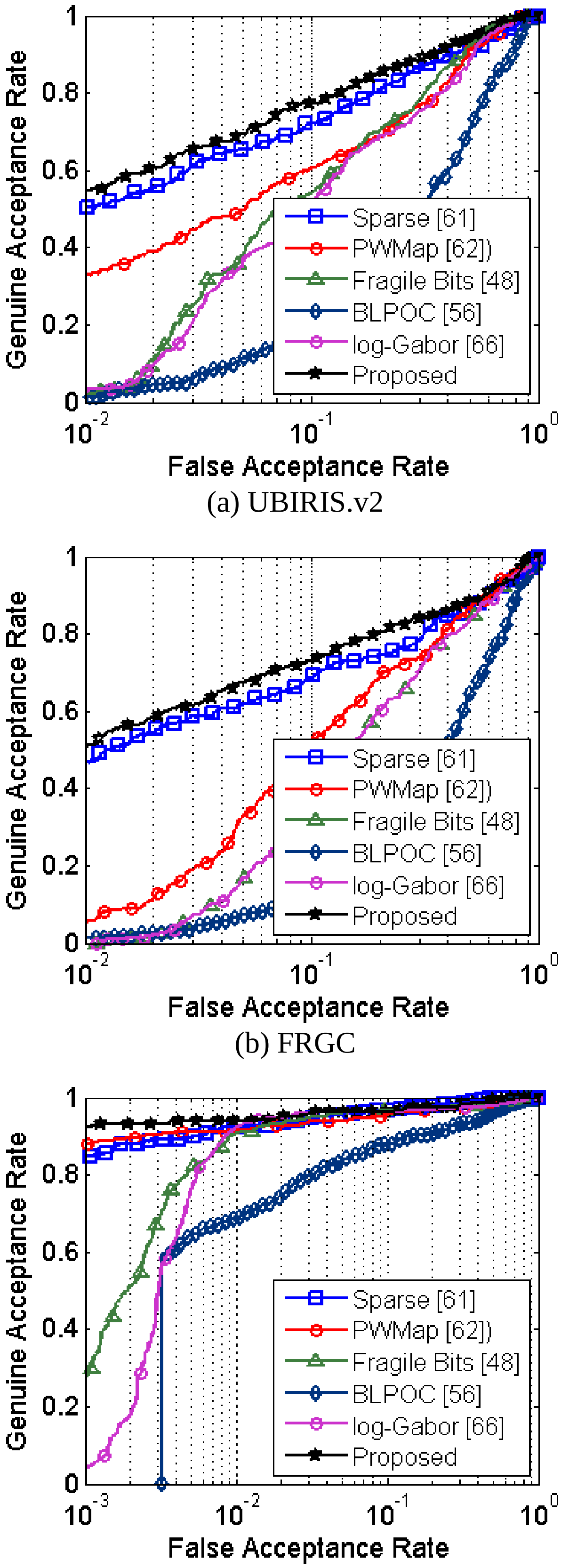

(a) UBIRIS.v2

(b) FRGC

(c) CASIA.v4-distance

Figure 7.7: Receiver operating characteristic curves from various approaches.

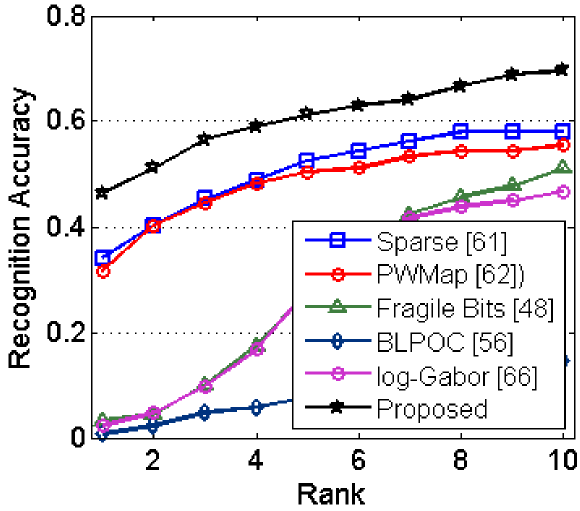

(a) UBIRIS.v2

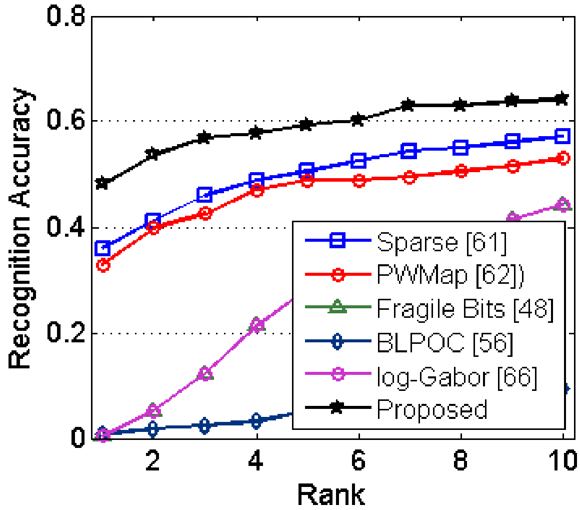

(b) FRGC

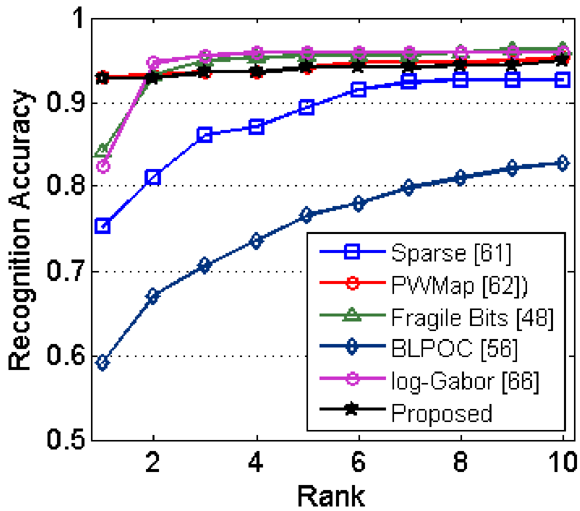

(c) CASIA.v4-distance

Figure 7.8:. Cumulative match characteristic curves from various approaches.

7.2.4 Joint Scores from Multiple Phase-based Features

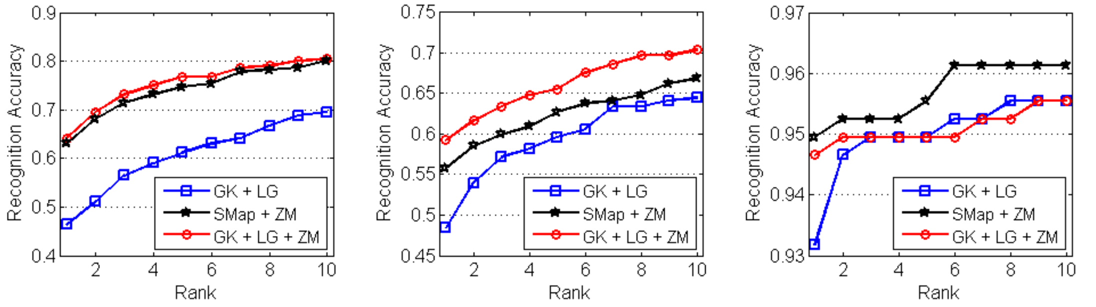

(a) UBIRIS.v2 (b) FRGC (c) CASIA.v4-distance

Figure 7.9: Cumulative match characteristic curves from joint scores of multiple phase-based features.

In this section, we show that the presented GeoKey encoding scheme in this chapter can be a solution to address the complexity of the global encoding scheme as detailed in Section 5.1.1, and yet achieve comparable recognition accuracy on the three employed databases. We compare the recognition performance from multiple phase-based features, *i.e.* GK (GeoKey encoding) + LG (Log-Gabor encoding), SMap (iris bits stabilization encoding) + ZM (ZMs phase-based encoding) and GK + LG + ZM. The experiments on (GK + LG + ZM) phase-based features are aimed to offer a more computationally attractive approach as an alternative to the global encoding module in Section 5.1.1. Figure 7.9 shows the cumulative match characteristic curves from the joint scores of multiple phase-based features on the three employed databases. It can be observed that comparable recognition accuracies have been reported from GK + LG + ZM phase-based features as compared to the reported results in CHAPTER 5, but with more computationally attractive.

7.2.5 Discussion

One attractive element of the proposed iris encoding and matching strategy in this chapter is its efficiency in both computation and memory requirements. The iris matching for both localized and global binarized iris features can be computed in

Table 7.3: Memory requirements by the best three algorithms from the experiments.

Database / Method	Memory Requirements Per Iris Template (bytes)		
	UBIRIS.v2	**FRGC**	**CASIA.V4-distance**
Sparse [61]	262144	65536	262144
PWMap [62]	4096 + 32768	1024 + 8192	4096 + 32768
CHAPTER 5	154752	39744	157952
- Stabilized bits	*16384 + 131072*	*4096 + 32768*	*16384 + 131072*
- Zernike moments	*3200 + 4096*	*1856 + 1024*	*6400 + 4096*
Proposed	**11584**	**4000**	**14848**
- GeoKey	*192*	*96*	*256*
- Log-Gabor	*4096 + 4096*	*1024 + 1024*	*4096 + 4096*
- Zernike moments	*3200*	*1856*	*6400*

very efficient way using the Hamming distance. Table 7.3 summarizes the requirements of the memory storage by the best three performing iris encoding and matching algorithms from the experiments (see Section 7.2.3) on the three employed databases, which suggest that much lower memory storage[x] is required by the proposed iris encoding and matching strategy. Although the memory requirement by the proposed iris encoding approach is higher than the conventional approach (*e.g.* [31], involves only computation of iris code and occlusion mask) which requires computation of multiple iris features in order to provide more accurate recognition accuracy. However, we expect that such limitation can be overcome with the rapid advent of computing powers and technologies (*e.g.* cloud computing). As mentioned earlier, quality of the eye images acquired at-a-distance and under less constrained environments, especially the visible illumination eye images, is usually degraded by multiple noise sources which can impair the recognition performance. The joint strategy of using multiple matchers can be more tolerant to the noise and provide more effective solution to recover discriminative iris features. Such joint strategy has shown to be promising based on the reported experimental results to provide more accurate iris recognition for eye images acquired at-a-distance and under less constrained imaging conditions.

[x] Memory requirement is computed based on the size of the normalized iris image (see Section 5.2.1).

7.3 Summary

This chapter has presented a computationally attractive GeoKey iris encoding and matching strategy for the noisy iris images acquired at-a-distance and under less constrained environments using either visible or NIR imaging. The superiority of the proposed iris encoding and matching strategy is ascertained by providing comparison with several state-of-the-art iris encoding and matching algorithms on three publicly available databases: UBIRIS.v2, FRGC, CASIA.v4-distance, which suggests the average improvements of 36.3%, 32.7% and 29.6% in equal error rates, respectively. In addition, the recognition performance from joint strategy of using multiple features was also investigated. The GeoKey encoding strategy which has its advantages in both computation and memory requirements can be used as an alternative to the global encoding module in Section 5.1.1. Such joint strategy of using multiple recovered iris features has shown to be promising, especially for the visible illumination eye images, as comparable recognition performance to the approach in CHAPTER 5 has been reported from our experiments (see Section 7.2.4).

CHAPTER 8

Conclusions and Future Work

The work described in this thesis has been concerned with the development of iris recognition algorithm for eye images acquired at-a-distance and under less constrained imaging conditions using either visible or NIR illumination. We developed an effective random walker based iris segmentation solution to automatically extract the iris regions from noisy eye images. In addition, a set of post-processing operations (initial iris center estimation, iris and pupil localization, boundary refinement, eyelid localization with adaptive eyelid models, eyelashes and shadow masking) which had shown to be effective to mitigate the commonly observed noise sources such as occlusions from eyelids, eyelashes and shadow were developed as well. The second open problem of at-a-distance iris recognition concerns with the development of robust feature encoding and matching algorithms which can be more tolerant to the inherent noise and variations in the segmented iris image quality and recover discriminative features from such noisy iris data. We presented an effective iris encoding and matching strategy by exploiting iris features from both global and localized normalized iris region pixels. The global iris encoding has its strength to recover discriminative iris features from less noisy iris region pixels while the localized iris encoding can better accommodate for imaging variations. The experimental results obtained from such joint strategy have shown to be promising, as the average improvements of 54.3%, 32.7% and 42.6% in equal error rates as compared to several competing approaches [48], [56], [66], [61], [62], were reported from the experiments on three publicly available databases: UBIRIS.v2, FRGC and CASIA.v4-distance, respectively.

One of the possible solutions to further improve the recognition accuracy for distantly iris recognition is to consider additional available features around the eye region, *i.e.* periocular. The periocular region is typically acquired simultaneously with the eye and therefore does not incur additional hardware cost. We presented the experimental results from using the joint iris and periocular strategy on the

UBIRIS.v2, FRGC and CASIA.v4-distance databases. The rank-one recognition rate of 85.1% was reported from the joint iris and periocular strategy on the UBIRIS.v2 database while the rank-one recognition rate from using iris alone was only 63%. For the experiment conducted on FRGC database, the rank-one recognition rate of 65.9% was observed from using joint iris and periocular strategy while the rank-one recognition rate of 55.8% was reported from using the iris alone. The strategy either considering joint iris and periocular or iris alone reported very similar rank-one recognition rates, *i.e.*, 95% and 96.1% on CASIA.v4-distance database. In such case, the contribution from the periocular features to complement the improvement of iris recognition performance seems to be limited. One possible reason may due to better image quality of the NIR illumination iris images from the CASIA.v4-distance database. The proposed iris encoding strategy can more effectively recover the discriminative iris features from such less noisy iris region pixels and achieves very promising recognition accuracy by using only iris alone.

In order to reduce the computational complexity and the memory requirement of the proposed iris encoding and matching strategy, a geometric key iris encoding scheme was investigated. Such geometric key iris encoding scheme produces binary iris templates by using computationally efficient and fast comparison operation on locally assembled image features. The generated binary iris templates are compact in size and allow efficient computation of their similarity using Hamming distance. The geometric key encoding scheme reported promising recognition results by providing comparison with several competing approaches [48], [56], [66], [61], [62], on the UBIRIS.v2, FRGC and CASIA.v4-distance databases, which reported the average improvements of 36.3%, 32.7% and 29.6% in equal error rates, respectively. We had shown experimentally that the computationally attractive geometric key encoding scheme can be a solution to address the complexity of the global iris encoding strategy presented earlier, and yet reported comparable recognition performance.

8.1 Contributions

Figure 8.1: Contribution highlights of this thesis.

This thesis makes several important contributions, as highlighted in Figure 8.1. Firstly, an effective iris segmentation approach was developed which can automatically extract the iris regions from eye images acquired at-a-distance and under less constrained environments. The proposed iris segmentation approach can simultaneously works on visible and NIR illumination eye images. Secondly, a global iris bits stabilization encoding strategy was proposed such that the iris bits which are highly consistent are rewarded while the inconsistent iris bits are penalized. Thirdly, a localized encoding strategy by exploiting the phase information of the ZMs was proposed. Such ZMs phase-based encoding strategy can be more tolerant to the imaging variations in the eye images acquired at-a-distance and under constrained environments. Fourthly, the strategy to jointly exploit the iris and periocular features was developed to further improve the recognition performance of the at-a-distance iris recognition. Lastly, a computationally attractive iris encoding and matching strategy was proposed.

8.2 Future Work

As future work, we hope to develop more effective iris encoding and matching algorithms which can be more accurate to perform iris recognition at-a-distance and under less constrained environments. One possible improvement works is to consider generation of dynamic geometric keys with different key lengths, block sizes and key generation functions for feature encoding which can be more adaptive to each enrolled user.

Another possible aspect for performance improvement is to consider different fusion strategy, for example, feature level fusion [129]. The feature set contains richer information extracted from the raw biometric data than the matching score and therefore it is expected to provide better recognition accuracy. However, template alignment issue, particularly the iris, has to be addressed before performing the feature level fusion [130].

Multispectral iris recognition can be a potential aspect to provide more accurate recognition accuracy [131]. Such multispectral strategy may better reveal iris textural information which is more sensitive to certain spectrum and such cross-spectral iris textural information can be further exploited to improve the recognition performance. Future iris recognition technologies may possibly require performing cross-spectral matching between the NIR and visible illumination eye images. Therefore, development of effective matching strategies which can seamlessly match such heterogeneous iris data is essential.

There are still several remaining issues which require further research effort to be devoted, especially for the visible illumination eye images. Recent studies have shown that the effect of iris template aging results in increase of false non-match rate [132], [133]. However, it still remains uncertain how such template aging phenomenon can impact the recognition performance on the visible illumination eye images. Textured cosmetic lenses are another major problem for iris recognition [134], [135]. The present contact lens detection approaches have been designed to work for NIR eye images. Therefore, further research effort is still required to study the applicability of such approaches on the visible illumination eye images.

BIBLIOGRAPHY

[1] A. Jain, A. Ross and S. Prabhakar, "An introduction to biometric recognition," *IEEE Trans. Circuits Syst. Video Technol.*, vol. 14, no. 1, pp. 4-20, 2004.

[2] A. Jain, P. Flynn and A. R. (Eds.), Handbook of Biometrics, Springer, 2008.

[3] P. Gregory and M. A. Simon, Biometrics For Dummies, Hoboken, NJ: Wiley, 2008.

[4] R. Bolle, J. Connell, S. Pankanti, N. Ratha and A. Senior, Guide to Biometrics, New York: Springer, 2004.

[5] R. Clarke, "Human Identification in Information Systems: Management Challenges and Public Policy Issues," *Information Technology & People*, vol. 7, no. 4, pp. 6-37, 1994.

[6] D. Zhang, F. Song, Y. Xu and Z. Liang, Advanced Pattern Recognition Technologies with Applications to Biometrics, Hershey, NY: Medical Information Science Reference, 2008.

[7] "CASIA.v3 Database," [Online]. Available: http://www.idealtest.org/dbDetailForUser.do?id=3. [Accessed 18 December 2013].

[8] "IIT Delhi Ear Database," [Online]. Available: http://www4.comp.polyu.edu.hk/~csajaykr/IITD/Database_Ear.htm. [Accessed 25 February 2014].

[9] "IIT Delhi Touchless Palmprint Database," [Online]. Available: http://www4.comp.polyu.edu.hk/~csajaykr/IITD/Database_Palm.htm. [Accessed 25 February 2014].

[10] "Face Recognition Grand Challenge – Overview," [Online]. Available: http://www.nist.gov/itl/iad/ig/frgc.cfm. [Accessed December 2013].

[11] "HKPU Finger Image Database," [Online]. Available: http://www4.comp.polyu.edu.hk/~csajaykr/fvdatabase.htm. [Accessed 25 February 2014].

[12] "LSA 352: Speech Recognition and Synthesis," [Online]. Available:

http://nlp.stanford.edu/courses/lsa352/. [Accessed 25 February 2014].

[13] "The Center for Research in Intelligent Systems (CRIS)," University of California, [Online]. Available: http://www.cris.ucr.edu/research.php. [Accessed 25 February 2014].

[14] J. Daugman, "Iris recognition at airports and border crossings," in *Encyclopedia of Biometrics*, S. Li and A. Jain, Eds., Springer, 2009, pp. 819-825.

[15] UIDAI, "Role of Biometric," 27 March 2012 . [Online]. Available: http://uidai.gov.in/images/role_of_biometric_technology_in_aadhaar_authentication_020412.pdf. [Accessed 17 December 2013].

[16] ICAO, "Machine Readable Travel Documents - Part 1 Machine Readable Passports," 2006. [Online]. Available: http://www.icao.int/publications/Documents/9303_p1_v2_cons_en.pdf. [Accessed 18 December 2013].

[17] "GovHK: The Smart Identity Card," [Online]. Available: http://www.gov.hk/en/residents/immigration/idcard/hkic/smartid.htm. [Accessed 16 December 2013].

[18] R. W. V. Bruegge, "Facial Recognition and Identification Initiatives," [Online]. Available: http://biometrics.org/bc2010/presentations/DOJ/vorder_bruegge-Facial-Recognition-and-Identification-Initiatives.pdf. [Accessed 17 December 2013].

[19] R. S. Snell and M. A. Lemp, Clinical Anatomy of the Eye, 2nd ed., Wiley-Blackwell, 1998.

[20] L. A. Remington, Clinical Anatomy of the Visual System, 2nd ed., Butterworth-Heinemann, 2005.

[21] U. R. Acharya, E. Ng and J. S. (Eds.), Image Modeling of the Human Eye, Massachusetts: Artech House, 2008.

[22] D. H. Cherwek, H. E. Grossniklaus and A. K. Hutchinson, "Iris," in *Duane's Ophthalmology*, Lippincott Williams & Wilkins, 2006.

[23] R. Wildes, "Iris recognition: An emerging biometric technology," *Proc. Of IEEE*, vol. 85, no. 9, pp. 1348-1363, 1997.

[24] K. Bowyer, K. Hollingsworth and P. Flynn, "Image understanding for iris biometrics: A survey," *Image Vision Comput.,* vol. 110, no. 2, pp. 181-307, 2008.

[25] M. J. Burge and K. Bowyer, Eds., Handbook of Iris Recognition, London: Springer, 2013.

[26] M. Dobeš, L. Machala, P. Tichavský and J. Pospíšil, "Human eye iris recognition using the mutual information," *Optik,* vol. 115, no. 9, pp. 399-405, 2004.

[27] M. Dobeš, J. Martinek, D. Skoupil, Z. Dobešová and J. Pospíšil, "Human eye localization using the modified Hough transform," *Optik,* vol. 117, no. 10, pp. 468-473, 2006.

[28] L. Flom and A. Safir, "Iris recognition system," U.S. Patent 4641349, 1987.

[29] J. Daugman, "High confidence visual recognition of persons by a test of statistical independence," *IEEE Trans. Pattern Anal. Mach. Intell.,* vol. 15, no. 11, pp. 1148-1161, 1993.

[30] J. Daugman, "Biometric personal identification system based on iris analysis," U.S. Patent 5291560, 1994.

[31] J. Daugman, "How iris recognition works," *IEEE Trans. Circuits Syst. Video Technol.,* vol. 14, no. 1, pp. 21-30, 2004.

[32] "ISO/IEC 19794-6:2005. Information technology - Biometric data interchange formats, part 6: Iris image data," International Organization for Standardization, 2005.

[33] "UPOL Iris Database," [Online]. Available: http://www.inf.upol.cz/iris/. [Accessed December 2013].

[34] J. Matey, O. Naroditsky, K. Hanna, R. Kolczynski, D. LoIacono, S. Mangru, M. Tinker, T. Zappia and W. Zhao, "Iris on the move: Acquisition of images for iris recognition in less constrained environments," *Proc. of the IEEE,* vol. 94, no. 11, pp. 1936-1947, 2006.

[35] S. Venugopalan, U. Prasad, K. Harun, K. Neblett, D. Toomey, J. Heyman and M. Savvides, "Long range iris acquisition system for stationary and mobile subjects," *Proc. IJCB 2011,* pp. 1-8, 2011.

[36] ANSI, "American national standard for the safe use of lasers and leds used in optical fiber transmission systems," ANSI Z136.2, 1988.

[37] CIE, "Photobiological safety standards for safety standards for lamps," Report of TC 6-38; CIE 134-3-99, 1999.

[38] N. Kourkoumelis and M. Tzaphlidou, "Medical safety issues concerning the use of incoherent infrared light in biometrics," in *Ethics and Policy of Biometrics* , vol. 6005, A. K. a. D. Zhang, Ed., Berlin / Heidelberg, Springer, 2010, pp. 121-126.

[39] H. Proenca and L. Alexandre, "UBIRIS: A noisy iris image database," *Proc. ICIAP 2005, Intern. Conf. Image Analysis and Processing,* 2005.

[40] H. Proenca, S. Filipe, R. Santos, J. Oliveira and L. Alexandre, "The UBIRIS.v2: A database of visible wavelength images captured on the move and at-a-distance," *IEEE Trans. Pattern Anal. Mach. Intell.,* vol. 32, no. 8, pp. 1529-1535, 2010.

[41] N. K. Ratha and V. G. (Eds.), Advances in Biometrics, Springer, 2008.

[42] "IIT Delhi Iris Database," [Online]. Available: http://www4.comp.polyu.edu.hk/~csajaykr/IITD/Database_Iris.htm. [Accessed 20 December 2013].

[43] J. Daugman, "New methods in iris recognition,," *IEEE Trans. Syst. Man Cybern. Part B Cybern.,* vol. 37, no. 5, pp. 1167-1175, 2007.

[44] Y. Lee, R. J. Micheals, P. J. Phillips and J. J. Filliben, "Video-based Automated System for Iris Recognition (VASIR)," NIST, [Online]. Available: http://www.nist.gov/itl/iad/ig/vasir.cfm. [Accessed 20 December 2013].

[45] Y. Lee, R. J. Micheals and P. J. Philips, "Improvements in video-based automated system for iris recognition (VASIR)," *Proc. Motion and Video Computing,* pp. 1-8, 2009.

[46] L. Ma, T. Tan, Y. Wang and D. Zhang, "Personal identification based on iris texture analysis," *IEEE Trans. Pattern Anal. Mach. Intell.,* vol. 25, no. 12, pp. 1519-1533, 2003.

[47] K. Hollingsworth, K. Bowyer and P. Flynn, "Using fragile bit coincidence to improve iris recognition," *Proc. BTAS 2009,* pp. 1-6, 2009.

[48] K. Hollingsworth, K. Bowyer and P.J. Flynn, "The best bits in an iris code," *IEEE Trans. Pattern Anal. Mach. Intell.,* vol. 31, no. 6, pp. 964-973, 2009.

[49] L. Masek and P. Kovesi, "MATLAB source code for a biometric identification system based on iris patterns," The School of Computer Science and Software Engineering, The University of Western Australia, 30 November 2003. [Online]. Available: http://www.csse.uwa.edu.au/~pk/studentprojects/libor/. [Accessed 21 December 2013].

[50] L. Ma, T. Tan, Y. Wang and D. Zhang, "Efficient iris recognition by characterizing key local variations," *IEEE Trans. Image Process.,* vol. 13, no. 6, pp. 739-750, 2004.

[51] A. Kumar and A. Passi, "Comparison and combination of iris matchers for reliable personal authentication," *Pattern Recognit.,* vol. 43, no. 3, pp. 1016-1026, 2010.

[52] Z. Sun and T. Tan, "Ordinal measures for iris recognition," *IEEE Trans. Pattern Anal. Mach. Intell.,* vol. 31, no. 12, pp. 2211-2226, 2009.

[53] Z. He, T. Tan, Z. Sun and X. Qiu, "Toward accurate and fast iris segmentation for iris biometrics," *IEEE Trans. Pattern Anal. Mach. Intell.,* vol. 31, no. 9, pp. 1670-1684, 2009.

[54] D. Monro, S. Rakshit and Z. Dexin, "DCT-based iris recognition," *IEEE Trans. Pattern Anal. Mach. Intell.,* vol. 29, no. 4, pp. 586-595, 2007.

[55] M. Vatsa, R. Singh and A. Noore, "Improving iris recognition performance using segmentation, quality enhancement, match score fusion, and indexing," *IEEE Trans. Syst. Man Cybern. Part B Cybern.,* vol. 38, no. 4, pp. 1021-1035, 2008.

[56] K. Miyazawa, K. Ito, T. Aoki, K. Kobayashi and H. Nakajima, "An effective approach for iris recognition using phase-based image matching," *IEEE Trans. Pattern Anal. Mach. Intell.,* vol. 30, pp. 1741-1756, 2008.

[57] E. Krichen, S. Garcia-Salicetti and B. Dorizzi, "A new phase-correlation-based iris matching for degraded images," *IEEE Trans. Syst. Man Cybern. Part B Cybern.,* vol. 39, no. 4, pp. 924-934, 2009.

[58] S. Shah and A. Ross, "Iris segmentation using geodesic active contours," *IEEE Trans. Inf. Forensics Secur.,* vol. 4, no. 4, pp. 824-836, 2009.

[59] T. Tan, Z. He and Z. Sun, "Efficient and robust segmentation of noisy iris images for non-cooperative iris recognition," *Image Vision Comput.,* vol. 28, no. 2, pp. 223-230, 2010.

[60] H. Proenca, "Iris recognition: On the segmentation of degraded images acquired in the visible Wavelength," *IEEE Trans. Pattern Anal. Mach. Intell.,* vol. 32, no. 8, pp. 1502-1516, 2010.

[61] J. Pillai, V. Patel, R. Chellappa and N. Ratha, "Secure and robust iris recognition using random projections and sparse representations," *IEEE Trans. Pattern Anal. Mach. Intell.,* vol. 33, pp. 1877-1893, 2011.

[62] W. Dong, Z. Sun and T. Tan, "Iris matching based on personalized weight map," *IEEE Trans. Pattern Anal. Mach. Intell.,* vol. 33, no. 9, pp. 1744-1757, 2011.

[63] R.M. da Costa and A. Gonzaga, "Dynamic features for iris recognition," *IEEE Trans. Syst. Man Cybern. Part B Cybern.,* vol. 42, no. 4, pp. 1072-1082, 2012.

[64] T. Tan, X. Zhang, Z. Sun and H. Zhang, "Noisy iris image matching by using multiple cues," *Pattern Recognit. Lett.,* vol. 33, no. 8, pp. 979-977, 2012.

[65] C.-W. Tan and A. Kumar, "A unified framework for automated iris segmentation using distantly acquired face images," *IEEE Trans. Image Process.,* vol. 21, no. 9, pp. 4068-4079, 2012.

[66] C. Tan and A. Kumar, "Towards online iris and periocular recognition under relaxed imaging constraints," *IEEE Trans. Image Process.,* vol. 22, no. 10, pp. 3751-3765, 2013.

[67] J. Daugman and I. Malhas, "Iris recognition border-crossing system in the UAE," *Biometrics,* vol. 44, no. 2, pp. 49-53, 2004.

[68] "The United Arab Emirates Deployment of Iris Recognition," [Online]. Available: http://www.cl.cam.ac.uk/~jgd1000/deployments.html. [Accessed 24 December 2013].

[69] Z. He, T. Tan and Z. Sun, "Iris localization via pulling and pushing," *Proc. ICPR 2006,* pp. 366-369, 2006.

[70] X. Huang, B. Fu, C. Ti, A. Tokuta and R. Yang, "Robust varying-resolution iris recognition," *Proc. BTAS 2012,* pp. 47-54, 2012.

[71] D. J. Fields, "Relations between the statistics of natural images and the response properties of cortical cells," *J. Opt. Soc. Am. A,* vol. 4, no. 12, pp. 2379-2394, 1987.

[72] P. Yao, J. Li, X. Ye, Z. Zhuang and B. Li, "Iris recognition algorithm using modified Log-Gabor filters," *Proc. ICPR 2006,* pp. 461-464, 2006.

[73] K. Hollingsworth, K. Bowyer and P. Flynn, "Improved iris recognition through fusion of Hamming distance and fragile bit distance," *IEEE Trans. Pattern Anal. Mach. Intell.,* vol. 33, no. 12, pp. 2465-2476, 2011.

[74] J. Pillai, V. Patel and R. Chellappa, "Sparsity inspired selection and recogniton of iris images," *Proc. BTAS 2009,* pp. 1-6, 2009.

[75] A. Kumar and T.-S. Chan, "Iris recognition using quaternionic sparse orientation code (QSOC)," *Proc. CVPRW 2012,* pp. 59-64, 2012.

[76] D. G. Lowe, "Distinctive image features from scale-invariant keypoints," *Int. J. Comput. Vision,* vol. 60, no. 2, pp. 91-110, 2004.

[77] E. Tola, V. Lepetit and P. Fua, "DAISY: Aan efficient dense descriptor applied to wide-baseline stereo," *IEEE Trans. Pattern Anal. Mach. Intell.,* vol. 32, no. 5, pp. 815-830, 2010.

[78] L. Yu, D. Z. and K. Wang, "The relative distance of key point based iris recognition," *Pattern Recogn.*, vol. 40, no. 2, pp. 423-430, 2007.

[79] C. Belcher and Y. Du, "Region-based SIFT approach to iris recognition," *Optics and Lasers in Engineering,* vol. 47, no. 1, pp. 139-147, 2009.

[80] M. Zhang, Z. Sun and T. Tan, "Deformable DAISY matcher for robust iris recognition," *Proc. ICIP 2011,* pp. 3189-3192, 2011.

[81] "Light and the Modern Atom," 9 November 2009. [Online]. Available: http://www.chemistryland.com/CHM151W/07-Atomic%20Structure/Spectra/ModernAtom151.html. [Accessed 30 December 2013].

[82] "NICE.I - Noisy Iris Challenge Evaluation, Part I," [Online]. Available: http://nice1.di.ubi.pt/index.html. [Accessed December 2013].

[83] W. Sankowski, K. Grabowski, M. Napieralska, M. Zubert and A. Napieralski, "Reliable algorithm for iris segmentation in eye image," *Image Vision*

Comput., vol. 28, no. 2, pp. 231-237, 2010.

[84] P. Almeida, "A knowledge-based approach to the iris segmentation problem," *Image Vision Comput.*, vol. 28, no. 2, pp. 238-245, 2010.

[85] P. Li, X. Liu, L. Xiao and Q. Song, "Robust and accurate iris segmentation in very noisy iris images," *Image Vision Comput.*, vol. 28, no. 2, pp. 246-253, 2010.

[86] D. S. Jeong, J. W. Hwang, B. J. Kang, K. R. Park, C. S. Won, D.-K. Park and J. Kim, "A new iris segmentation method for non-ideal iris images," *Image Vision Comput.*, vol. 28, no. 2, pp. 254-260, 2010.

[87] Y. Chen, M. Adjouadi, C. Han, J. Wang, A. Barreto, N. Rishe and J. Andrian, "A highly accurate and computationally efficient approach for unconstrained iris segmentation,," *Image Vision Comput.*, vol. 28, no. 2, pp. 261-269, 2010.

[88] R. D. Labati and F. Scotti, "Noisy iris segmentation with boundary regularization and reflections removal," *Image Vision Comput.*, vol. 28, no. 2, pp. 270-277, 2010.

[89] C.-W. Tan and A. Kumar, "Efficient iris segmentation using Grow-Cut algorithm for remotely acquired iris images," *Proc. BTAS 2012*, pp. 99-104, 2012.

[90] "NICE:II - Noisy Iris Challenge Evaluation, Part II," [Online]. Available: http://nice2.di.ubi.pt/. [Accessed December 2013].

[91] Q. Wang, X. Zhang, M. Li, X. Dong, Q. Zhou and Y. Yin, "Adaboost and multi-orientation 2D Gabor-based noisy iris recognition," *Pattern Recogn. Lett.*, vol. 33, no. 8, pp. 978-983, 2012.

[92] G. Santos and E. Hoyle, "A fusion approach to unconstrained iris recognition," *Pattern Recogn. Lett.*, vol. 33, no. 8, pp. 984-990, 2012.

[93] K. Bowyer, "The results of the NICE.II iris biometrics competition," *Pattern Recognit. Lett.*, vol. 33, no. 8, pp. 965-969, 2012.

[94] H. Proenca and L. Alexandre, "Toward covert iris biometric recognition: Experimental results from the NICE Contests," *IEEE Trans. Inf. Forensics Secur.*, vol. 7, pp. 798-808, 2012.

[95] Z. He, Z. Sun, T. Tan, X. Qiu, C. Zhong and W. Dong, "Boosting ordinal features for accurate and fast iris recognition," *Proc. CVPR 2008*, pp. 1-8,

2008.

[96] U. Park, R. R. Jillela, A. Ross and A. K. Jain, "Periocular biometrics in the visible spectrum," *IEEE Trans. Info. Forensics & Security,* vol. 6, no. 1, pp. 96-106, 2011.

[97] K. Y. Shin, G. P. Nam, D. S. Jeong, D. H. Cho, B. J. Kang, K. R. Park and J. Kim, "New iris recognition method for noisy iris images," *Pattern Recogn. Lett.,* vol. 33, no. 8, pp. 991-999, 2012.

[98] P. Li, X. Liu and N. Zhao, "Weighted co-occurrence phase histogram for iris recognition," *Pattern Recogn. Lett.,* vol. 33, no. 8, pp. 1000-1005, 2012.

[99] M. D. Marsico, M. Nappi and D. Riccio, "Noisy iris recognition integrated scheme," *Pattern Recogn. Lett.,* vol. 33, no. 8, pp. 1006-1011, 2012.

[100] P. Li and H. Ma, "Iris recognition in non-ideal imaging conditions," *Pattern Recogn. Lett.,* vol. 33, no. 8, pp. 1012-1018, 2012.

[101] R. Szewczyk, K. Grabowski, M. Napieralska, W. Sankowski, M. Zubert and A. Napieralski, "A reliable iris recognition algorithm based on reverse biorthogonal wavelet transform," *Pattern Recogn. Lett.,* vol. 33, no. 8, pp. 1019-1026, 2012.

[102] "OpenCV," [Online]. Available: http://opencv.org/. [Accessed 2 January 2014].

[103] P. Viola and M. Jones, "Rapid object detection using a boosted cascade of simple features," *Proc. CVPR 2001,* pp. 511-518, 2001.

[104] D. H. Brainard and B. A. Wandell, "Analysis of the retinex theory of color vision," *J. Opt. Soc. Am. A,* vol. 3, no. 10, pp. 1651-1661, 1986.

[105] V. Štruc and N. Pavešić, "Gabor-based kernel partial-least-squares discrimination features for face recognition," *Informatica (Vilnius),* vol. 20, no. 1, pp. 115-138, 2009.

[106] V. Štruc and N. Pavešić, "Performance evaluation of photometric normalization techniques for illumination invariant face recognition," in *Advances in Face Image Analysis: Techniques and Technologies*, Y. Zhang, Ed., IGI-Global, 2011, pp. 279-300.

[107] L. Grady, "Random walks for image segmentation," *IEEE Trans. Pattern*

Anal. Mach. Intell., vol. 28, no. 11, pp. 1768-1783, 2006.

[108] J. Bondy and U. Murty, Graph Theory, Springer, 2008.

[109] P. Phillips, P. Flynn, T. Scruggs, K. Bowyer, J. Chang, K. Hoffman, J. Marques, J. Min and W.Worek, "Overview of the face recognition grand challenge," *Proc. CVPR 2005*, pp. 947-954, 2005.

[110] "CASIA.v4 Database," [Online]. Available: http://biometrics.idealtest.org/dbDetailForUser.do?id=4. [Accessed 18 December 2013].

[111] D. Comaniciu and P. Meer, "Mean shift: A robust approach toward feature space analysis," *IEEE Trans. Pattern Anal. Mach. Intell.,* vol. 24, no. 5, pp. 603-619, 2002.

[112] P. Armitage, G.Berry and J. N. S. Matthews, Statistical Methods in Medical Research, 4th ed., Blackwell Publishing, 2002.

[113] A. Khotanzad and Y. H. Hong, "Invariant image recognition by Zernike moments," *IEEE Trans. Pattern Anal. Mach. Intell.,* vol. 12, no. 5, pp. 489-497, 1990.

[114] C.-H. Teh and R. Chin, "On image analysis by the methods of moments," *IEEE Trans. Pattern Anal. Mach. Intell.,* vol. 10, no. 4, pp. 496-513, 1998.

[115] J. Revaud, G. Lavoue and A. Baskurt, "Improving Zernike moments comparison for optimal similarity and rotation angle retrieval," *IEEE Trans. Pattern Anal.* .

[116] Z. Chen and S.-K. Sun, "A Zernike moment phase-based descriptor for local image representation and matching," *IEEE Trans. Image Process.,* vol. 19, no. 1, pp. 205-219, 2010.

[117] C.-W. Tan and A. Kumar, "Automated segmentation of iris images using visible wavelength face images," *Proc. CVPR 2011,* pp. 9-14, 2011.

[118] "VLFeat: An Open and Portable Library of Computer Vision Algorithms," [Online]. Available: http://www.vlfeat.org/. [Accessed 5 January 2014].

[119] A. Oliva and A. Torralba, "Modeling the shape of the scene: A holistic representation of the spatial envelope," *Int. J. Comput. Vision,* vol. 42, no. 3, pp. 145-175, 2001.

[120] T. Ojala, M. Pietikainen and T. Maenpaa, "Multiresolution gray-scale and rotation invariant texture classification with local binary patterns," *IEEE Trans. Pattern Anal. Mach. Intell.,* vol. 24, no. 7, pp. 971-987, 2002.

[121] N. Dalal and B. Triggs, "Histograms of oriented gradients for human detection," *Proc CVPR 2005,* pp. 886-893, 2005.

[122] T. Leung and J. Malik, "Representing and recognizing the visual appearance of materials using three-dimensional textons," *Int. J. Comput. Vision,* vol. 43, no. 1, pp. 29-44, 2001.

[123] V. P. Pauca, M. Forkin, X. Xu, R. Plemmons and A. Ross, "Challenging ocular image recognition," *Proc. of SPIE (Biometric Technology for Human Identification VIII),* vol. 8029, 2011.

[124] S. Bharadwaj, H. Bhatt, M. Vatsa and R. Singh, "Periocular biometrics: When iris recognition fails," *Proc. BTAS 2010,* pp. 1-6, 2010.

[125] D. L. Woodard, S. Pundlik, P. Miller, R. Jillela and A. Ross, "On the fusion of periocular and iris biometrics in non-ideal imagery," *Proc. ICPR 2010,* pp. 201-204, 2010.

[126] M. Calonder, V. Lepetit, M. Ozuysal, T. Trzcinski, C. Strecha and P. Fua, "BRIEF: Computing a local binary descriptor very fast," *IEEE Trans. Pattern Anal. Mach. Intell.,* vol. 34, no. 7, pp. 1281-1298, 2012.

[127] K. Jänich, Linear algebra, New York: Springer-Verlag, 1994.

[128] M. Ozuysal, M. Calonder, V. Lepetit and P. Fua, "Fast keypoint recognition using random ferns," *IEEE Trans. Pattern Anal. Mach. Intell.,* vol. 32, no. 3, pp. 448-461, 2010.

[129] A. Ross and A. K. Jain, "Fusion Techniques in Multibiometric Systems," in *Face Biometrics for Personal Identification*, B. Abidi and M. A. Abidi, Eds., Springer, 2007, pp. 185-212.

[130] C. Rathgeb and C. Busch, "Multi-Biometric Template Protection: Issues and Challenges," in *New Trends and Developments in Biometrics*, J. Yang and S. J. Xie, Eds., InTech, 2012.

[131] C. Boyce, A. Ross, M. Monaco, L. Hornak and L. Xin, "Multispectral iris analysis: A preliminary study," *Proc. CVPRW 2006,* p. 51, 2006.

[132] S. Fenker, E. Ortiz and K. Bowyer, "Template aging phenomenon in iris recognition," *IEEE Access,* vol. 1, pp. 266-274, 2013.

[133] K. W. Bowyer and E. Ortiz, "Making sense of the IREX VI report," Computer Vision Research Lab, 2013.

[134] J. Doyle, P. Flynn and K. Bowyer, "Automated classification of contact lens type in iris images," *Proc. ICB 2013,* pp. 1-6, 2013.

[135] N. Kohli, D. Yadav, M. Vatsa and R. Singh, "Revisiting iris recognition with color cosmetic contact lenses," *Proc. ICB 2013,* pp. 1-7, 2013.

[136] A. Ross and A. K. Jain, "Multimodal biometrics: an overview," *Proc. EUSIPCO,* pp. 1221-1224, 2004.

[137] K. W. Bowyer, K. I. Chang, P. Yan, P. J. Flynn and S. S. E. Hansley, "Multi-modal biometrics: an overview (invited talk)," *Proc. MMUA,* 2006.

[138] C.-W. Tan and A. Kumar, "Human identification from at-a-distance images by simultaneously exploiting iris and periocular features," *Proc. ICPR 2012,* pp. 553-556, 2012.

[139] C.-W. Tan and A. Kumar, "Adaptive and localized iris weight map for accurate iris recognition under less constrained environments," *Proc. BTAS 2013,* pp. 1-7, 2013.

[140] K. Hollingsworth, S. Darnell, P. Miller, D. Woodard, K. Bowyer and P. Flynn, "Human and machine performance on periocular biometrics under near-infrared light and visible light," *IEEE Trans. Inf. Forensics Secur.,* vol. 7, no. 2, pp. 588-601, 2012.

[141] C.-W. Tan and A. Kumar, "Accurate iris recognition at a distance using stabilized iris encoding and Zernike moments phase features," *IEEE Trans. Image Process.,* vol. 23, no. 9, pp. 3962-3974, 2014.